

**PALEOCENE TURBIDITE DEPOSITION IN THE CENTRAL AMERICAN  
SEAWAY (NW COSTA RICA): GEOCHEMICAL ANALYSIS AND  
PROVENANCE OF DETRITAL SPINEL AND CLINOPYROXENE**

---

A Thesis Presented to  
the Faculty of the College of Natural Sciences and Mathematics  
University of Houston

---

In Partial Fulfillment  
of the Requirements for the Degree  
Master of Science

---

By  
Allegra Catherine Thibodaux Giblin  
August 2015

**PALEOCENE TURBIDITE DEPOSITION IN THE CENTRAL AMERICAN  
SEAWAY (NW COSTA RICA): GEOCHEMICAL ANALYSIS AND  
PROVENANCE OF DETRITAL SPINEL AND CLINOPYROXENE**

---

Allegra Giblin

---

Dr. Jonathan Snow, Chair

---

Dr. Esteban Gazel, Virginia Polytechnic  
Institute and State University, Blacksburg,  
VA

---

Dr. Joel Saylor

---

Dr. Virginia Sisson

---

Dr. Dan Wells, Dean, College of Natural  
Sciences and Mathematics

**PALEOCENE TURBIDITE DEPOSITION IN THE CENTRAL AMERICAN  
SEAWAY (NW COSTA RICA): GEOCHEMICAL ANALYSIS AND  
PROVENANCE OF DETRITAL SPINEL AND CLINOPYROXENE**

---

An Abstract of a Thesis

Presented to

the Faculty of the College of Natural Sciences and Mathematics

University of Houston

---

In Partial Fulfillment

of the Requirements for the Degree

Master of Science

---

By

Allegra Catherine Thibodaux Giblin

August 2015

The Central American Land Bridge is the crucial connection between North and South America, and the Miocene closure of the Panama seaway led to a change in global oceanic circulation patterns. Modern Costa Rica is part of the island arc that formed over the western Caribbean subduction zone, and the Santa Elena peninsula is on the northwest coast of Costa Rica next to the Sandino forearc basin. This study focuses on the origin and provenance of the Paleocene deep water Rivas and Descartes turbidites that crop out on the northern part of the Santa Elena peninsula in northwestern Costa Rica. Understanding the sedimentary fill of the Sandino Basin that contributed to the closing of the seaway may lead to a better understanding of the Late Cretaceous-Paleogene arcs.

Provenance studies of the Santa Elena Peninsula turbidite sandstone bodies constrain the history of the paleogeography and tectonics of the region. Petrographic analyses of rock thin sections constrain source areas; geochemical analysis of individual detrital heavy minerals from rock samples give indications of sediment sources and tectonic setting during deposition. This study is a provenance analysis based on (i) semi-quantitative energy-dispersive spectrometry analysis of heavy minerals, (ii) quantitative wavelength-dispersive spectrometry for major elements of detrital clinopyroxene and spinel grains, (iii) trace element analysis through laser ablation of single detrital clinopyroxene grains, and (iv) comparative analysis of the different potential source rocks to clearly identify the most likely sediment sources.

The detrital spinel and clinopyroxene are possibly sourced from: mantle ophiolites, mid-ocean ridge gabbros, or volcanic arc tholeiitic basalts or calc-alkaline andesites. Spinel and clinopyroxene geochemistry suggests a possible peridotitic source,

linked to mantle rocks that are now covered by Tertiary volcanic rocks or have completely eroded. The character of the crustal minerals indicates sources from mid-ocean ridge gabbros, and island arc tholeiites and andesites. This suggests that during the early history of the gateway uplift and seaway closure, sediment sources were dominated first by older ophiolites and gabbroic sources, then by volcanic inputs from the arc.

<b>Contents</b>	
<b>Abstract</b> .....	iv
<b>Introduction</b> .....	1
<b>General morphology</b> .....	4
<b>Tectonics and volcanism</b> .....	7
<b>Forearc basin development</b> .....	9
<b>Paleocurrents and deposition</b> .....	10
<b>Sedimentary deposits</b> .....	12
<i>Rivas Formation</i> .....	12
<i>Descartes Formation</i> .....	14
<b>Geologic setting of potential sedimentary source rocks</b> .....	17
<i>Santa Elena Ophiolite</i> .....	17
<i>Santa Rosa Accretionary Complex</i> .....	18
<i>Nicoya Complex</i> .....	20
<b>Analytical methods</b> .....	22
<b>Sample collection</b> .....	22
<b>Sample preparation</b> .....	24
<b>Electron microprobe analysis</b> .....	25
<b>Laser ablation inductively coupled mass spectrometry</b> .....	29
<b>Results</b> .....	41
<b>Petrography</b> .....	41
<b>Mineral identification</b> .....	42
<b>Clinopyroxene</b> .....	42
<i>Major element geochemistry of clinopyroxene</i> .....	42
<i>Trace element geochemistry of clinopyroxene</i> .....	49
<b>Spinel</b> .....	58
<b>Discussion</b> .....	66
<b>Tectonic setting and petrogenesis</b> .....	66
<b>Ophiolite sources</b> .....	67
<b>Mid-ocean ridge gabbroic sources</b> .....	72
<b>Arc volcanics</b> .....	75
<b>Paleogeography of Paleocene–Eocene Central America</b> .....	77
<b>Conclusions</b> .....	82
<b>References</b> .....	84
<b>Appendix I (Sample locations and maps)</b> .....	96
<b>Appendix II (Additional diagrams)</b> .....	102
<b>Appendix III (Petrographic descriptions)</b> .....	115
<b>Appendix IV (Error analysis)</b> .....	122

## **Introduction**

The closing of the Central American seaway between North and South America led to a change in global oceanic circulation patterns and affected global climate. The seaway closure was due to the formation of a land bridge by the collision of various terranes over time and the Middle America arc is considered an amalgamation of continental crust in northern Central America, along with the remnants of the oceanic Caribbean Large Igneous Province (CLIP) and older arcs (Late Cretaceous to Paleogene), and the modern Costa Rica-Panama arc (Pindell et al., 2006; Mann et al., 2007; Pindell and Kennan, 2009). Ocean circulation has influenced the overlying atmosphere and therefore the climate. The breakup of the supercontinent Pangaea began in the Triassic and as they fractured, the different landmasses became separated by large, narrow, shallow seas. In the Cretaceous, off-axis volcanism and rapid seafloor spreading at mid-ocean ridges reduced the volume of the oceans and led to a rise in eustatic sea levels as much as 250 m above present day levels. The early Paleogene world had very warm climates with surface temperatures a few degrees warmer than today (Estes and Hutchinson, 1980; Poulsen et al., 2001). The warming trend continued through the Paleocene, with the Paleocene/Eocene boundary marked by a brief global warming event due to increased atmospheric greenhouse gas concentrations. (Bice and Marotzke, 2002). Meanwhile the seaway between North and South America was open, with water freely flowing between the Pacific and Atlantic oceans. The restriction of this open seaway, beginning in the Miocene, is coincident with the appearance of ice in the Arctic; restricting the oceanic flow between the Pacific and Atlantic oceans led to a changing of

the thermohaline circulation patterns in the oceans, altering oceanic heat flow and transport, producing global effects. It is likely that oceanic gateways have played a major role in determining the Earth's climate (Brass et al., 1982).

The modern land bridge that developed over time and closed the Panamanian seaway is part of a complicated history of plate tectonic movement that led to an accumulation of accreted terranes forming its backbone; components of the backbone include remnants of the oceanic Caribbean Large Igneous Province (CLIP), ophiolites obducted on to the CLIP, the primitive tholeiitic arc that formed between the Aptian to Santonian, and the andesitic arc that began forming in the Maastrichtian (Seyfried et al., 1987; Alvarado et al., 2007). The CLIP began move eastward between the westward moving North and South American plates and into the Caribbean in the Cretaceous (Pindell et al., 2006). Pindell (2006) suggests the western Caribbean margin may have remained inactive until late Albian (~95 Ma) when subduction commenced. Subduction of the Pacific plate underneath the Caribbean plate led to the initiation of island arc volcanism and the opening of forearc basins. Throughout the Paleogene, tectonics were relatively stable and by the middle Miocene (13-15 Ma) the seaway was closed (Montes et al., 2015).

When island arc volcanism began, a forearc basin opened between the CLIP and the trench. The forearc Sandino Basin (Figures 1, 2) stretches from southern Mexico to northwestern Costa Rica (Ranero et al., 2007). It was very deep initially and had much accommodation space to receive sediment deposits. There are 5 main syn-tectonic, volcanoclastic turbidite deposits in the Sandino Basin; of these deposits the oldest are the Rivas and Descartes Formations (known as the Rivas and Brito

Formations in Nicaragua), which record the history of the Cretaceous through Paleogene arc lavas that are not well known or well described in Central America (Alvarado et al., 2007). These sediments indicate the presence of the older arc, along with sediments from other tectonic sources, and reveal the composition of the arc that is either covered by younger volcanics or no longer exists in outcrop. These sediments played a part in the gateway closure and record the history of the tectonics at a time before the seaway closure.

Provenance studies of sandstone bodies can help to unravel the complex histories of the paleogeography, paleocurrents and tectonics of a region. They can also determine the source rocks of the detrital grains within the sandstones. This study focuses on the origin and provenance of the deep water Rivas and Descartes Formation turbidites, deposited in the forearc Sandino Basin, that have been uplifted and outcrop on the northern part of the Santa Elena peninsula in northwestern Costa Rica. Detrital heavy minerals, clinopyroxene and spinel, found in the Rivas and Descartes turbiditic sandstones can reveal an answer to the question: at the time Panama gateway was open, what are the sediment sources and where was the high ground? Understanding the sediment sources helps to understand the paleogeography at the time of deposition and what rocks made up the high ground that formed the backbone for the Central American isthmus.

While petrographic analyses of rock thin sections can narrow down source areas, other factors such as climate, transport mechanism, and source mixing may affect the sandstone compositions and obscure identification of unique source areas (Morton, 1991). A better technique involves geochemical analysis of individual detrital heavy

minerals for distinguishing sediment sources and tectonic setting during deposition. Methods of analysis include (i) semi-quantitative analysis through energy-dispersive spectrometry (EDS) of heavy mineral abundance, (ii) wave-dispersive spectrometry (WDS) for the major elements with the electron microprobe (EMP) of detrital clinopyroxene and spinel grains, (iii) trace element analysis through laser ablation inductively-coupled mass spectrometry (LA-ICP-MS) of single detrital clinopyroxene grains, and (iv) comparative analysis of the different potential source rocks to clearly identify the most likely sources of detrital grains within the Rivas and Descartes Formation turbidites. Results indicate tectonic provenance of the sediments and lead to a better understanding of the evolution of the erosion-sedimentation system over time in the Sandino Basin.

### **General morphology**

Southern Central America has fundamentally different geology from northern Central America. There is no Paleozoic crystalline basement or Paleozoic to Mesozoic continental sedimentary cover. Costa Rica is located in southern Central America and was formed by accreted oceanic, volcanic, and sedimentary terrane dating primarily from the Cretaceous and onwards (Weyl, 1980). These accreted terranes make up the backbone of the land bridge that began to form over the western Caribbean subduction zone starting in the Aptian.

The Guanacaste region in the northwest of Costa Rica is divided into three major morphotectonic regions: (1) the emerged outer arc which includes the Santa Elena and Nicoya peninsulas; (2) the trough of the inner forearc (Tempisque basin), including the

Gulf of Nicoya; and (3) the inner arc composed of the active volcanic cordilleras of Guanacaste and Tilaran (Weyl, 1980; Calvo, 2003) (see Figure 1). The Cordillera de Guanacaste is a NW/SE trending line of Quaternary volcanoes that separate the Pacific and Caribbean lowlands, and include Rincon de la Vieja, which occasionally erupts steam and ash, and the more famous Arenal, which erupted massive nuees ardentes in 1968 after 400 years of inactivity. The Cordillera de Tilaran is further to the southeast and is bounded in the north by a NW/SE-trending fault “Falla de Arenal” and is composed of late Tertiary volcanic and plutonic rocks. The Valle de Tempisque forms a broad depression between the Nicoya peninsula and Cordillera de Guanacaste. It is an area of subsidence that continues southward into the Gulf of Nicoya. Part of the Tempisque basin, to the southwest of the Cordillera de Guanacaste, is the Meseta Volcanica de Santa Rosa (Dengo, 1962). It is a plateau of Pleistocene ignimbrites, pumice tuffs, and re-worked products of these rocks (Weyl, 1980). The emerged outer arc includes the Santa Elena peninsula and the Nicoya peninsula and consists primarily of Late Cretaceous to Paleogene ophiolite massifs composed of oceanic crust, mantle (peridotites), basic/pelagic mélanges accreted along the edges of the Caribbean plate in deformed belts and volcanic rocks (Alvarado et al., 2007). The ophiolites and mélanges crop out along the Pacific coast of Central America next to the forearc. Locations are from NW to SE: Nicaragua forearc ophiolites, Santa Elena, Nicoya, Herradura, Quepos, Osa, and Burica Peninsulas and on into Panama (from oldest to youngest) (Hoernle and Hauff, 2007). The Nicoya Complex, named after the main occurrence on the Nicoya peninsula, is thought to have an affinity to the CLIP, and with the exception of parts of the Nicoya

complex, the Pacific coast can be thought of as a collage of fragments of ocean basins, oceanic seamounts, or island arcs (Weyl, 1980; Flueh and von Huene, 2007).

Although there is still debate about the origin of these oceanic suites and their emplacement in Costa Rica, structural and geochemical data indicate that the Nicoya, Herradura, Quepos, Osa, and Burica Peninsulas were derived from the Galapagos hot-spot and were tectonically juxtaposed onto the Caribbean plate due to movement from the Galapagos hot spot (DiMarco et al., 1995; Sinton et al., 1997; Hauff et al., 2000; Hoernle et al., 2004; Denyer et al., 2006). The Santa Elena Peninsula contains basaltic rocks with geochemical affinities different from those of the other massifs, suggesting an origin unrelated to the Galapagos (Beccaluva et al., 1999; Hauff et al., 2000). Early Late Cretaceous to Paleogene arc lavas in Central America are not well known and little has been published about them. Most are rare and if seen are as interbedded andesitic and dacitic lavas of Campanian to Maastrichtian in age (Alvarado et al., 2007).

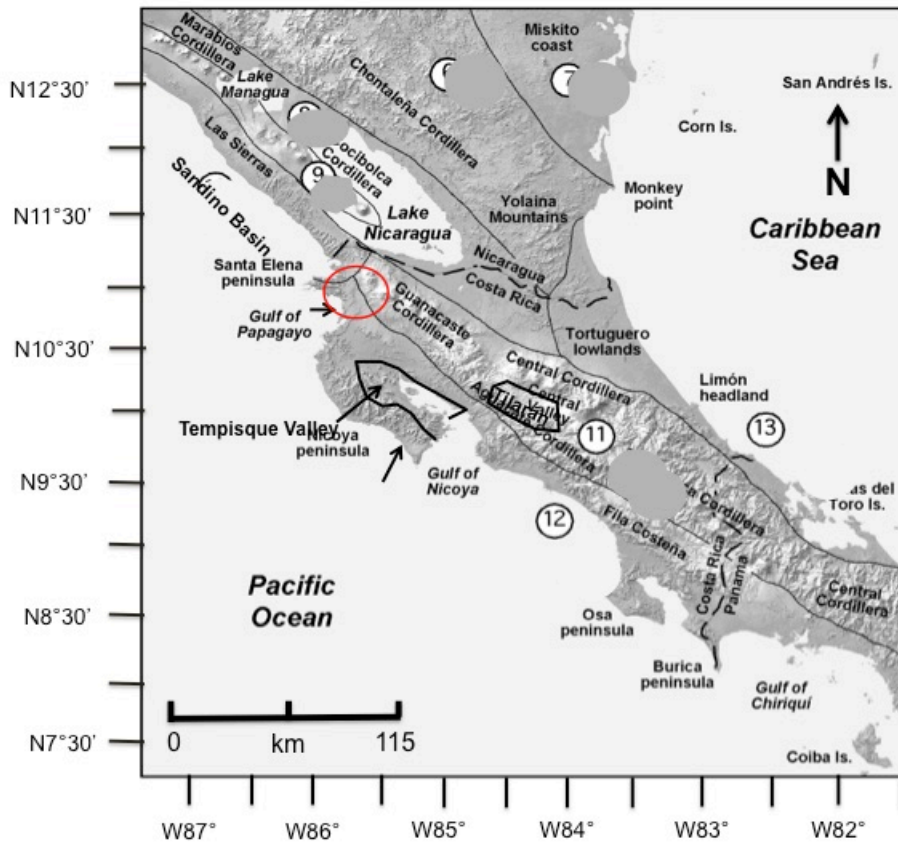


**Figure 1.** Map of geomorphologic regions of Costa Rica after Marshall (2007) with study area indicated by red circle.

### **Tectonics and volcanism**

Costa Rica is located on a triple junction of the Cocos, Nazca and Caribbean plates where the Cocos Plate is currently being subducted beneath the Caribbean plate at a rate of 88 mm / yr (DeMets, 1995). In the Late Cretaceous (between 95-72 Ma), an extensive period of volcanism thickened the Caribbean plate into an oceanic plateau referred to as the Caribbean Large Igneous Province (CLIP). From the Albian to Campanian (112-70 Ma), the thickened CLIP was moving eastward between the westward moving North and South American plates; the collision between Pacific and Caribbean plates caused ophiolitic bodies (such as the Santa Elena ophiolite) to be

obducted to the edge of the Caribbean plate (Pindell et al., 2006; Alvarado et al., 2007; Mann et al., 2007). Eastward dipping subduction initiated latest Santonian to early Campanian and in the late Campanian, there was uplift of the basement, which permitted large carbonate platforms to form on emerged or shallowly submerged areas, allowing for pelagic carbonate sedimentation to interfinger with coarse clastics near the margins (Galli-Oliver, 1979; Astorga et al, 1991; Ranero et al, 2000; Alvarado et al., 2007; Mann et al., 2007). Tholeiitic primitive arc volcanism initiated as early as 124 Ma to 83 Ma in Costa Rica (Seyfried et al., 1987; Alvarado et al., 2007). As subduction continued in the Maastrichtian, there was increased and profuse tholeiitic volcanism; from the late Maastrichtian to the Eocene, the andesitic island arc formed (Seyfried et al., 1987). As volcanism transitioned to an andesitic magma, rapid subsidence of the upper plate, driven by the slab sinking into the mantle, may have caused the initial opening of the forearc Sandino Basin, partially downing the carbonate platforms and causing differential raising of the outer arc and volcanic arc (Astorga, 1988; Astorga et al, 1991). The forearc basin would have been filled primarily with volcanoclastic sediments from developing arc with minor input from other sources along the trench; as the volcanic arc began to take hold and carbonate platforms drowned, sedimentation slowly transitioned from pelagic to hemipelagic carbonate sedimentation to gravity-driven mass flows of sandy fine-grained clastic turbidites that took hold by the Paleocene (Einsle, 2000; Ranero et al., 2007). The late Paleocene – early Eocene had relatively stable tectonics and development of explosive volcanism, causing uplift of the outer arc (Gose, 1983; Astorga et al 1991). During the lower Paleocene, smaller ephemeral carbonate platforms may have formed locally near the margins of the volcanic arc and along the shallow portions of the outer

arc (Astorga et al, 1991). Extensive shallow carbonate platforms proliferated on newly uplifted portions of the arc and around exposed terranes and island margins during volcanic quiet periods. Toward the end of the Eocene, volcanic activity began to decrease, represented by sedimentation characterized by sequences of mixed carbonate muds and fine-grained volcanoclastic turbidites (Gose, 1983; Seyfried et al, 1987; Astorga, 1988; Astorga et al., 1991).

### **Forearc basin development**

The formation of a volcanic island arc begins with plate subduction. A deep trench marks the boundary where the plates meet and on the overriding Caribbean plate, a volcanic island arc chain formed. Located between the arc and the trench is the forearc basin. The basement of the forearc may be formed of oceanic igneous rocks and basins formed on trapped oceanic crust may be deep initially, with large accommodation space for thick sediment deposits. As sediments load the forearc basin, it may subside even more, providing high levels of relief for easy erosion. The outer ridge of the basin, closer to the trench, acts as an emerged high and may also deposit sediments into the basin (Twiss and Moores, 1992; Einsle, 2000).

The forearc Sandino Basin is located along the continental shelf from the Gulf of Tehuantepec, Mexico to Costa Rica (Figures 2,3). It is 29,000 km<sup>2</sup>, with a NW-SE length of 250 km and a width of 100 km (Marshall, 2007). The basement of the Sandino Basin in NW Costa Rica and SW Nicaragua is oceanic Nicoya Complex (Jurassic to Late Cretaceous age) composed of primitive basalts that are ridge or ridge-like with CLIP affinities and late Cretaceous deep water sediment overlies Nicoya Complex igneous

rocks. This basin rapidly subsided during its early development (Cretaceous-Paleocene) and has been actively subsiding since the Late Cretaceous, with 9-15 km of sedimentary fill (Ranero et al., 2000; Ranero et al., 2007; Struss et al., 2008). Basin deposition began close to the present day coastline (Ranero et al., 2000, Walther et al., 2000). The sedimentary rocks of the Sandino Basin are dominantly clastic, deep water deposits with abundant volcanic tuffs and have been divided into five formations (the oldest are the Rivas and Descartes Formations) based on their lithostratigraphy, petrography and paleontology (Astorga, 1988; Kumpulainen, 1995). Where these deposits outcrop along the coast, they have been uplifted and folded since the Miocene, with a general NW-SE strike.

### **Paleocurrents and deposition**

Basin fill may be from the active arc or from basement rocks and is commonly deposited by turbidity currents that are either arc parallel along the basin axis or are orthogonal to the basin axis and follow the regional slope (Twiss and Moores, 1992). Initial forearc basin sedimentation may be characterized by pelagic to hemipelagic deposits, overlain by thick deposits of sand- and gravel-rich deep sea fans. Also common are channel fan systems fed by point sources along the arc (Einsle, 2000).

Liquefied mass flows, such as turbidity currents, need only very gentle slopes (< 0.5°) to initiate. In addition to slope angle, flow is driven by density differences in the overlying water body and the suspension. Typical sediment displacement volumes from mass transport complexes are on the order of  $10^3$  to  $10^6$  m<sup>3</sup>, can travel 100s kms up to 1,000 km from the original sediment input, and may have short recurrence intervals of

10s to 100s or 100s to 1000s of years (there may be an inverse relationship of bed thicknesses with depositional cycles) (Piper and Normark, 1983; Stow, 1986; Einsle, 2000). Thin-bedded turbidites are well known for their association with the Bouma sequence  $T_{abcde}$  divisions. They are commonly less than 50 cm thick, mud rich, and dominated by  $T_b$  (plane laminated sands) and  $T_c$  (ripple cross-beds due to current traction in low flow regime) divisions (see Figure 4b). These beds were deposited by turbidity currents with low sediment concentration that are low-density currents. Thick-bedded turbidites (greater than 50 cm thick) are the deposits of high-density turbidity currents. Beds may be graded or massive, with different grain populations: coarse grains larger than 3-5 cm diameter, pebbly to medium-grained sands, and medium-sized and finer sand grain sizes. Often these high-density flows are seen as part of submarine canyon fill (Lowe, 1982; Einsle, 2000; Lowe, 2004).

Sediment dispersal patterns are controlled by a combination of paleogeography, paleocurrents, exposed source rocks, and relative sea-level changes (Astorga, 1988). Paleocurrent directions may be identified based on the position of channel axes, erosional markings at the base of deposits, lateral variation and longitudinal thickness of lobes, and clast imbrication, such as the orientation of elongate axes of pebbles and cobbles. Based on paleocurrent indicators, deposition of Rivas and Descartes Formations was controlled by two perpendicular paleocurrent patterns in the basin, one transverse and the other longitudinal. The longitudinal pattern is generally parallel to the basin axis, or NW-SE, and is characteristic of basin plain turbidite deposits and large regional lobes. This pattern controls the majority of the sedimentation within the basin. The transverse pattern is seen in slump deposits, distributary channels and local lobes and is coincident

with the entry points of sediment into the basin (see Figure 21). Possible entry points include areas near the arc and hypothetical paleo-highs on the arc, along with paleocurrent directions during deposition of Rivas and Descartes Formations (Astorga, 1988).

### **Sedimentary deposits**

The arc-related deposits from the Late Cretaceous to Eocene Rivas and Descartes Formations (Figure 3) may generally be described as turbiditic sequences of volcanoclastic sediments, including tuffaceous shales, siltstones and sandstones, conglomerates, and breccias. The general volcanoclastic mineralogy consists of plagioclase, pyroxene, hornblende, variable quartz and rare biotite. Breccias and conglomerates are made up of basaltic, andesitic, and ignimbrite clasts from the arc. There is great variability in deposits from proximal to distal parts of the basin: deposits consist of hemipelagic to pelagic limestone deposits, submarine fans, submarine canyons with complete channel-lobe sequences (massive or graded sandstones) or locally derived mass-flow deposits (submarine slides, conglomeratic debris flows, slump masses) and thin-bedded low density turbidity current deposits prevailed (Weyl, 1980; Astorga, 1988; Astorga et al., 1991; Alvarado et al., 2007).

#### *Rivas Formation*

The Rivas Formation (Figure 3) is found in southern Nicaragua and on the Santa Elena peninsula. It is exposed on the northern edge of the peninsula and is a Maastrichtian to Late Paleocene volcanoclastic sedimentary section dominated by tuffaceous shales, sandstones and limestones (Weyl, 1980; Ranero et al., 2000;

Bergoeing, 2007; Struss et al., 2008). The exposed thickness of the formation ranges from a minimum of 600–800 m to a maximum of 2,500 m (Astorga, 1988; Ranero et al., 2000; Bergoeing, 2007). The upper boundary of the Rivas is defined as the basal conglomerate unit of the overlying Descartes Formation (Struss et al., 2008). The detrital grains are primarily of basaltic origins, and characterized by an abundance of feldspars, magnetite, and ferromagnesian minerals, with very low to absent-quartz content (Astorga 1988; Flores et al., 2003). The package displays cyclically intercalated sandstones and shales with some conglomerates and corresponds to turbidites of Maastrichtian to late Paleocene age. This deposit comprises two progradational depositional cycles and a third retrogradational cycle (Astorga 1988; Astorga et al., 1991).

Within this formation, 3 types of sedimentary deposits are: 1) basin plain turbidites, 2) lobe complexes, and 3) prograding channels. The basin plain turbidites and lobe complexes make up the majority of the deposit and alternate cyclically, with local occurrences of the channels. The basin plain turbidites are clay-dominated, sand-dominated, or a mix of the two types. The clay-dominated turbidites reflect low energy depositional environments that are in the very deep depositional areas, while the sand-dominated turbidites reflect high-energy deposits with an absence of pelagic sediments (Astorga, 1988; Astorga et al., 1991).

The lobe complexes are intercalated with the basin plain turbidites and represent times of major sediment input. These are composed of mainly sands mixed with clay and gravel in prisms of various thicknesses (10s-100s m) and deposited in the center of the basin. The lobes are elongate bodies with grain sizes larger than fine-medium with the larger, regional lobes having widths of 10s kilometers and smaller, local lobes with

widths of 100s meters. The lobes are composed of unorganized sandstones, organized sandstones, reworked turbidites, debris flows and sandy-pebbly unorganized turbidites. Lobe deposits generally make up the upper section of the progradational cycles (Astorga, 1988; Astorga et al., 1991).

Distributary channel deposits are meters to decameters wide and consist of coarse-grained facies of decimeter to meter thicknesses and are composed of organized breccias, unorganized conglomerates, sandy, organized conglomerates and debris flows. Deposits are interbedded with lobe and interlobe turbidites. These channels are not seen in the deep, submarine fan systems, but their presence indicates the proximity of a sediment entry point into the basin and their axes illustrate the direction of sediment input from the paleogeographic highs at the time (Astorga, 1988).

#### *Descartes Formation*

Located in the Guanacaste region in NW Costa Rica and exposed on the Descartes peninsula, in Manzanillo, and on the islands along the coast is the Descartes Formation (Figure 3). It overlies the Rivas Formation and is a 2,400 m-thick sequence of stacked deep water submarine fan deposits, late Paleocene to late Eocene in age (Weyl, 1980; Baumgartner et al., 1984; Boergoing, 2007). It contains sandstones, siltstones and claystones with an abundance of volcanics and feldspars. Carbonate ramps of middle to late Eocene age lie on top of Descartes deposits on the outer flanks of the basin (Ranero et al., 2000). The deposits have a maximum thickness of 1,600 m and consist of tuffitic arenites, intercalated with reef and foraminiferal limestones. The formation also contains

conglomerates, thick sandstones, shales, and calc-arenite deposits (Weyl, 1980; Astorga, 1988).

The base of the upper Paleocene is dominated by sediment gravity flows of basaltic composition that gradually change to an andesite-dominated detritus by the late Eocene (Denyer et al., 2005). Formation Descartes represents two different stages of deposition, demonstrating the geologic evolution of the area. The first is dominantly fine-grained low density turbidite sedimentation from the late Paleocene to late Eocene with only locally interbedded fans and lobes. The second stage is dominated by fans and lobes with distributary channel fills that are cyclically interbedded with fine-grained turbidite deposits. These deposits are composed of medium grey sands with centimeter intercalations of shales and fine calcareous sands, horizons of massive limestones, bioclastic limestones, calcarenites, breccias and calcareous conglomerates. (Astorga 1988; Astorga et al., 1991; Denyer et al., 2005).

Formation Descartes is characterized by basin plain turbidites, lobe complexes and local fan and channel fill deposits (Astorga 1988; Astorga et al., 1991). Turbidite deposits are of volcanoclastic composition with regularly alternating sands and shales, thin to thick stratification, and a wide lateral extent. Based on sand and clay contents, they are divided into sandy, shaley or mixed-type turbidites. Within turbidite deposits are thin interbedded lobes, channel-fill deposits and pelagic–hemipelagic deposits. The lobe complexes show facies of sands, pebbly sands, sandy conglomerates and conglomerates (organized and unorganized) with interlobular turbidite deposits. The local fans formed during a time of intense and continuous erosion at paleogeographic highs and were deposited at the base of submarine canyons by sediment gravity flows.

They have a lateral extent of 7-8 kms, a maximum thickness of 600 m, and are laterally discontinuous. Distributary channel deposits fill isolated erosive channels and vary in thickness from meters to decameters. The facies within the distributary channels are coarser grained and are composed of unorganized sandstones, organized sandstones, unorganized pebbly sandstones, unorganized sandy conglomerates, unorganized conglomerates, organized sandy breccias and organized conglomerates (Astorga, 1988; Astorga et al., 1991).

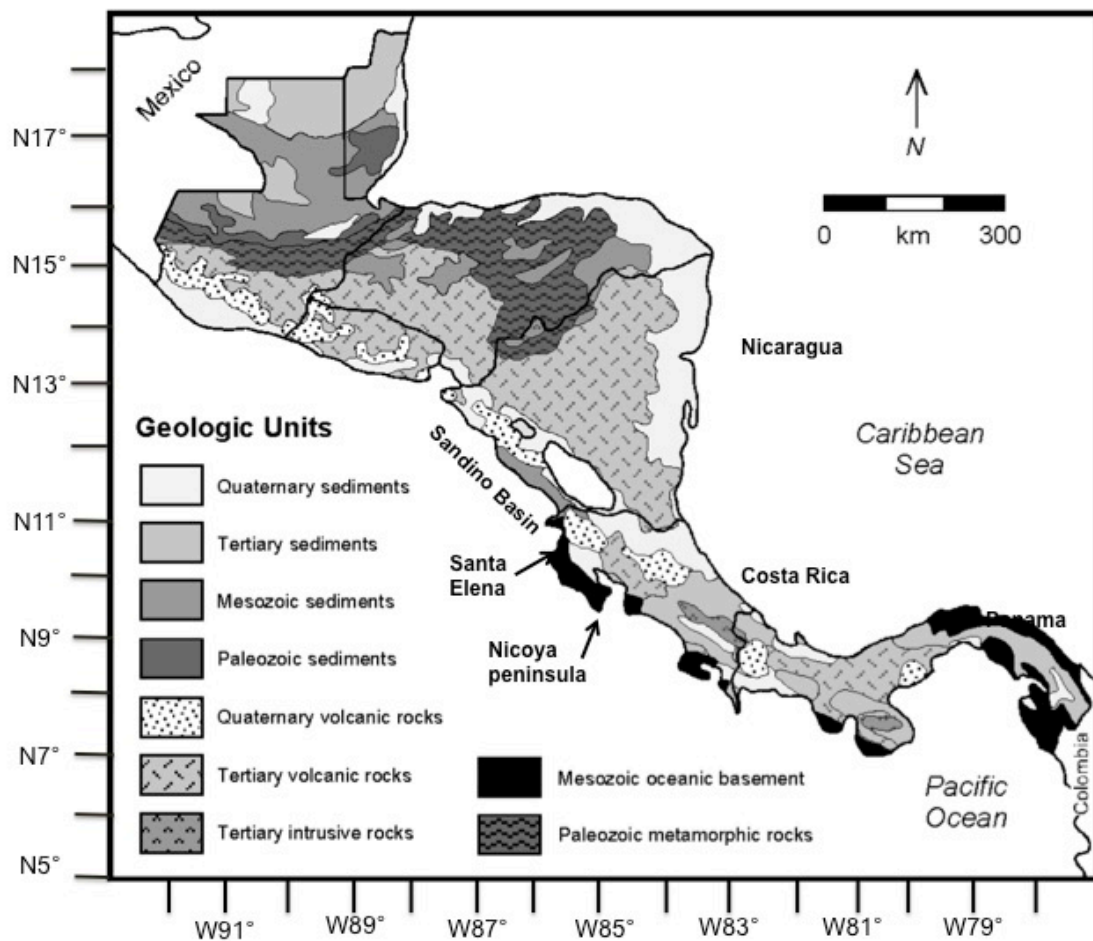


Figure 2. Geologic map of Central America after Marshall (2007).

## **Geologic setting of potential sedimentary source rocks**

The Santa Elena peninsula (Figures 1-3) is located on the west coast of Northern Costa Rica and is 40km long (EW) by 16km wide (NW). The peninsula itself is made up of a large peridotite body (Santa Elena ophiolite complex) thrust onto an igneous - sedimentary sequence that makes up the Santa Rosa accretionary complex (Baumgartner and Denyer, 2006; Gazel et al., 2006) (Figure 3). A prominent Caribbean rudist limestone lies unconformably on top of the Santa Elena thrust slice, suggesting shallow emergence of the ophiolite under Caribbean waters at the end of the Campanian (70.6 Ma) (Schmidt-Effing, 1980). Based on this evidence, exhumation and exposure of the Santa Elena ophiolite complex occurred sometime between the Cenomanian (99.6) and the end of the Campanian (70.6 Ma). The ophiolite body is in fault contact with the sedimentary rocks of the Rivas Formation on the northern part of the peninsula.

### *Santa Elena Ophiolite*

Santa Elena peninsula ophiolite massif is a thrust sheet with east-west trending thrust faults that carry dominantly ultramafic to mafic rocks the hanging wall. The ophiolite complex (see Figure 3) is a hanging wall thrust sheet that consists primarily of serpentinized peridotites, but also has minor instances of layered and pegmatitic gabbros, doleritic and basaltic dikes, and plagiogranites. Peridotites are dominantly lherzolite and clinopyroxene-bearing harzburgite (Gazel et al., 2006; Wright, 2011). Dunite is present in small areas. K/Ar geochronology of amphiboles within the series of doleritic dikes indicate an age of  $88 \pm 4.5$  Ma (Bellon and Tournon, 1978). The dike rocks display arc-related tholeiitic to transitional calc-alkaline affinities (Denyer and Gazel, 2009),

depletion of light rare earth elements (LREE) and enrichment of large-ion lithophile elements (LILE) and Pb (Gazel et al., 2006; Wright, 2011).

### *Santa Rosa Accretionary Complex*

The Santa Rosa accretionary complex (Figure 3) lies structurally below the Santa Elena thrust slice in the footwall of the thrust. This accretionary complex consists of vesicular pillowed and alkaline basalt flows, alkaline sills, ribbon and massive radiolarites, detrital and volcanoclastic turbidites, pelagic limestones, black shales, and polymictic megabreccias associated with thrust faulting (Baumgartner and Denyer, 2006). Rocks of the accretionary complex also seen in the Potrero Grande tectonic window in the central part of the peninsula (Azema and Tournon, 1980). Biostratigraphic ages from the youngest radiolarite of the accretionary complex indicate that thrust faulting and juxtaposition of the ultramafic thrust sheet occurred after the Cenomanian (99.6-93.5 Ma) (DeWever et al., 1985).

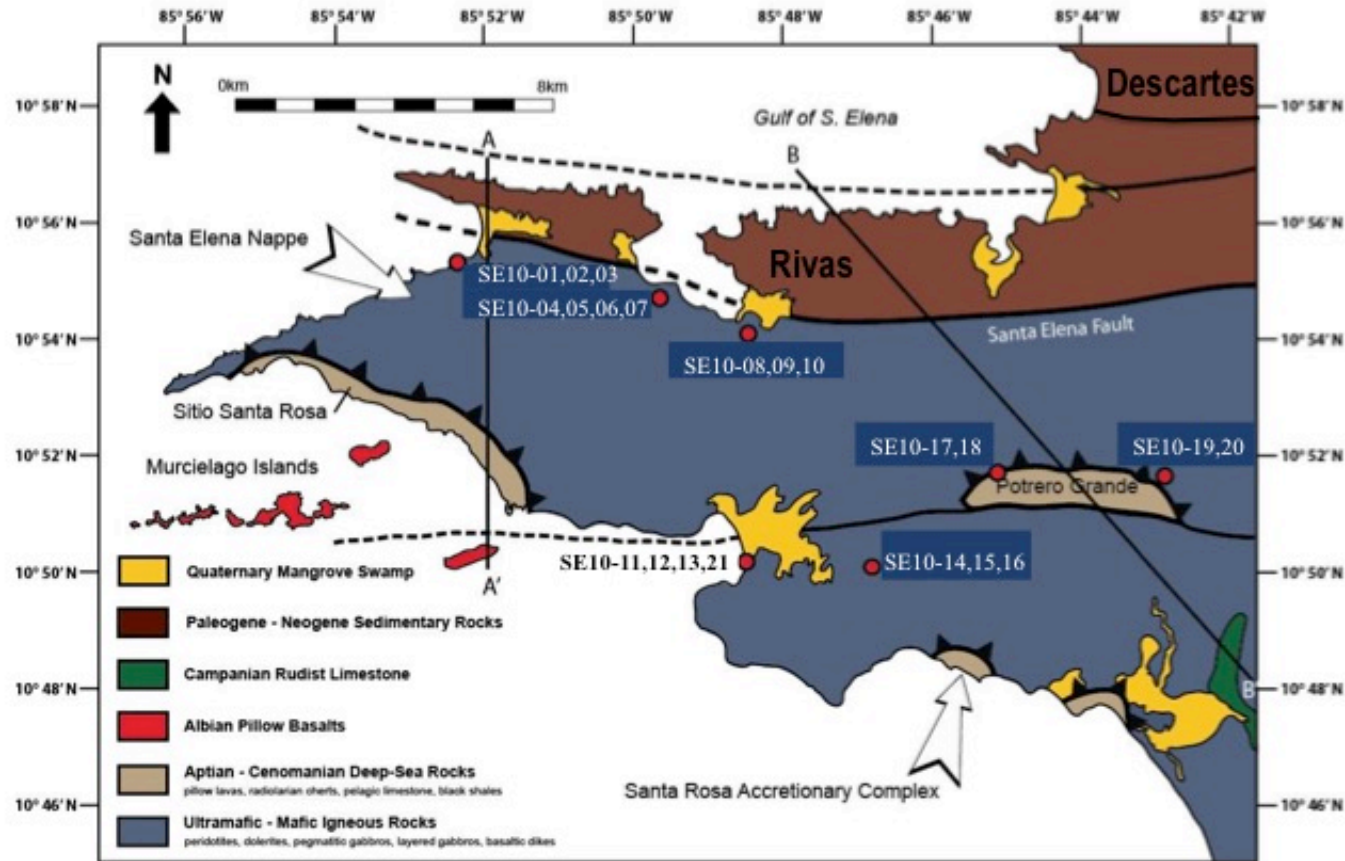


Figure 3. Geology of Santa Elena Peninsula modified after Wright (2011). Map shows locations of Rivas and Descartes sedimentary deposits (brown), Santa Elena ophiolite complex (blue), Santa Elena accretionary complex (grey), and the tholeiitic Murciélago Islands (red). Ophiolite samples taken at locations indicated by red circles.

### *Nicoya Complex*

The oceanic crust exposed on the Nicoya peninsula (Figures 1,2) is called the Nicoya complex (Dengo, 1962). It is made up of massive and pillow tholeiitic basalts, gabbros, and plagiogranites with some radiolarian chert (Weyl, 1980; Alvarado et al., 1992; Bergoeing, 2007). Sinton et al. (1997) found that the mafic oceanic rocks of the Nicoya Peninsula are from a single magmatic suite, formed within a short period from 88-90 Ma. More recent geochemical work by Hauff et al. (1997), Hauff et al. (2000) and Hoernle et al. (2004) has shown that the Nicoya igneous rocks are a portion of the Caribbean Plateau or of plateau geochemically similar to the Eastern Pacific Rise.

Southern Central America (Costa Rica and Panama) has no Paleozoic crystalline basement, rather the oldest basement rocks are oceanic and volcanic, dating back to the Cretaceous and are overlain by Tertiary to Holocene volcanics and sediments, which reflect a change in magma types from tholeiitic to andesitic to more felsic arc magmas. Some of the proposed sediment source rocks are seen along the Pacific northwest coast of Costa Rica (see Figures 1-3) and on the Santa Elena peninsula, including Mesozoic ophiolites, peridotites and basalts (massive and pillows), along with radiolarites, dolerites, rudist limestones, volcanoclastics and igneous intrusive rocks (plagiogranites, gabbros) (Calvo et al., 2003; Gazel, et al., 2006; Alvarado et al., 2007; Wegner et al., 2011). All of these rock types may be found along the entire Pacific coast of Central America and all are potential sediment source inputs, including the serpentinite bodies, remnants of the oceanic CLIP, and tholeiitic and andesitic volcanics. Understanding the sediment input of the Rivas and Descartes Formation deposits in the Sandino Basin may

lead to a better understanding of the Late Cretaceous to Paleogene arc compositions, which contributed to the eventual closing of the seaway in the Miocene and to significant changes in global climate.

## **Analytical Methods**

### **Sample collection**

Fifty one samples were collected over 2010–2011 from exposures of the Rivas Formation on the north side of Santa Rosa National Park, from beaches outside of the park (Cuajiniquil, Junquillal), and from pocket beaches accessed from the northern coastal road leading to the Descartes peninsula (Rajada, Copal, Manzanilla) (see Figure 4a). Exact sample locations are shown in Figure A-1 in the Appendix. Observed Rivas Formation turbidites were primarily fine- to very fine-grained low-density turbidity current deposits. Bouma divisions were seen in the deposits (Figure 4b) and showed coarser grained, massive beds ( $T_a$ ) fining upwards into finer grained, parallel beds ( $T_b$ ). Cross-bedding ( $T_c$ ) was observed infrequently on top of the  $T_b$  deposits. Conglomeratic deposits with andesitic pebbles to boulders were observed in the Descartes Formation deposits at Playa Junquillal and on the Descartes peninsula (Figures 4a,b). At Punto Pulpo, a fault contact between the Santa Elena ophiolite complex pillow basalts and Rivas Formation turbidite beds was observed (Figure 4a).

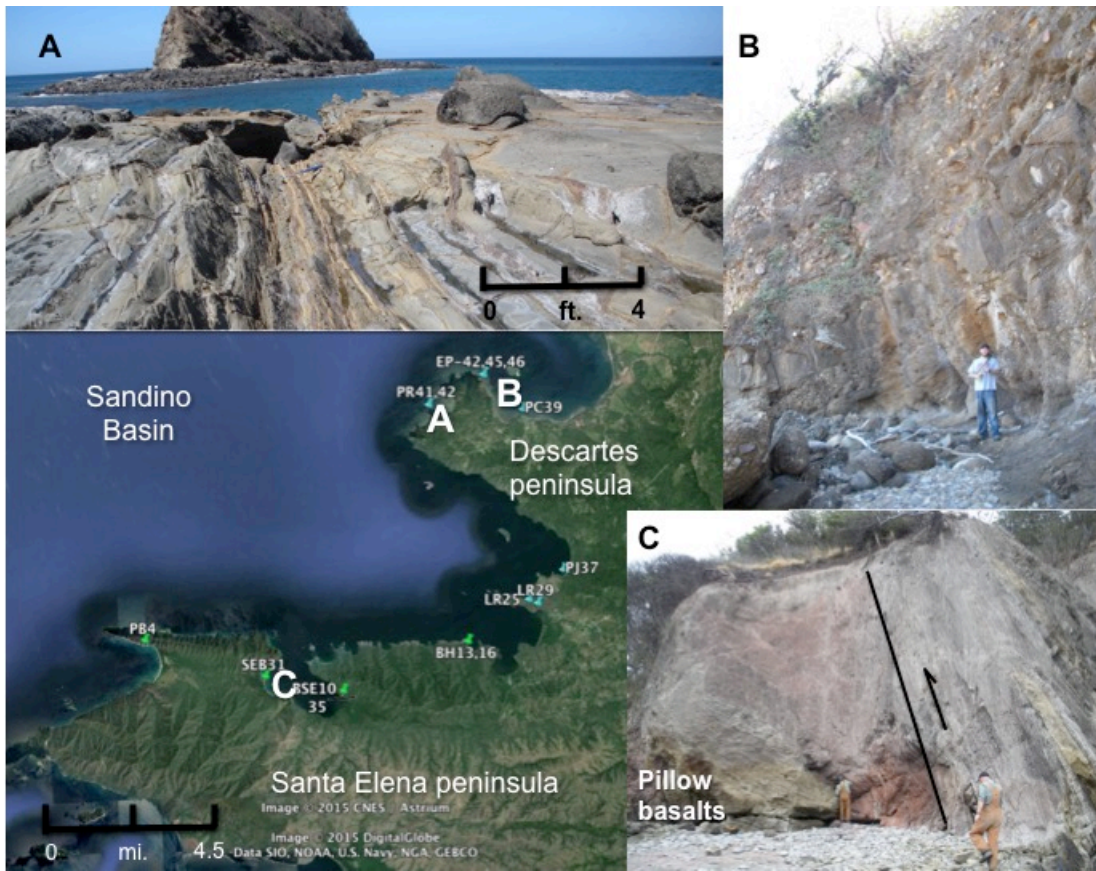


**Figure 4a.** Map with sample locations (lower left corner) and photographs of outcrops that reference map locations. Clockwise from top left corner: A) Dipping turbidite outcrops of Descartes Formation at Playa Rajada (PR). Turbidites were primarily low density turbidity current deposits with very fine grained to pebbly grain sizes. Strikes and dips indicate a plunging fold at this location. B) Pebbly to boulder conglomerate fining upward sequences at Ecoplaya beach (EP) location (S. Wright for scale) from the Descartes Formation. Boulders have volcanic origins – andesites and ignimbrites. C) Turbidite section at Punto Pulpo in Bahia Santa Elena (BSE) showing steeply dipping, upward thrust turbidite section from Rivas Formation against pillow basalts of the Santa Elena ophiolite (S. Wright and M. Loocke for scale).

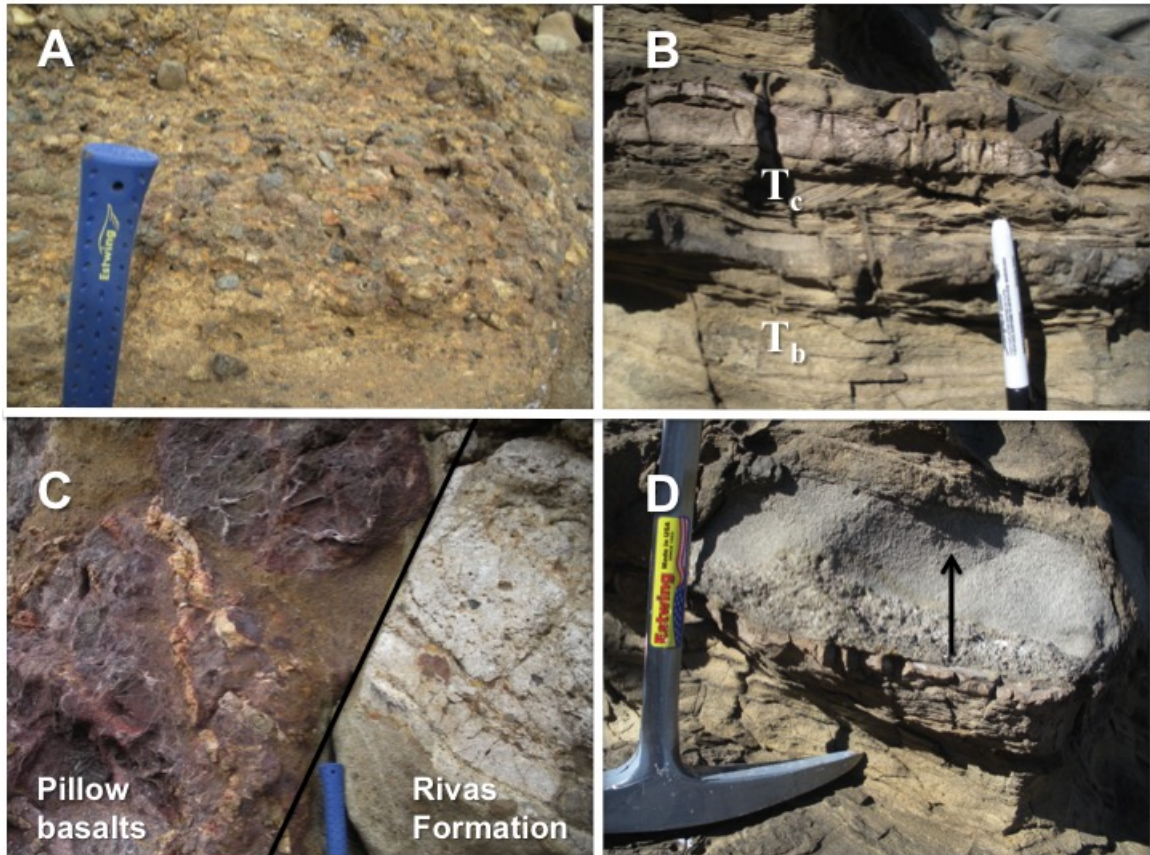


**Figure 4b.** Photographs of outcrops and sedimentary features from different sample locations. Location references sample location map in Figure 4a. From top left corner: A) Pebbly conglomerate at Playa Junquillal (map location E). Pebbles have volcanic origins. B) Sample location at Bahia Hachal (BH). Turbidite bed showing first-order architectural elements of lower flat laminated beds (Bouma designation  $T_b$ ) underlying cross-laminated beds ( $T_c$ ) at map location D. C) Fault contact at Punto Pulpo (map location C) showing pillow basalts of the Santa Elena complex juxtaposed against a massive turbidite deposit of the Rivas Formation. D) Fining upwards turbidite bed (BH) with very coarse grains at the base grading upwards in to medium grain sizes

### **Sample preparation**

Of the original 51 samples collected, 18 were then selected for further processing and crushed initially in a jaw crusher and later crushed by hand with a mortar and pestle. The samples were then washed to take out the remaining clay particles and heavy minerals were separated in a column using methylene iodide (specific gravity of 3.32

gm/cm<sup>3</sup>). Next, the samples were dried and magnetite was removed with a hand magnet. Heavy mineral grains were picked under a microscope to isolate grains for analysis, covered with epoxy, and cured. Once the samples were dry, they were polished using a combination of polishing grit and papers, starting at size 1500, 2000, 2500, 3000, 5 micron grit and lastly 1 micron grit of high-purity alumina. Once a smooth surface was obtained, samples were then carbon coated to ensure conductivity and prepared for the microprobe analysis.

### **Electron microprobe analysis**

Analyses were made using a Cameca SX 50 electron microprobe (EMP) at the University of Houston in Houston, Texas, which is equipped with four wavelength dispersive (WDS) spectrometers and one energy dispersive (EDS) spectrometer. The locations of all mineral phases that were analyzed were recorded for consistency with electron microprobe analysis (EMPA) and laser ablation inductively coupled plasma mass spectrometry (LA-ICP-MS) analyses (Figure 5). Over 300 energy-dispersive spectrometry (EDS) analyses were determined for a suite of heavy minerals (HM) from 18 samples. The analytical conditions were: accelerating potential of 15 kV, a beam current of 10 nA, and a spot size of 10 microns, with a counting time of 100 seconds. Heavy mineral phases were determined during the EDS (Figure 5). The number of grains for each sample varied from 40 – 100 per ring.

Wave-dispersive spectrometry (WDS) to measure heavy mineral chemistry was performed with the EMP on the mineral phase clinopyroxene. For clinopyroxene analysis an accelerating voltage of 15 kV and a beam current of 20 nA were used. I

measured Si, Ti, Al, Fe, Mn, Mg, Ca, Na, K, F and Cl. Spectrometer 1 with the LIF crystal was used to measure Mn. A natural standard, rhodonite, was used for Mn. Spectrometer 2 has the TAP crystal and was used to measure F, Na, Mg and Al. F was calibrated with synthetic MgF while the rest were natural standards, jadeite for Na, diopside for Mg, and garnet for Al. Spectrometer 3 with a PET crystal was used for Cl, which was calibrated with tugtupite. Spectrometer 4 with a PET crystal was used to measure K and Ti, each calibrated on natural standards of microcline for K and rutile for Ti. The counting time was set at 20 seconds with a background count time of 10 s for all but F and Cl, which had count times of 40 s with background counts of 20 s. Ca, Fe and Si were measured with EDS concurrently with WDS measurements for a count time of 100 s. During analysis random standard analyses were performed to ensure that mechanical drift had not occurred and affected the analytical results. Analyses that returned greater than 102% or less than 97 % were rejected. Another criterion for sample rejection was misidentification of phases (e.g. too much TiO in what looked like pyroxene). When necessary grain mounts were repolished to get smoother surfaces and recoated in carbon to return more acceptable totals.

Repeat analyses of a primary standard of known measurements were done to standardize the EMP. Sample standard bracketing was performed by measuring 5-6 points, then re-measuring the standard. Lastly measuring a secondary, external standard allowed assessment of both accuracy and precision of the measurements. The best estimate of analytical precision and accuracy is repeat measurements of external standards and the standard deviation of the standard measurements is the best estimate of overall error. Error results can be found in Table A-2 and A-3 in Appendix II. General

factors that can affect analytical precision may be due to both systematic and random error, including the random nature of X-ray generation, short- term filament instability, sample charging, sample heterogeneity and specimen surface irregularities. Specimen surface irregularities were minimized by adequate thin section polishing, surface charging was addressed by ensuring carbon coating was thick enough, and care was taken while loading the sample shuttle to ensure a good airlock while pumping to a vacuum.

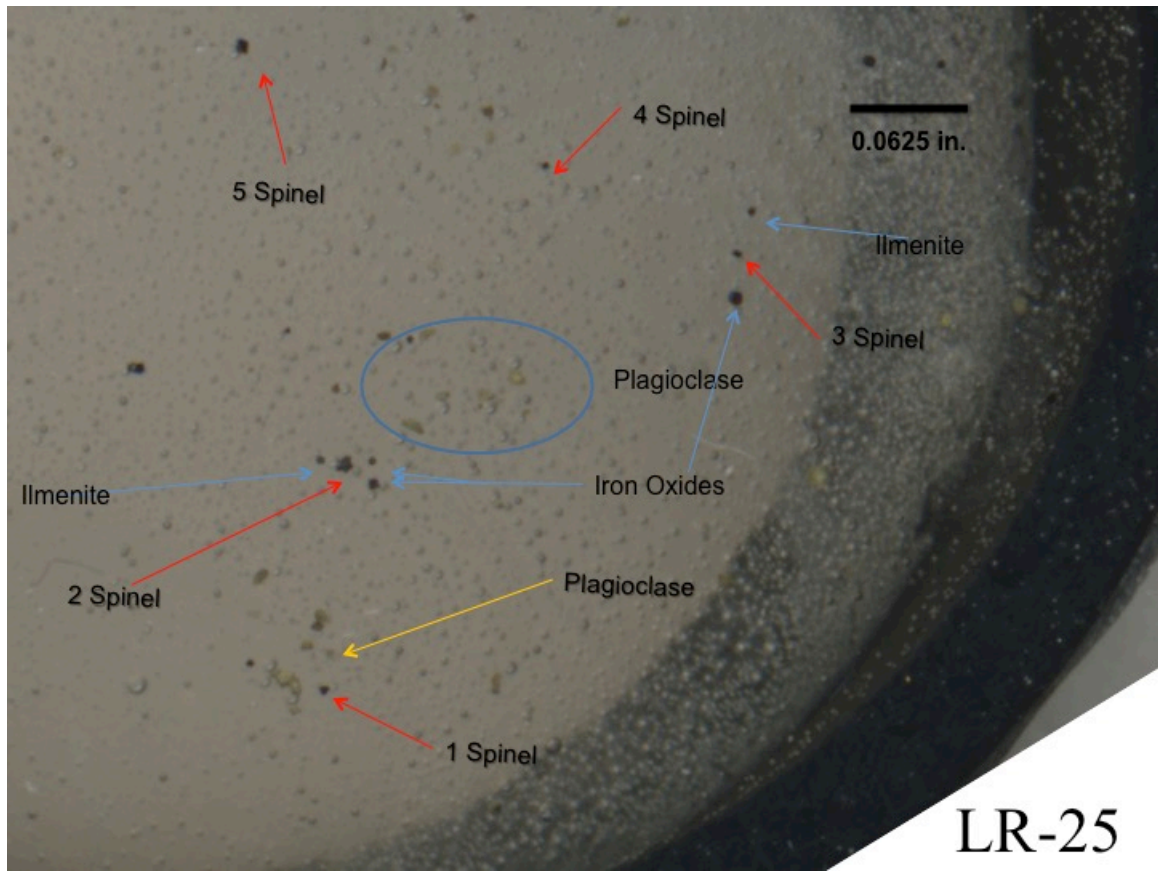


Figure 5. Image of grain mount with detrital heavy minerals for sample LR-25 identified using EDS.

## **Laser ablation inductively-coupled mass spectrometry**

Measurements of trace elements in clinopyroxene grains were done on a Varian quadrupole inductively coupled plasma mass spectrometer (ICP-MS) using a CETAC laser ablation sample introduction system with a 213 nm laser wavelength at the University of Houston. In-situ measurements on minerals in grain mounts were made at a 10 Hz shot rate and ranged from 150-170 bursts, resulting in 30-35 second measurement times. Three grains in five different samples were measured, with three spots measured on each grain. Spot sizes of 30  $\mu\text{m}$  were used on each grain. Repeat analyses of a primary standard – tholeiitic basalt glass KLG-2 – and a secondary standard – rhyolite glass ATH0 – were performed to test instrument stability and data reproducibility. Magnesium concentrations measured by the microprobe were used to correct drift of measured trace element ratio concentrations, as well as standard bracketing by measuring both standards between every 6 points. The data were reduced using an in-house laser ablation software package. Analytical precision of the LA-ICP-MS was determined similarly to the electron microprobe. Standard error analyses, including averages and standard deviations, can be found in tables A-4 and A-5 in Appendix II. Errors on repeat standard analyses were between 3 and 8% for most elements for the KLG standard and between 2 and 9% for the ATHO standard. Inaccuracy in measurements may be influenced by mechanical instability (both the laser ablation mechanism and the ICPMS), heterogeneity of the detrital grains, and data reduction errors, including uncertainties in standard corrections.

Table 1. Clinopyroxene Major Elements (1of 6)

Clinopyroxene Major Elements												
Sample Mineralogy	BH13-03 Diopside	BH13-04 Augite	BH13-05 Augite	BH13-06 Augite	BH13-07 Diopside	BH13-08 Augite	BH13-09 Augite	PR41-01 Augite	PR41-05 Augite	PR41-07 Augite	PR41-13 Augite	
Na <sub>2</sub> O	0.3	0.3	0.2	0.2	0.2	0.3	0.3	0.4	0.3	0.3	0.4	
MgO	14.9	15.8	16.4	15.4	16.5	15.3	15.1	15.2	14.8	15.5	15.7	
SiO <sub>2</sub>	49.5	51.5	51.6	51.6	52.0	52.0	51.7	52.0	51.1	52.1	51.4	
Al <sub>2</sub> O <sub>3</sub>	4.9	2.4	2.6	2.4	3.0	1.7	1.7	2.0	1.4	1.7	2.2	
K <sub>2</sub> O	0.0	0.0	0.0	0.0	0.0	0.0	0.0	0.0	0.0	0.0	0.0	
CaO	22.3	20.1	20.0	20.4	22.0	20.4	20.4	20.9	19.7	20.4	19.7	
TiO <sub>2</sub>	0.5	0.4	0.4	0.3	0.3	0.4	0.4	0.5	0.6	0.5	0.6	
Cr <sub>2</sub> O <sub>3</sub>	0.1	0.0	0.1	0.0	0.5	0.0	0.0	0.0	0.0	0.0	0.0	
MnO	0.1	0.2	0.2	0.4	0.1	0.5	0.6	0.4	0.8	0.6	0.4	
FeO	2.9	6.7	5.9	7.0	3.7	7.3	7.3	6.6	7.5	6.9	6.8	
Fe <sub>2</sub> O <sub>3</sub>	4.2	3.3	3.4	2.8	2.6	1.6	3.2	3.1	3.7	3.2	3.9	
Total	99.8	100.6	100.8	100.4	100.9	99.4	100.5	101.0	100.0	101.2	101.0	
Wo	0.491	0.425	0.422	0.431	0.460	0.431	0.434	0.443	0.427	0.431	0.421	
En	0.459	0.466	0.481	0.452	0.480	0.449	0.445	0.448	0.446	0.456	0.466	
Fs	0.050	0.110	0.098	0.116	0.060	0.120	0.120	0.109	0.127	0.113	0.113	
Cr#	1.4	1.0	3.4	0.0	10.3	0.0	0.0	0.0	1.5	1.3	0.0	
Mg#	90.1	80.9	83.1	79.5	88.9	79.0	78.7	80.4	77.8	80.1	80.5	

Table 1. Clinopyroxene major and minor element concentrations (wt. % oxide) from electron microprobe analyses at University of Houston and Texas A&M University.

Table 1. Clinopyroxene Major Elements (2 of 6)

Clinopyroxene Major Elements										
Sample Mineralogy	EP45-05 Augite	EP45-07 Augite	EP45-08 Augite	EP45-09 Augite	EP45-10 Augite	EP42b-01 Augite	EP42b-02 Augite	EP42b-03 Augite	EP42b-04 Augite	EP42b-05 Augite
Na <sub>2</sub> O	0.3	0.3	0.3	0.2	0.2	0.2	0.3	0.2	0.2	0.2
MgO	15.6	14.2	13.3	13.9	14.2	15.4	14.3	15.5	15.8	12.7
SiO <sub>2</sub>	51.8	51.2	49.5	51.4	51.7	51.5	50.8	51.2	51.4	51.3
Al <sub>2</sub> O <sub>3</sub>	2.2	1.3	1.8	1.2	1.3	2.3	2.1	3.1	2.6	1.1
K <sub>2</sub> O	0.0	0.0	0.0	0.0	0.0	0.0	0.0	0.0	0.0	0.0
CaO	19.5	19.3	19.1	19.3	19.5	20.1	19.0	21.0	20.1	19.1
TiO <sub>2</sub>	0.5	0.4	0.4	0.4	0.4	0.6	0.6	0.6	0.5	0.4
Cr <sub>2</sub> O <sub>3</sub>	0.0	0.0	0.0	0.0	0.0	0.0	0.0	0.0	0.0	0.0
MnO	0.5	0.8	0.9	0.8	0.8	0.4	0.5	0.3	0.3	0.8
FeO	7.7	9.4	9.2	10.3	10.1	7.4	9.9	5.9	6.6	12.7
Fe <sub>2</sub> O <sub>3</sub>	2.2	2.3	3.4	2.2	1.5	3.1	3.0	3.7	3.6	2.2
Total	100.2	99.2	97.7	99.9	99.7	100.8	100.3	101.4	101.1	100.5
Wo	0.413	0.417	0.427	0.414	0.413	0.425	0.408	0.445	0.426	0.408
En	0.460	0.425	0.413	0.414	0.419	0.454	0.427	0.458	0.465	0.380
Fs	0.127	0.159	0.160	0.173	0.168	0.121	0.166	0.097	0.109	0.212
Cr#	0.0	0.0	1.2	0.0	0.0	0.0	1.1	0.0	0.0	0.0
Mg#	78.3	72.8	72.0	70.6	71.5	78.9	72.0	82.5	80.9	64.2

Table 1. Clinopyroxene major and minor element concentrations (wt. % oxide) from electron microprobe analyses at University of Houston and Texas A&M University.

Table 1. Clinopyroxene Major Elements (3 of 6)

Clinopyroxene Major Elements										
Sample	EP42b-06	EP42b-07	EP42b-08	EP42b-09	PR24-27	PR42-49	PR42-50	PR42-38	PR42-39	EP46-07
Mineralogy	Augite	Augite	Augite	Diopside	Augite	Augite	Augite	Diopside	Augite	Augite
Na <sub>2</sub> O	0.2	0.3	0.3	0.2	0.2	0.3	0.2	0.2	0.3	0.2
MgO	13.0	15.7	15.5	15.3	15.5	15.0	15.8	15.2	15.4	13.6
SiO <sub>2</sub>	51.2	51.2	50.6	50.2	51.2	50.7	51.6	50.6	51.1	52.2
Al <sub>2</sub> O <sub>3</sub>	1.4	2.5	2.3	4.1	2.9	2.3	2.5	3.3	2.1	1.2
K <sub>2</sub> O	0.0	0.0	0.0	0.0	0.0	0.0	0.0	0.0	0.0	0.0
CaO	19.3	20.4	19.9	22.0	20.6	19.5	20.2	21.6	19.8	19.8
TiO <sub>2</sub>	0.5	0.6	0.6	0.5	0.5	0.8	0.5	0.5	0.6	0.4
Cr <sub>2</sub> O <sub>3</sub>	0.0	0.0	0.0	0.4	0.0	0.0	0.0	0.0	0.0	0.0
MnO	0.8	0.4	0.3	0.2	0.3	0.4	0.2	0.2	0.4	0.8
FeO	11.9	6.0	6.4	3.8	6.2	8.0	6.8	5.0	7.1	11.2
Fe <sub>2</sub> O <sub>3</sub>	2.0	3.9	4.2	4.1	3.3	2.9	2.7	3.9	3.4	1.6
Total	100.3	101.0	100.0	100.8	100.7	99.7	100.5	100.5	100.3	101.1
Wo	0.414	0.435	0.428	0.475	0.459	0.449	0.464	0.453	0.458	0.397
En	0.387	0.465	0.464	0.461	0.103	0.134	0.111	0.083	0.119	0.185
Fs	0.199	0.101	0.108	0.064	0.439	0.417	0.425	0.464	0.423	0.418
Cr#	0.0	0.0	1.0	6.3	0.0	0.0	0.0	0.0	0.0	0.0
Mg#	66.0	82.2	81.2	87.7	81.7	77.0	80.6	84.6	79.4	68.3

Table 1. Clinopyroxene major and minor element concentrations (wt. % oxide) from electron microprobe analyses at University of Houston and Texas A&M University.

Table 1. Clinopyroxene Major Elements (4 of 6)

Clinopyroxene Major Elements										
Sample Mineralogy	EP46-37 Augite	EP46-21 Augite	EP46-38 Augite	EP46-18 Augite	EP46-39 Augite	EP46-40 Augite	EP46-29 Augite	EP46-41 Augite	EP46-42 Augite	SE10-25-1 Augite
Na <sub>2</sub> O	0.2	0.2	0.3	0.3	0.2	0.3	0.2	0.3	0.2	0.2
MgO	13.9	13.8	14.2	13.9	13.6	13.0	13.3	13.8	13.0	13.6
SiO <sub>2</sub>	52.0	51.6	51.4	51.7	51.2	50.6	51.0	51.3	50.9	52.5
Al <sub>2</sub> O <sub>3</sub>	1.2	1.4	1.7	1.4	1.3	1.4	1.3	1.3	1.3	1.7
K <sub>2</sub> O	0.0	0.0	0.0	0.0	0.0	0.0	0.0	0.0	0.0	0.0
CaO	19.9	19.1	19.5	19.9	19.7	19.5	19.4	19.6	19.4	20.7
TiO <sub>2</sub>	0.4	0.4	0.5	0.4	0.4	0.5	0.5	0.5	0.5	0.4
Cr <sub>2</sub> O <sub>3</sub>	0.0	0.0	0.0	0.0	0.0	0.0	0.0	0.0	0.0	0.0
MnO	0.8	0.8	0.7	0.8	0.8	0.8	0.9	0.9	0.9	0.4
FeO	10.5	11.2	9.6	9.8	10.1	10.8	11.0	10.0	11.1	10.4
Fe <sub>2</sub> O <sub>3</sub>	1.8	1.6	2.5	2.5	1.8	2.1	1.8	2.3	2.4	0.0
Total	100.7	100.1	100.5	100.7	99.2	98.9	99.2	99.9	99.7	100.0
Wo	0.409	0.408	0.423	0.413	0.407	0.393	0.398	0.412	0.392	0.394
En	0.172	0.185	0.160	0.163	0.170	0.183	0.185	0.167	0.188	0.175
Fs	0.419	0.407	0.417	0.424	0.424	0.424	0.417	0.421	0.420	0.431
Cr#	0.0	0.0	0.0	0.0	0.0	0.0	0.0	0.0	0.0	0.0
Mg#	70.3	68.8	72.6	71.7	70.6	68.2	68.3	71.1	67.6	69.2

Table 1. Clinopyroxene major and minor element concentrations (wt. % oxide) from electron microprobe analyses at University of Houston and Texas A&M University.

Table 1. Clinopyroxene Major Elements (5 of 6)

Clinopyroxene Major Elements										
Sample	PR41-14	PR41-15	SE10-25-01	SE10-25-03	SE10-25-06	SE10-25-07	SE10-25-08	SE10-25-09	SE10-25-10	EP45-03
Mineralogy	Diopside	Augite	Augite	Augite	Augite	Augite	Augite	Augite	Augite	Augite
Na <sub>2</sub> O	0.2	0.3	0.3	0.3	0.3	0.3	0.3	0.3	0.2	0.3
MgO	16.0	15.8	14.6	15.4	14.9	14.9	15.8	14.9	14.9	14.0
SiO <sub>2</sub>	50.7	51.7	51.1	51.1	51.3	51.1	50.9	50.8	51.7	51.1
Al <sub>2</sub> O <sub>3</sub>	4.0	3.0	1.9	2.5	2.8	2.1	3.3	2.3	1.5	1.1
K <sub>2</sub> O	0.0	0.0	0.0	0.0	0.0	0.0	0.0	0.0	0.0	0.0
CaO	22.4	20.3	20.3	19.9	20.0	19.8	21.0	20.6	19.4	18.8
TiO <sub>2</sub>	0.3	0.5	0.4	0.4	0.4	0.4	0.6	0.5	0.4	0.4
Cr <sub>2</sub> O <sub>3</sub>	0.3	0.0	0.0	0.1	0.0	0.0	0.2	0.0	0.0	0.0
MnO	0.2	0.3	0.5	0.3	0.4	0.4	0.2	0.4	0.6	1.0
FeO	2.8	6.6	7.5	7.0	7.5	8.2	5.0	6.4	9.1	10.4
Fe <sub>2</sub> O <sub>3</sub>	4.1	3.5	3.4	3.4	3.1	3.0	3.8	3.8	2.4	2.9
Total	101.0	101.8	100.0	100.3	100.8	100.2	100.9	99.9	100.2	99.8
Wo	0.478	0.428	0.437	0.427	0.429	0.422	0.448	0.445	0.410	0.405
En	0.475	0.463	0.437	0.458	0.445	0.422	0.469	0.447	0.440	0.420
Fs	0.047	0.109	0.126	0.118	0.126	0.136	0.083	0.108	0.150	0.176
Cr#	5.0	0.0	0.0	3.6	0.0	1.1	3.4	0.0	0.0	0.0
Mg#	91.0	81.0	77.6	79.6	77.9	76.4	85.0	80.6	74.6	70.5

Table 1. Clinopyroxene major and minor element concentrations (wt. % oxide) from electron microprobe analyses at University of Houston and Texas A&M University.

Table 1. Clinopyroxene Major Elements (6 of 6)

Clinopyroxene Major Elements			
Sample Mineralogy	SE10-25-2 Augite	SE10-25-3 Augite	SE10-25-4 Augite
Na <sub>2</sub> O	0.3	0.2	0.3
MgO	13.5	14.0	13.7
SiO <sub>2</sub>	52.6	52.4	53.2
Al <sub>2</sub> O <sub>3</sub>	1.7	2.1	1.4
K <sub>2</sub> O	0.0	0.0	0.0
CaO	20.1	20.1	21.5
TiO <sub>2</sub>	0.5	0.4	0.3
Cr <sub>2</sub> O <sub>3</sub>	0.0	0.0	0.0
MnO	0.5	0.4	0.4
FeO	11.6	10.8	9.9
Fe <sub>2</sub> O <sub>3</sub>	0.0	0.4	0.0
Total	100.7	100.8	100.6
Wo	0.390	0.406	0.392
En	0.192	0.176	0.166
Fs	0.418	0.418	0.442
Cr#	0.0	0.0	0.0
Mg#	67.0	69.8	70.3

Table 1: Clinopyroxene major and minor element concentrations (wt. % oxide) from electron microprobe analyses at Texas A&M University and University of Houston.

Table 2. Spinel Major Elements (1 of 3)

Spinel Major Elements								
Sample	PR-41						LR-29	
	PR41-09	PR41-10	PR41-08	PR41-11	PR41-12	PR41-13	LR29-05	LR29-08
SiO2	0.16	0.16	0.16	0.07	0.07	0.06	0.05	0.02
TiO2	0.47	0.69	0.73	0.49	0.96	0.51	1.82	0.62
Al2O3	34.26	19.88	21.73	33.33	16.59	31.96	22.46	19.83
Cr2O3	20.76	37.20	33.40	22.04	37.87	24.50	25.02	37.15
Fe2O3	14.16	12.40	14.07	14.31	14.91	13.45	19.46	13.47
MgO	13.80	11.60	11.55	13.65	10.68	13.88	11.08	11.82
MnO	0.08	0.10	0.10	0.08	0.10	0.08	0.11	0.10
FeO	16.68	17.89	18.28	16.72	18.92	16.20	19.73	17.46
NiO	0.10	0.07	0.10	0.12	0.09	0.13	0.12	0.08
ZnO	0.11	0.08	0.09	0.15	0.05	0.10	0.10	0.07
Total	100.58	100.07	100.20	100.95	100.24	100.87	99.95	100.61
Cr#	28.899	55.65	50.77	30.74	60.50	33.97	42.77	55.70
Mg#	59.605	53.61	52.97	59.26	50.13	60.44	50.03	54.67

Table 2. Spinel major and minor element concentrations (wt. % oxide) from electron microprobe analyses at the University of Houston.

Table 2. Spinel Major Elements (2 of 3)

Spinel Major Elements							
Sample	LR-25						
	LR25-05	LR25-06	LR25-04	LR25-03	LR25-07	LR25-02	LR25-01
SiO2	0.03	0.05	0.04	0.04	0.04	0.08	0.08
TiO2	0.64	2.86	0.64	0.70	0.58	0.62	0.57
Al2O3	27.00	13.47	26.54	28.27	30.31	26.93	27.41
Cr2O3	30.60	25.87	30.77	28.09	28.08	30.34	30.40
Fe2O3	12.04	23.99	12.19	12.40	11.48	11.81	12.00
MgO	13.75	8.20	13.54	13.10	14.42	13.54	13.77
MnO	0.09	0.14	0.08	0.09	0.09	0.07	0.07
FeO	15.34	22.79	15.51	16.37	15.00	15.51	15.47
NiO	0.14	0.09	0.14	0.18	0.14	0.12	0.15
ZnO	0.05	0.16	0.15	0.18	0.01	0.13	0.08
Total	99.67	97.58	99.61	99.38	100.14	99.15	100.01
Cr#	43.20	56.29	43.76	40.02	38.35	43.042	42.66
Mg#	61.53	39.05	60.88	58.82	63.13	60.852	61.35

Table 2. Spinel major and minor element concentrations (wt. % oxide) from electron microprobe analyses at the University of Houston.

Table 2. Spinel Major Elements (3 of 3)

Spinel Major Elements						
Sample	SE10-21					
	SE10-21-05	SE10-21-03	SE10-21-08	SE10-21-09	SE10-21-10	SE10-21-11
SiO <sub>2</sub>	0.05	0.04	0.05	0.03	0.07	0.05
TiO <sub>2</sub>	0.08	0.17	0.02	0.13	0.16	0.10
Al <sub>2</sub> O <sub>3</sub>	46.68	22.45	46.59	13.78	11.64	24.00
Cr <sub>2</sub> O <sub>3</sub>	20.64	43.56	21.10	55.37	53.19	43.22
Fe <sub>2</sub> O <sub>3</sub>	1.32	4.43	1.61	2.48	4.12	2.74
MgO	16.30	11.99	16.98	12.29	7.34	12.20
MnO	0.06	0.11	0.06	0.11	0.16	0.11
FeO	13.89	16.91	13.03	15.03	22.10	16.72
NiO	0.24	0.11	0.21	0.08	0.04	0.11
ZnO	0.31	0.34	0.15	0.21	0.33	0.23
Total	99.54	100.08	99.78	99.50	99.14	99.47
Cr#	22.88	56.55	23.30	72.93	75.40	57.21
Mg#	67.64	55.82	69.90	59.31	37.16	55.46

Table 2. Spinel major and minor element concentrations (wt. % oxide) from electron microprobe analyses at the University of Houston.

Table 3. Clinopyroxene Trace Elements (1 of 2)

Clinopyroxene Trace Elements Chondrite Normalized								
Sample	BH-13-3	BH-13-6	BH-13-4	PR-41-1	PR-41-3	PR-41-4	SE10-25-6	SE10-25-4
Nb	0.07	0.12	0.04	0.14	0.06	0.14	0.12	0.12
La	0.62	2.67	1.67	4.79	0.94	2.46	8.26	5.05
Ce	1.20	5.06	2.92	9.35	1.91	5.04	16.79	10.60
Sr	4.33	2.78	2.51	3.70	4.63	3.98	3.29	2.35
Pr	2.12	9.24	4.99	15.30	3.39	8.75	29.73	19.17
Nd	3.29	14.23	7.60	22.35	5.67	13.73	47.59	30.19
Zr	1.14	3.65	2.40	5.94	2.52	3.14	7.39	5.74
Sm	5.01	21.99	10.66	31.63	9.14	19.44	70.69	47.23
Eu	6.27	14.37	9.02	19.24	10.58	18.58	50.58	26.89
Gd	5.88	26.11	12.32	33.46	10.96	22.77	88.83	58.39
Tb	6.15	26.60	12.46	31.75	11.01	21.76	92.37	63.15
Ti	5.47	3.94	3.86	4.54	9.81	5.02	5.15	3.57
Dy	5.68	27.65	13.11	32.10	10.68	21.13	94.15	67.94
Y	4.46	23.29	11.65	29.26	7.86	15.58	71.36	49.74
Ho	5.26	25.47	12.30	29.67	9.85	19.49	90.21	62.52
Er	4.96	25.33	11.96	27.47	10.33	19.66	90.68	66.46
Tm	4.55	23.43	10.99	25.00	8.00	16.88	79.74	59.83
Yb	4.19	22.80	10.91	25.27	8.14	16.83	82.29	60.28
Lu	3.39	21.35	9.85	24.17	6.34	15.12	80.83	56.69
Hf	3.05	7.37	4.81	9.95	7.28	7.07	15.15	12.77
V	6.25	3.97	5.32	4.23	7.79	4.76	0.48	4.25

Table 3. Table of chondrite-normalized trace elements measured at the University of Houston.

Table 3. Clinopyroxene Trace Elements (2 of 2)

Clinopyroxene Trace Elements Chondrite Normalized							
Sample	SE10-25-5	PR-42-01	PR-42-02	PR-42-03	EP-44-01	EP-44-02	EP-44-03
Nb	0.10	0.13	0.12	0.09	0.07	0.10	0.09
La	0.99	12.46	3.81	1.07	4.39	4.48	6.25
Ce	2.13	24.01	8.04	2.14	9.21	10.18	13.73
Sr	2.41	3.18	3.03	2.71	3.18	3.27	3.58
Pr	3.95	41.22	14.30	3.95	17.60	17.98	25.29
Nd	7.32	60.01	23.40	6.58	28.11	28.86	40.73
Zr	1.82	8.50	5.69	1.49	5.03	5.09	6.80
Sm	12.99	87.25	38.05	10.42	45.77	47.83	65.63
Eu	11.25	54.57	30.39	11.06	31.76	33.69	42.02
Gd	17.56	99.97	48.38	14.12	57.75	61.59	81.40
Tb	18.64	98.52	48.88	14.13	61.38	65.39	86.48
Ti	4.62	4.79	7.21	5.34	4.66	4.87	5.35
Dy	20.53	100.24	50.82	14.20	64.78	69.04	89.91
Y	15.41	74.15	36.66	10.26	49.97	50.26	64.18
Ho	19.62	94.02	45.68	13.07	61.21	63.66	83.12
Er	19.87	98.99	47.98	12.70	61.92	65.65	83.71
Tm	19.19	87.51	42.56	11.25	55.60	60.25	75.40
Yb	18.58	92.04	41.31	10.71	55.54	58.10	78.36
Lu	17.78	85.13	38.42	10.34	52.74	56.81	75.41
Hf	4.53	16.61	13.99	3.65	10.97	10.55	15.61
V	8.41	1.50	1.56	5.25	0.75	0.76	0.82

Table 3. Table of chondrite-normalized trace elements measured at the University of Houston.

## Results

### Petrography

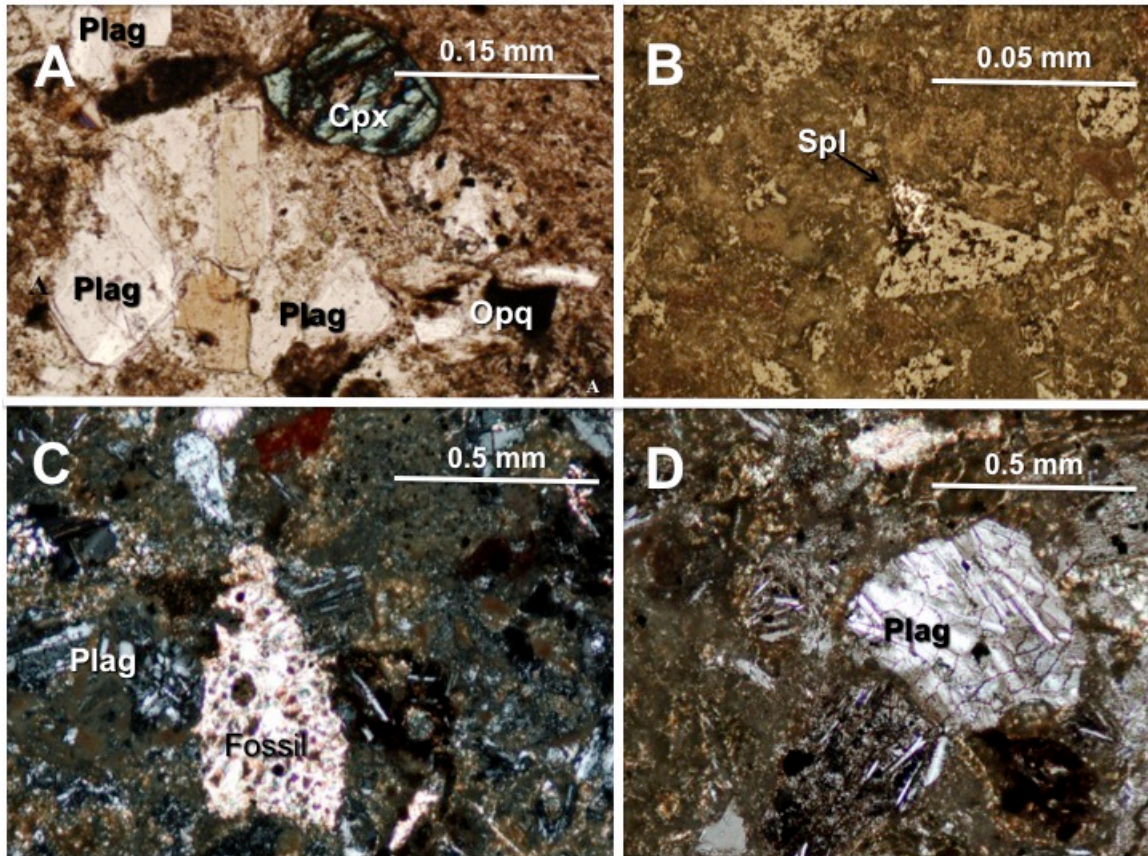


Figure 6. Photomicrographs of thin sections (TS) from Rivas turbidite samples shown clockwise from the top left corner. A) Larger clasts in TS include abundant plagioclase (Plag), opaques (Opq), and very minor clinopyroxene (Cpx). B) Reflected light (RL) image of a spinel (Sp) grain. C) Sample with fossil test and abundant plagioclase (Plag) grains in a micrite cement. D) Cross-polarized light (XPL) images of plagioclase laths and volcanic rock fragments, along with opaque grains and sparry calcite within a micrite cement.

Samples used in this study consist of sandstones and siltstones, limestones, and andesites. The sandstones of the Rivas and Descartes Formations can be broadly classified as volcanoclastic sandstones. Framework grains may be in either a micritic or clayey matrix (see Figure 6). The dominant clastic grain type is plagioclase, seen with

polysynthetic twinning and zoning. Plagioclase may be seen as euhedral laths to sub-rounded grains, and also make up lithic volcanic rock fragments. Plagioclase grains may be unaltered to moderately altered to sericite. Clastic samples contained less than one percent clinopyroxene and spinel. Clinopyroxene are sub sub-rounded to rounded. Biogenic grains consist of fossils (foraminifera, ostracods, gastropods, clams, bryozoans, etc.). Calcite spar is seen in limestones filling microfractures and as detrital grains (angular to sub-angular). Opaque minerals were common in all samples. Zircon is seen as a rare accessory phase.

### **Mineral identification**

EDS was used to identify the non-opaque heavy minerals from the Rivas and Descartes turbidites and volcanic samples. Identified grains are green clinopyroxene (primarily augite with minor diopside), spinel, and plagioclase was common. Very minor amounts of zircon and apatite were seen. Opaque minerals, such as ilmenite, were abundant.

### **Clinopyroxene**

#### *Major element geochemistry of clinopyroxene*

Clinopyroxene can have a wide range of compositions, depending on the chemistry of the parent magma type and tectonic setting (Le Bas 1962, Nisbet and Pearce 1977, Leterrier et al 1982); thus, geochemical analysis of the detrital clinopyroxene grains from the Descartes formation can constrain the magmatic affinities of the source rock that contributed to the turbidites (Cawood 1983). Clinopyroxene occurs primarily as augite ( $\text{Wo}_{43}\text{En}_{44.6}\text{Fs}_{12.3}$ ) with very minor diopside ( $\text{Wo}_{47.4}\text{En}_{47}\text{Fs}_{5.6}$ ). Clinopyroxene Cr# ranges from 0-10 with an average of 1.3, suggesting minimal melt interaction with fertile

peridotites. Plotting the clinopyroxene grains analyzed from the Rivas and Descartes Formations in the clinopyroxene end-member diagram (Figure 7), they fall in both the augite and diopside fields with the majority being augitic clinopyroxene.

LeBas (1962) defined a  $\text{SiO}_2\text{-Al}_2\text{O}_3$  covariation diagram based on pyroxene from igneous groundmass and determined boundaries among non-alkaline, alkaline, and peralkaline magma types. LeBas found that tholeiites, high-alumina, and calc-alkaline rocks fall in the sub-alkaline category. This is because as fractionation occurs (as  $\text{Fe}/\text{Ca}+\text{Mg}+\text{Fe}$  increase), the  $\text{Al}_2\text{O}_3/\text{SiO}_2$  ratio is small and will decrease with fractionation. It is understood that the  $\text{Al}_2\text{O}_3/\text{SiO}_2$  of the pyroxene varies with that of the host rock. Plotting the detrital and volcanic clinopyroxene from the Rivas and Descartes samples in this diagram shows that the grains fall into the sub-alkaline category (Figure 8). Additionally all the volcanic clinopyroxene samples show some compositional variation, even though they are from the same magma series.

Leterrier et al. (1982) discrimination diagrams were developed using chemical composition of calcic clinopyroxene from basalts and basic andesites. Using over 1,200 pyroxene analyses, a linear progressive discriminant analysis was done to understand how different elements partitioned in melt and how compositional variations could define different magma types. Only Ca, Ti, Al, and to a lesser extent Cr and Na were important cations in distinguishing among different magma types. The diagrams only distinguish between strongly contrasted magmas: orogenic basalts (island arc tholeiites, calc-alkali basalts, and island arc shochonitic lavas), non-orogenic tholeiites (basalts from rifts zones, back-arc basin tholeiites, oceanic island tholeiites), and alkali basalts (basanites,

etc.). While the diagrams were designed for volcanic samples, they still allow for differentiation of data from different tectonic settings.

Figures 9-11 define tectonic sources for clinopyroxene grains. Figure 9 is a plot elemental Ca+Na vs. Ti and defines fields for alkali basalts and other basalts (mid-ocean ridge (MOR), backarc (BAB), calc-alkaline, tholeiitic) and all the clinopyroxene samples are in the other basalts category. Figure 10 plots elemental Ca vs. Ti+Cr and further subdivides the other basalts category into non-orogenic (MOR, BAB) and orogenic (tholeiitic and calc-alkaline). The clinopyroxene fall within in the orogenic category; orogenic basalts are more depleted in Cr and Ti with respect to basalts from MORs, BABBs, and OIBs. Figure 11 plots total elemental Al against elemental Ti and differentiates the orogenic category into calc-alkaline and tholeiitic fields, showing a mix between tholeiitic and calc-alkaline tectonic origins for the clinopyroxene grains. As expected, the volcanic clinopyroxene grains from the andesitic boulder samples fall within the calc-alkaline field.

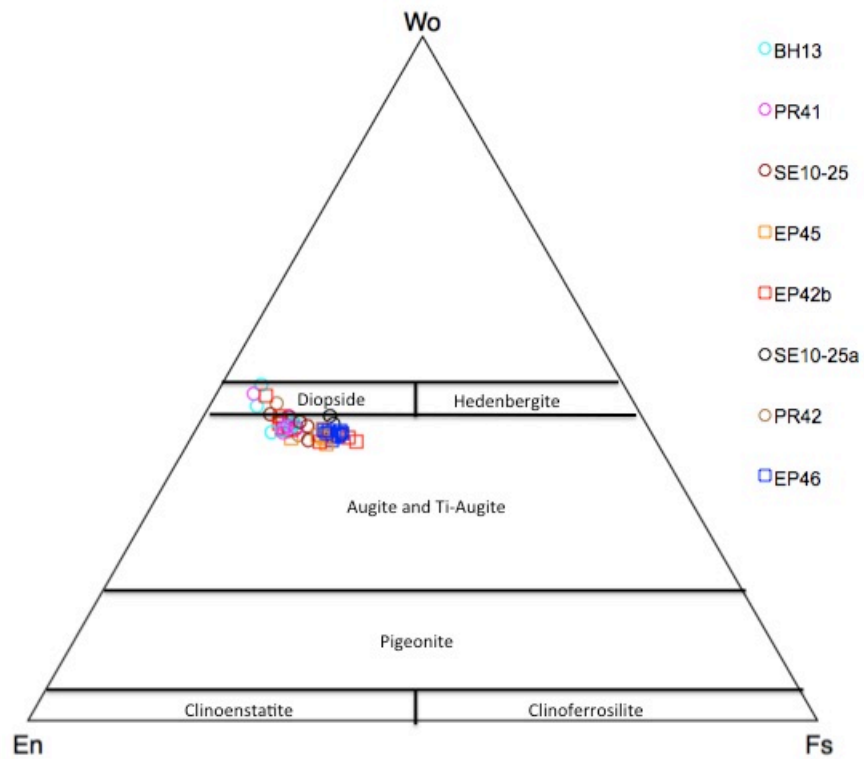


Figure 7.  $\text{Ca}_2\text{Si}_2\text{O}_6 - \text{Mg}_2\text{Si}_2\text{O}_6 - \text{Fe}_2\text{Si}_2\text{O}_6$  end-member diagram of clinopyroxene compositions. Detrital clinopyroxene grains from Rivas and Descartes Formation turbidites (open circles) and clinopyroxene grains from andesitic pebbly to boulder conglomerate (open squares) are plotted on the diagram. Detrital clinopyroxene grains are primarily augite with minor diopside.

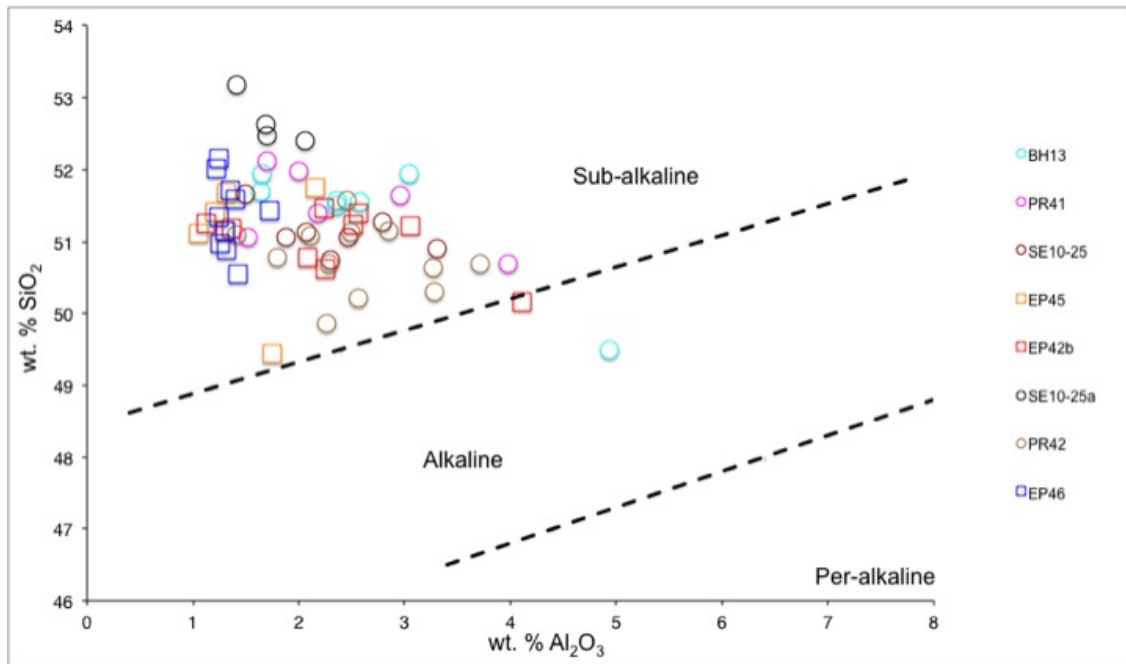


Figure 8: Al<sub>2</sub>O<sub>3</sub> vs SiO<sub>2</sub> co-variation diagram for Rivas and Descartes Formation detrital clinopyroxene grains. Divisions for compositional types are after Le Bas (1962). The detrital grains are open circles and the volcanic clinopyroxene grains from andesite boulders are open squares. The clinopyroxene derived from the turbidite and volcanic samples are classified sub-alkaline.

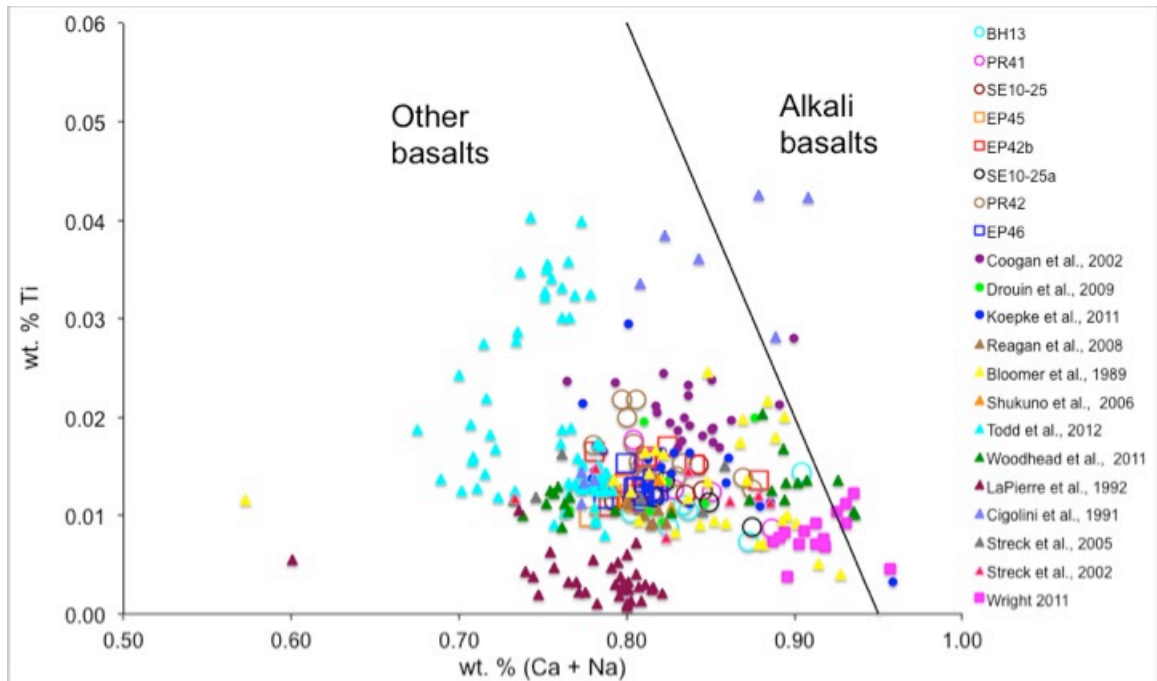


Figure 9. Discrimination diagram for clinopyroxene plotting wt. % (Ca+Na) vs wt. % Ti. This diagram distinguishes clinopyroxene from either alkali basalts (A) or other basalts (T) (fields after Leterrier et al., 1982). Comparison data are plotted on the graph: SEP ophiolite (closed pink square), mid-ocean gabbros (colored circles) and volcanic extrusives (colored triangles).

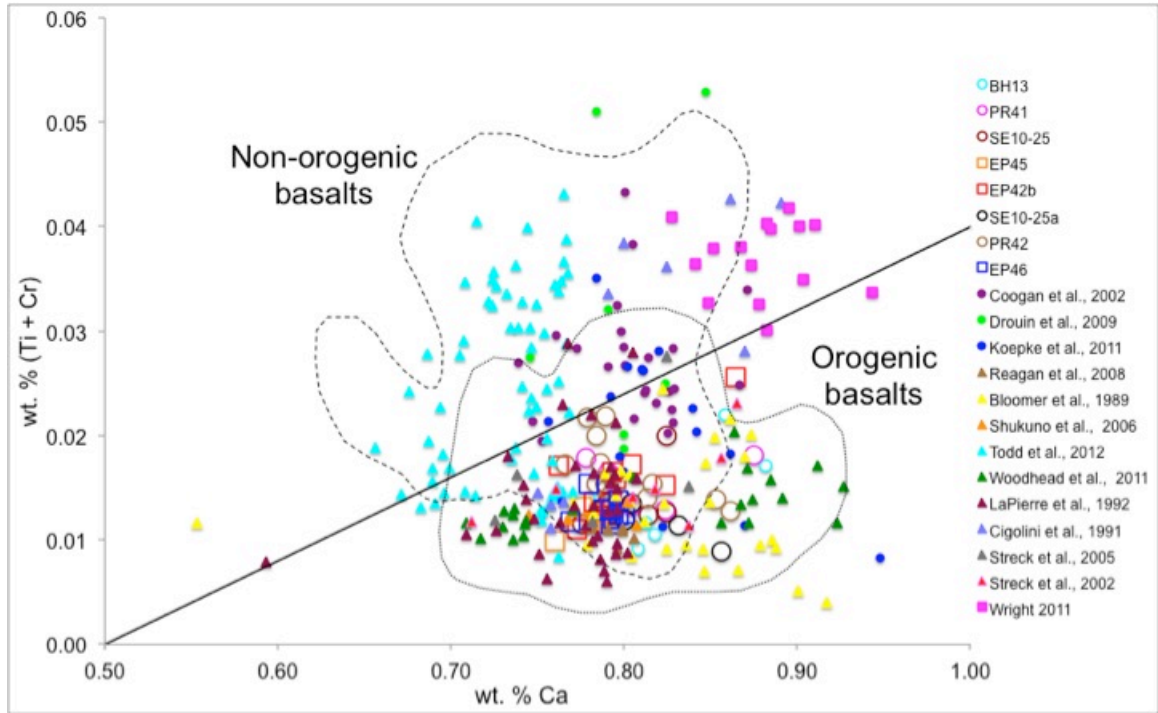


Figure 10. Plot of wt. % (Ca vs Ti) + wt. % Cr. This plot distinguishes clinopyroxene from orogenic basalts (O) (including island arc tholeiites, calc-alkali basalts from continental margins and island arc shoshonitic lavas) or non-orogenic tholeiites (D) (including transitional basalts from rift zones, abyssal tholeiites, back-arc basin tholeiites, oceanic islands tholeiites, continental tholeiites). Comparison data are plotted on the graph: SEP ophiolite (closed pink square), mid-ocean gabbros (colored circles) and volcanic extrusives (colored triangles).

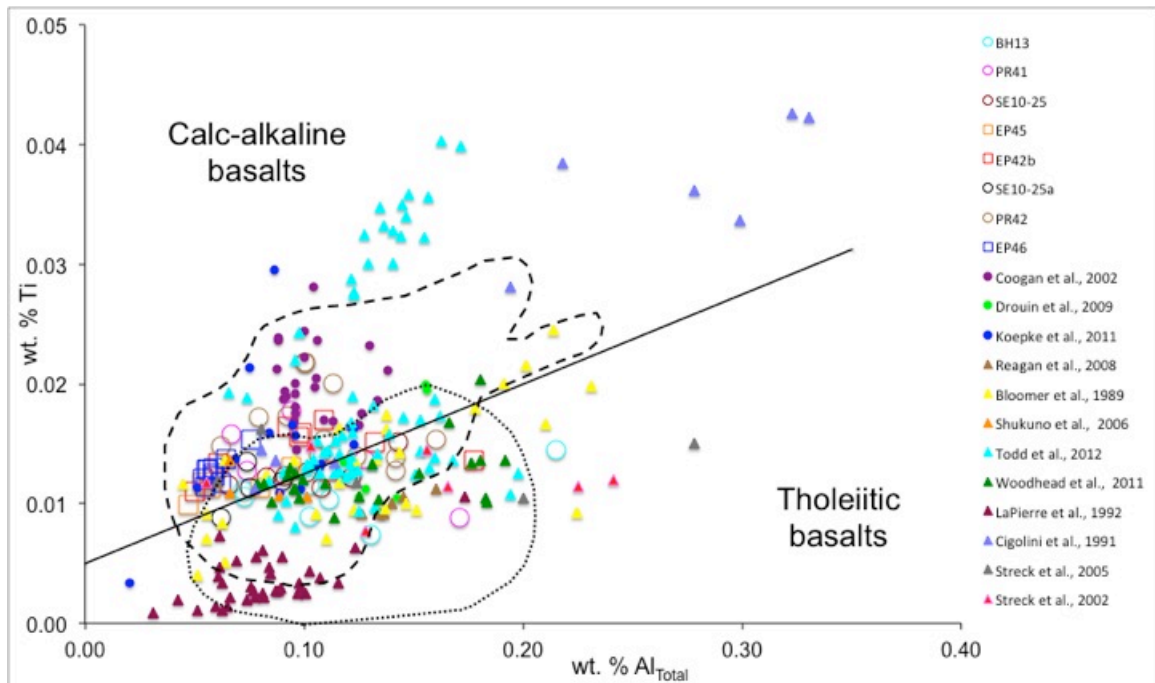


Figure 11. Plot of wt. %  $Al_{Total}$  vs wt. % Ti. This is a discrimination diagram for orogenic basalts and designates the clinopyroxene as either calc-alkali (C) or tholeiitic (I) in origin. Fields after Leterrier et al., 1982. Comparison data are plotted on the graph: mid-ocean gabbros (colored circles) and volcanic extrusives (colored triangles).

#### *Trace element geochemistry of clinopyroxene*

Figure 12 is a chondrite-normalized rare earth element (REE) diagram of the patterns for the detrital Rivas and Descartes clinopyroxene. Chondrite values for normalization were taken from McDonough and Sun (1985). All the clinopyroxene grains show slightly depleted, gently sloping light rare earth element (LREE) patterns, while they are slightly more enriched with high rare earth elements (HREE) that show a flat pattern. Although all samples follow the same general trend with slight LREE depletions, two separate groups are identified. Most of the analyzed clinopyroxene have a negative Eu anomaly as expected, but another group of four samples lack an Eu anomaly.

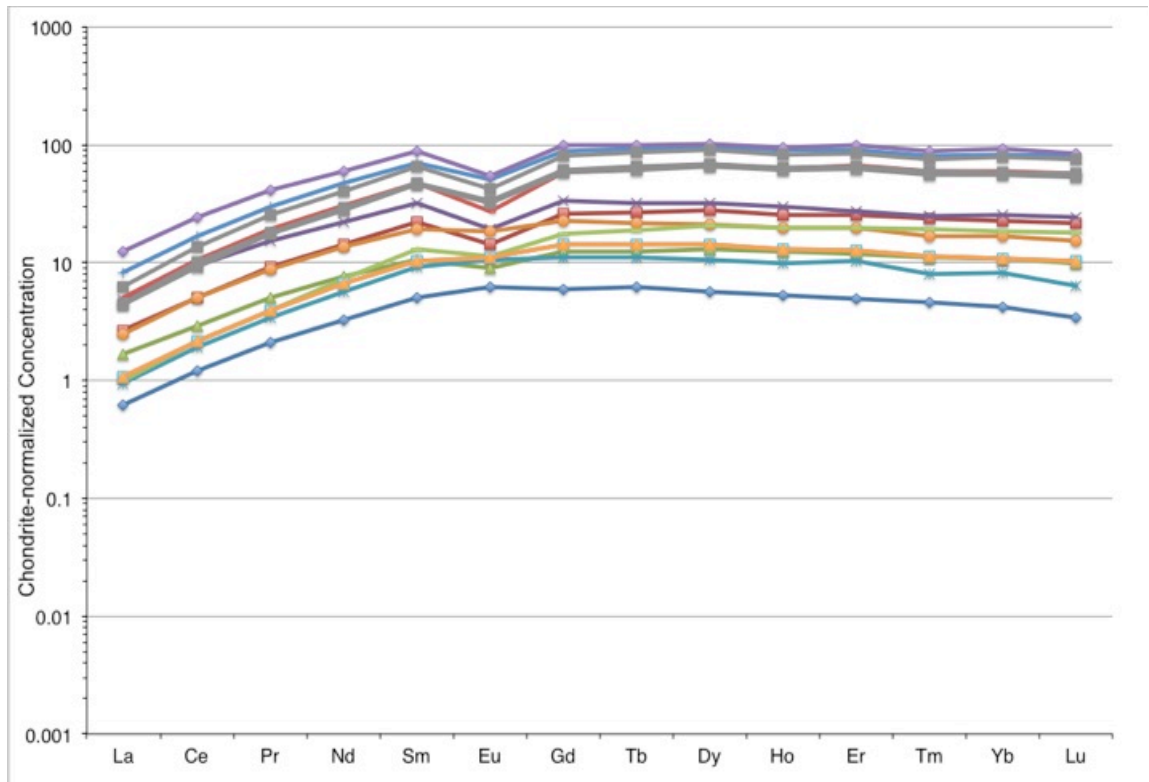


Figure 12. REE concentrations of Rivas and Descartes Formation detrital clinopyroxene (colored traces). Each colored line represents an individual detrital clinopyroxene from Rivas and Descartes Formation turbidite samples and is an average composition for that sample.

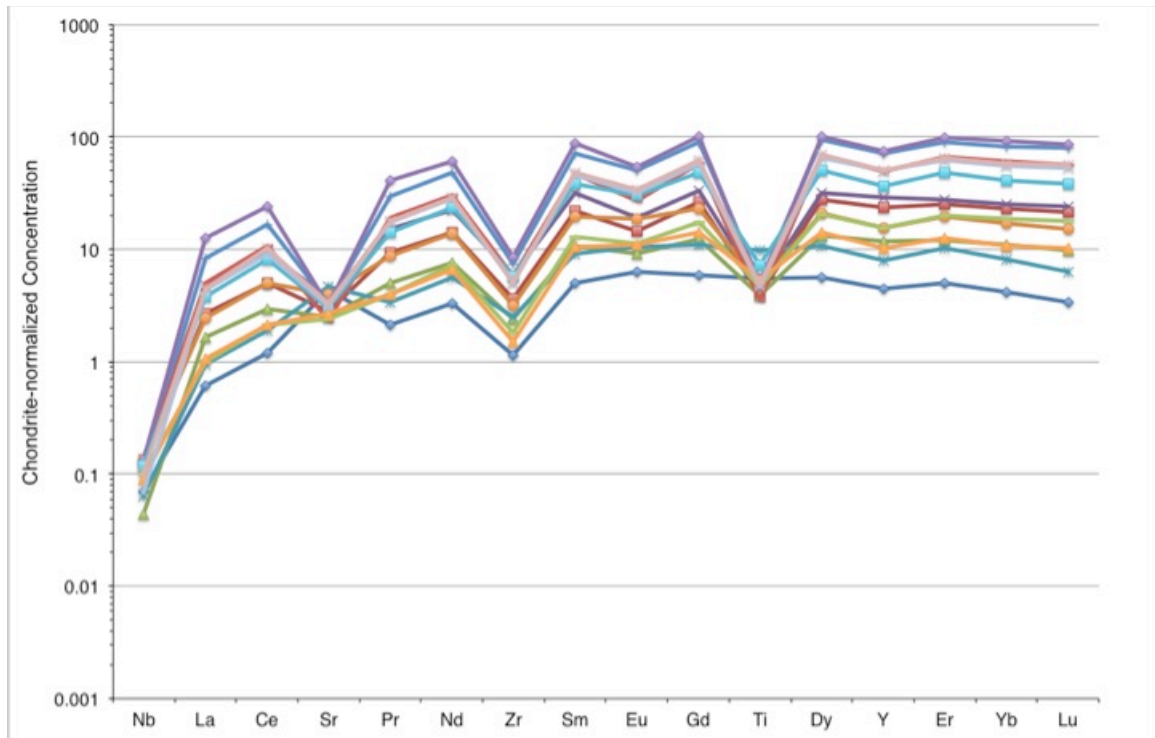


Figure 13. Extended trace element diagram for chondrite-normalized concentrations of detrital clinopyroxene grains from Rivas and Descartes Formation turbidites.

Figure 13 is an extended REE chondrite-normalized diagram for the Rivas and Descartes clinopyroxene grains. In addition to the negative Eu anomalies, the samples also have negative Ti anomalies, with the exception of two samples from group 2 with no Ti anomaly and higher Hf, along with three other samples. There are also 2 samples with flat spots at Y (BH13-4 and PR-41-1).

Differentiation of the Rivas and Descartes clinopyroxene grains may be seen in Figures 14-16 (additional diagrams in Appendix II Figures A-8 – A13). Figure 14 shows the clinopyroxene from Wright (2011) are much more depleted in LREE and have slightly enriched Tm. As the peridotite pyroxenes are from residues of partial melts, the LREEs are extracted, showing a steep LREE curve. The clinopyroxene from the turbidite

samples have a more gently dipping curve, implying a different tectonic source. Figure 15 shows a MOR gabbro clinopyroxene trace element pattern very similar pattern to the Descartes clinopyroxene, with slightly depleted LREE and flat HREE curves. Figure 16 compares the Santa Elena detrital clinopyroxene data to volcanic arc clinopyroxene data; the patterns are also similar with slightly depleted LREE and flat HREE patterns. The gabbroic patterns appear to cover the upper range of sample data, while the volcanic patterns cover the lower range of data. The major element data and trace element patterns of the detrital clinopyroxene show a clear difference from mantle clinopyroxene. The crossovers in the MOR and volcanic arc data suggest that there is not one single population of clinopyroxene in the Rivas and Descartes Formation deposits, but there are likely multiple sediment source inputs with different origins.

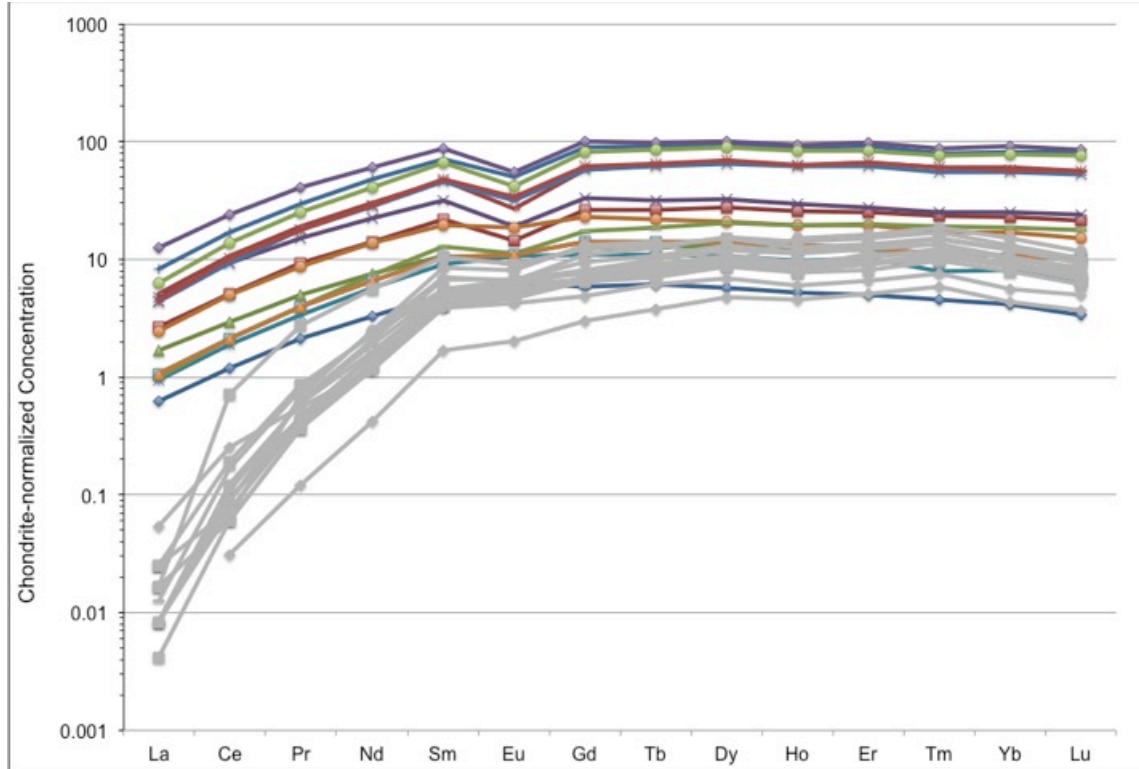


Figure 14. Chondrite-normalized concentrations for REE comparing trace element concentrations of mantle clinopyroxene from the Santa Elena ophiolite (Wright, 2011) to detrital clinopyroxene of Rivas and Descartes Formations.

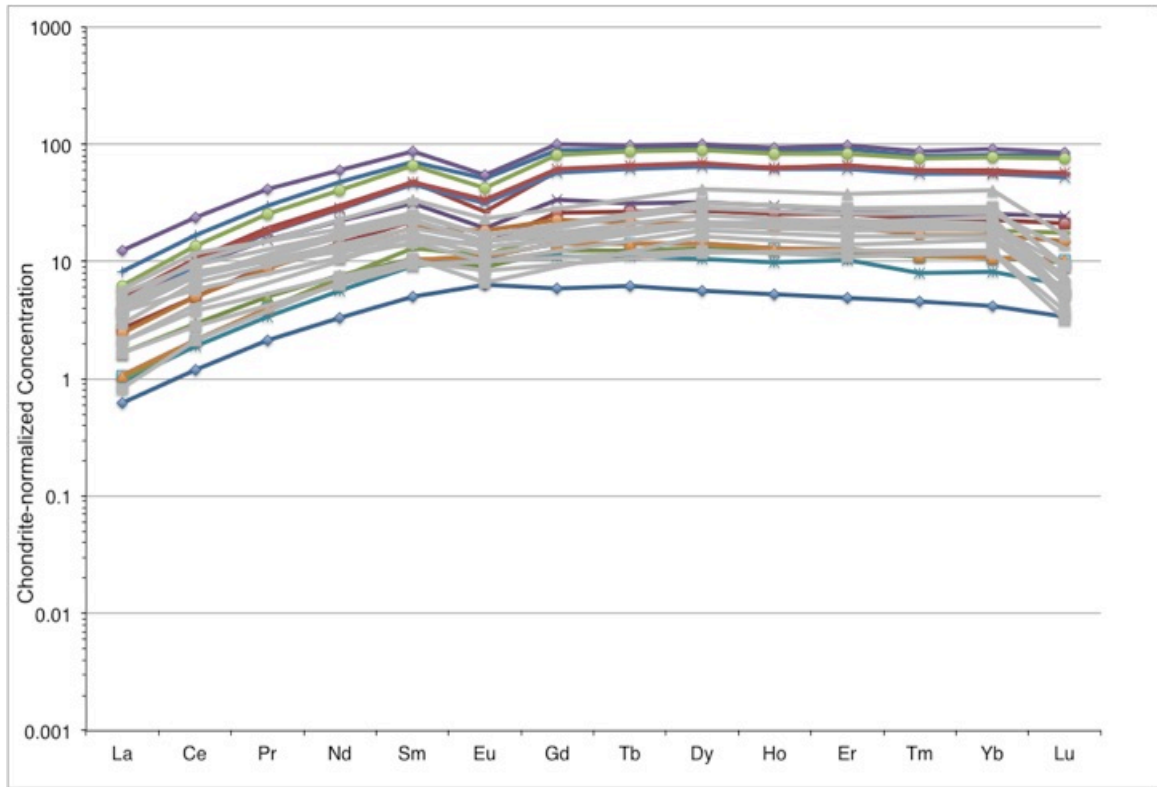


Figure 15. Chondrite-normalized REE diagram comparing trace element concentrations of clinopyroxene from mid-ocean ridge gabbros (Coogan et al., 2002) to detrital clinopyroxene of Rivas and Descartes Formations.

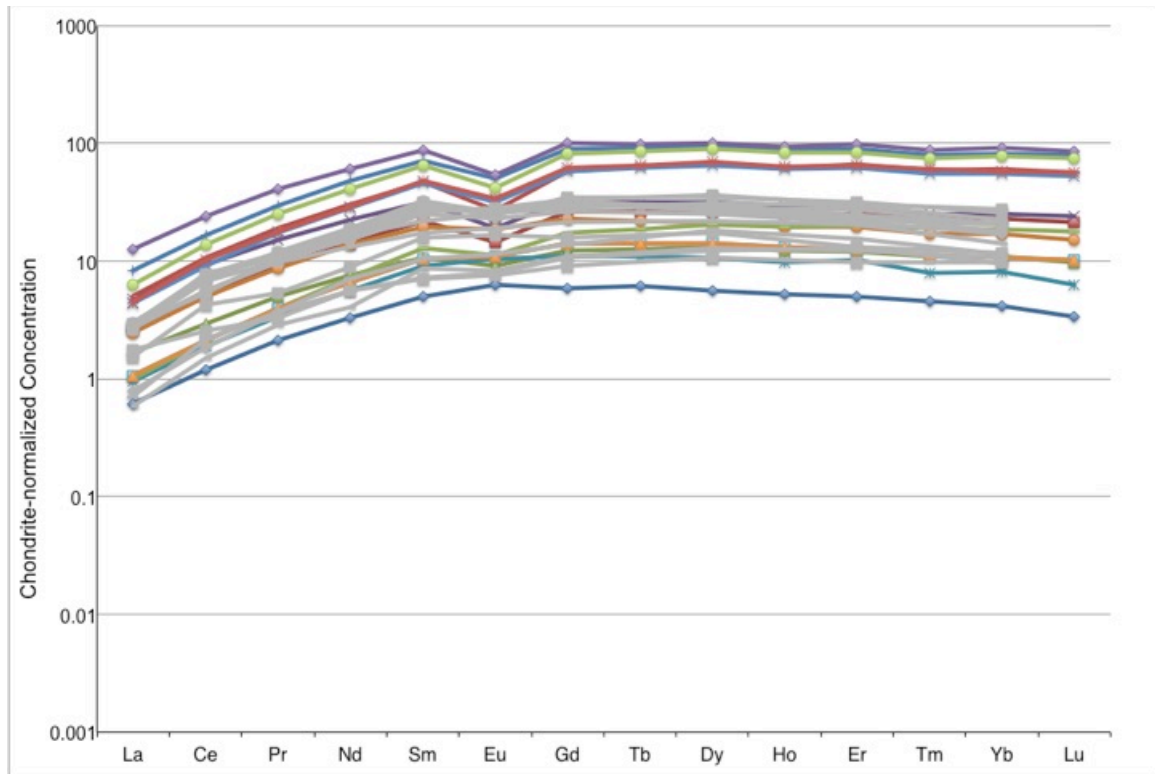


Figure 16. Chondrite-normalized REE diagram comparing trace element concentrations of clinopyroxene from volcanic arc basalts (Todd et al., 2012) to detrital clinopyroxene of Rivas and Descartes Formations.

Most subduction-related volcanic rocks have low abundances of the high field strength elements (HFSE) relative to the rare earth elements (REE), compared to MORB. HFSEs include Zr, Ti, Nb and Ta, which are incompatible and tend to concentrate in the melt. The heavy REE tend to be favored in solids over the liquids and are expected to be enriched the clinopyroxene. (Hawkesworth et al., 1994; Stalder et al., 1998). The detrital Rivas and Descartes clinopyroxene grains have negative Nb anomalies, indicating that they are HFSE depleted (Figure 13). The ratio of La/Sm is a measurement of the slope of the LREEs and indicates whether a magma is enriched or depleted (the negative slope in the trace element patterns here indicates the melt was more enriched in LREEs). The Nb/La ratio is a ratio of the HFSE to the REEs. Figure 17 shows a plot of Nb/La against

La/Sm. Subduction zone volcanics are expected to have a low Nb/La ratio. The detrital clinopyroxene data (including one sample from an andesite cobble – EP 46) are compared to volcanic clinopyroxene from the Fiji-Tonga-Kermadec arc, gabbroic pyroxene from the Parece Vela backarc basin, and gabbroic mid-Atlantic ridge clinopyroxene. The andesite clinopyroxene sample has the lowest ratio of HFSEs to REEs (0.02), while the MOR clinopyroxene have higher ratios (0.2-0.5). The data from the Fiji volcanic arc have a wider field of Nb/La ratio (0.02-0.2) that begin to overlap the MOR and BAB samples. The detrital clinopyroxene grains cluster nearer the andesite samples and nearer the more HFSE-depleted end of the diagram.

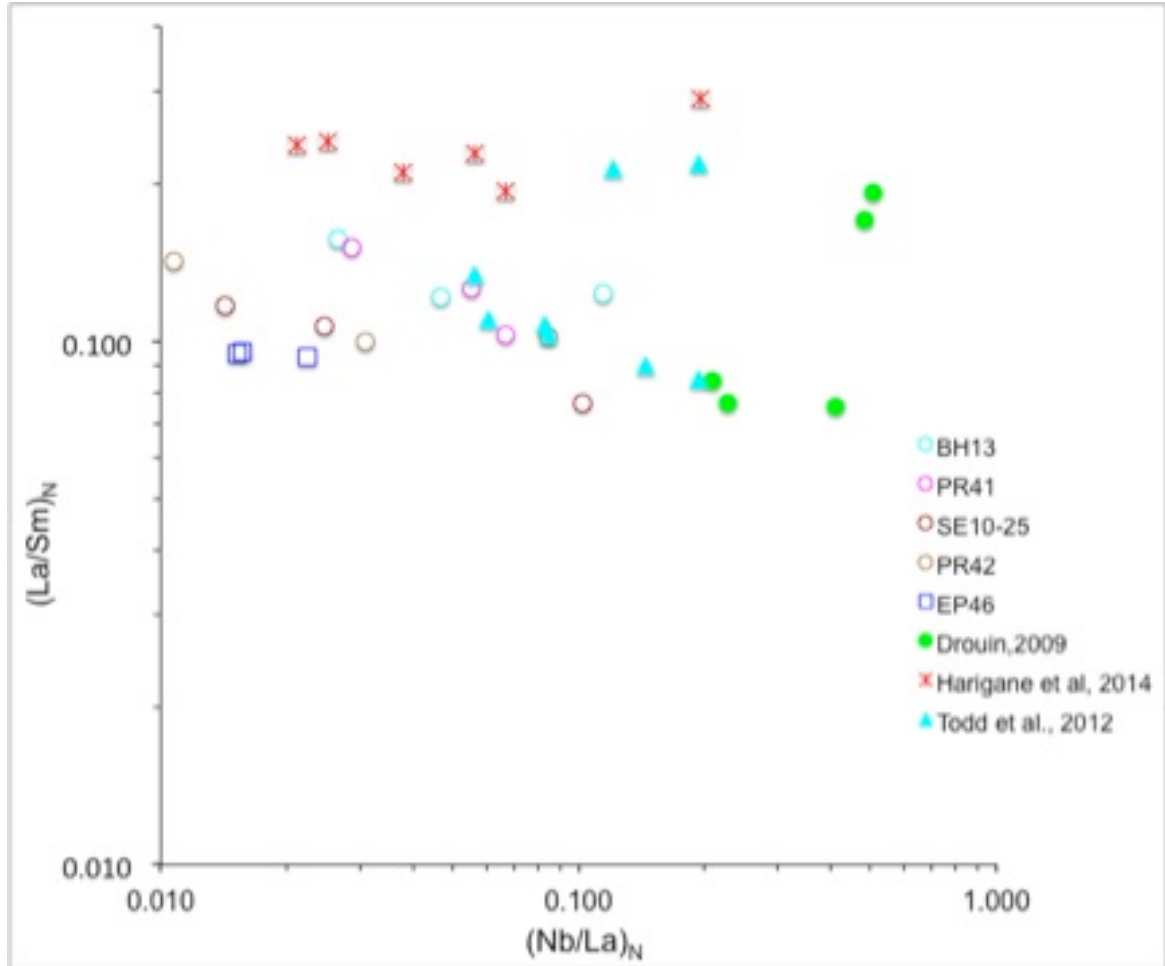


Figure 17. Plot of chondrite-normalized trace element ratios of Nb/La vs. La/Sm. Shown are Santa Elena detrital clinopyroxene grains (open shapes), andesitic boulder sample (EP 46 – open squares), volcanic arc (Fijian arc) clinopyroxene (closed triangles), backarc (BAB) clinopyroxene (stars), and mid-ocean ridge (MOR) clinopyroxene (closed circles).

## **Spinel**

Chromian spinel is an accessory mineral phase that is seen across the spectrum of peridotites and basalts, and it is sensitive to bulk composition and petrogenesis of the host rock. During fractional crystallization, Cr and Mg are strongly partitioned in to the solid, while Al moves into the melt. While spinel undergoes large compositional changes during crystallization, melting, and re-equilibration, other silicate phases may only see modest compositional changes (Dick and Bullen, 1984); thus, Dick and Bullen (1984) call chromian spinel “petrologic litmus paper” because it is so sensitive to parent rock crystallization.

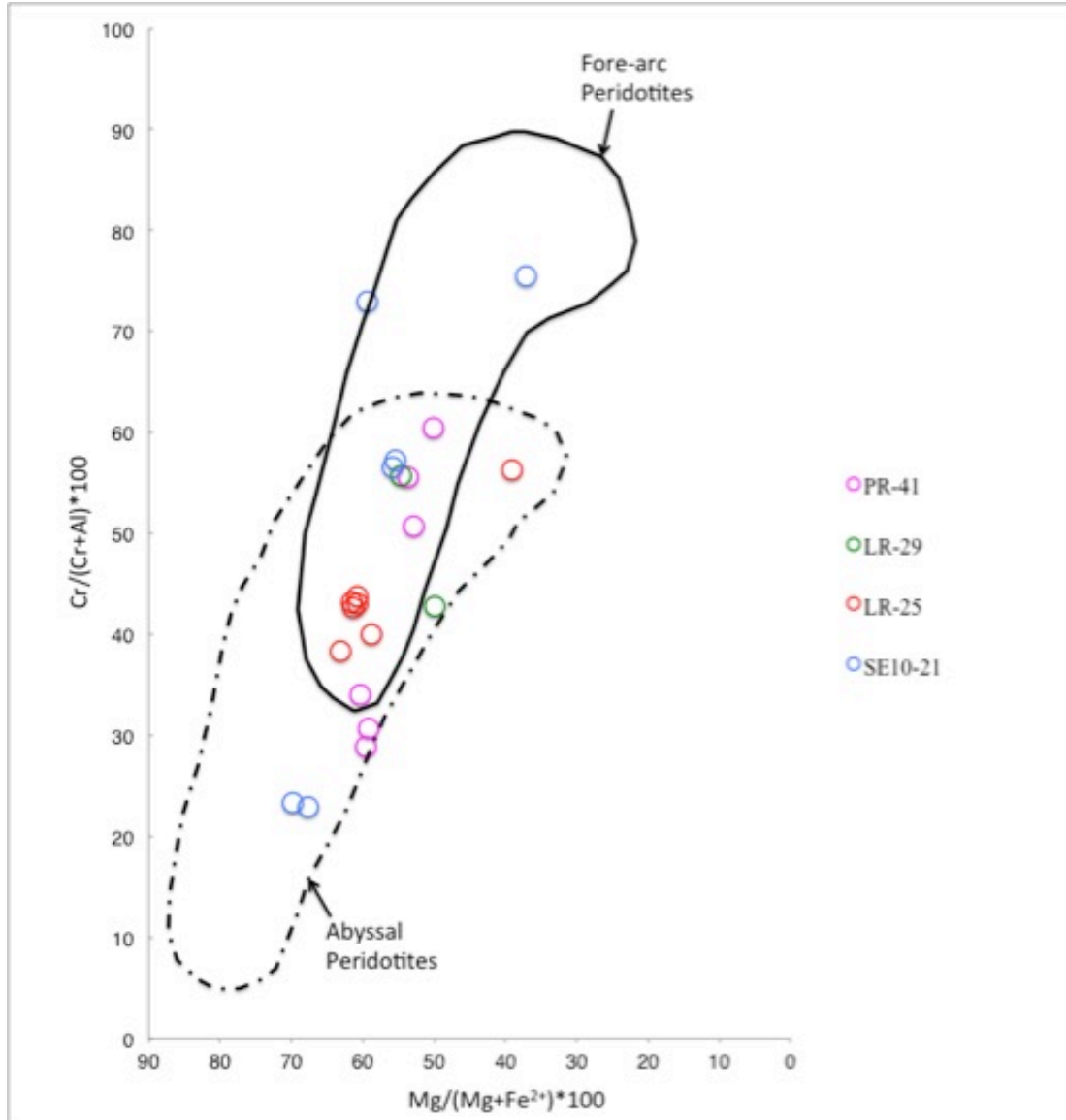


Figure 18. Plot of spinel Mg# ( $Mg/(Mg+Fe^{2+})$ ) against spinel Cr# ( $Cr/(Cr+Al)$ ). The detrital spinel grains fall in both the abyssal and forearc fields. Partial melting of peridotites results in an increase in spinel Cr# and a decrease in spinel Mg#, resulting in a negative melting trend correlation. Fertile to moderately depleted abyssal peridotites fall on the lower end of this trend with low Cr#'s and high Mg#'s, while more depleted fore-arc peridotites fall on the upper end of the trend (fields after Dick and Bullen, 1984). An additional figure compares the turbidite detrital spinel compositions to spinel compositions from different tectonic settings globally (see also Appendix III Figures A-15).

Figure 18 shows the spinel grains from the Descartes formation turbidites plotted as Mg# ( $\text{Mg} \cdot 100 / \text{Mg} + \text{Fe}^{2+}$ ) against Cr# ( $\text{Cr} \cdot 100 / \text{Cr} + \text{Al}$ ). All the grains demonstrate a positive correlation with spinel Mg#. Cr#s range from the low 20s to the upper 70s, while Mg#s range from the upper 30s to the upper 60s. The spinel grains plot in both abyssal and fore-arc peridotite fields, as defined by Dick and Bullen (1984). The PR and LR samples fall in the overlapping field between both end-members, while the SE samples range from end member compositions and in the overlapping field. Spinel in the abyssal range are more enriched in aluminum and moderately fertile with minimal partial melting of a depleted MORB mantle (Workman and Hart, 2005), while the spinel in the fore-arc range are more heavily depleted in aluminum and are more comparable to mantle spinel from a convergent plate margin (Dick and Bullen, 1984; Parkinson and Pearce, 1998).

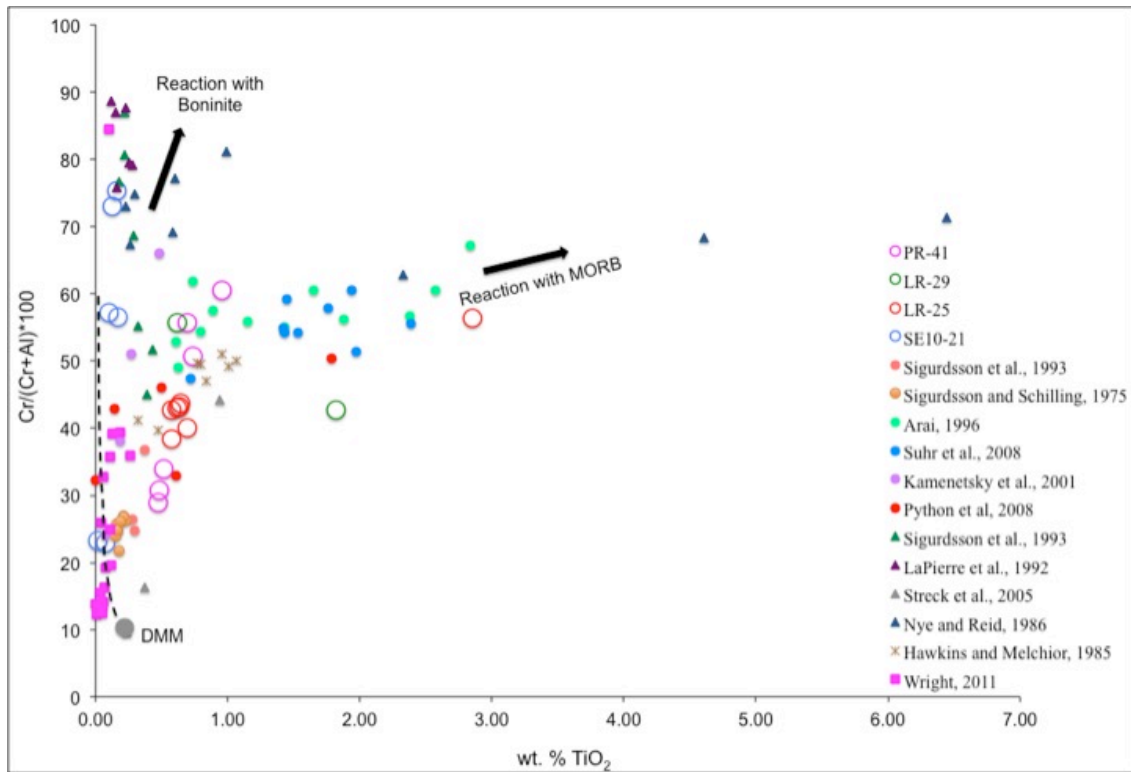


Figure 19. Plot of wt % TiO<sub>2</sub> in spinel against Cr# [Cr/(Cr+Al)] in spinel. Partial melting of the mantle results in an increase in Cr# with a simultaneous decrease in TiO<sub>2</sub>. The DMM in the figure (Depleted MORB Mantle) of Workman and Hart (2005) and shows the most undepleted end of the mantle trend described by low Cr#'s and relatively high TiO<sub>2</sub>. As partial melting occurs in the spinel peridotite field, melting follows the dashed line trend. The figure compares the turbidite detrital spinel compositions to spinel compositions from different tectonic settings globally (see Appendix). The two arrows show the effects of metasomatism of peridotites with more titanium rich melts, either MORB or boninite.

In Figure 19 the Rivas and Descartes detrital spinel represent samples from four locations and have variable compositions. Samples from PR-41 have low wt% Ti (<1 %) with Cr# varying from high 20s to low 60s. The samples from LR-29 have <1 wt % Ti and Cr#s more constrained from high 30s to mid 40s, and one outlier with ~3 wt% Ti and Cr# in mid 50s. The LR-29 sample has 1 spinel that plots <1 wt% Ti and Cr# mid 50s and another with ~2 wt% Ti and Cr# in the low 40s. Both the LR-25 and LR-29 samples

have higher weight percent  $\text{TiO}_2$ , possibly indicative of melt-rock interaction with MORB-type melts. SE10-25 shows a distribution of spinel compositions with  $< 1$  wt% Ti and Cr# varying from 20-75. In this group, the low Cr# samples plot along the anhydrous, fractional peridotite melting trend of Hellebrand et al., (2001) and have a comparatively moderately fertile signature. In contrast, the remaining spinels in the group become more depleted in aluminum and move toward the part of the diagram that represents metasomatism with boninite-type rocks. This is indicative of mantle spinel from plate-convergent settings (Dick and Bullen, 1984; Parkinson and Pearce, 1998) and typical of supra-subduction zones (Iishi et al, 1992) where hydrous re-melting of refractory mantle and melt-rock reaction with refractory melts has occurred.

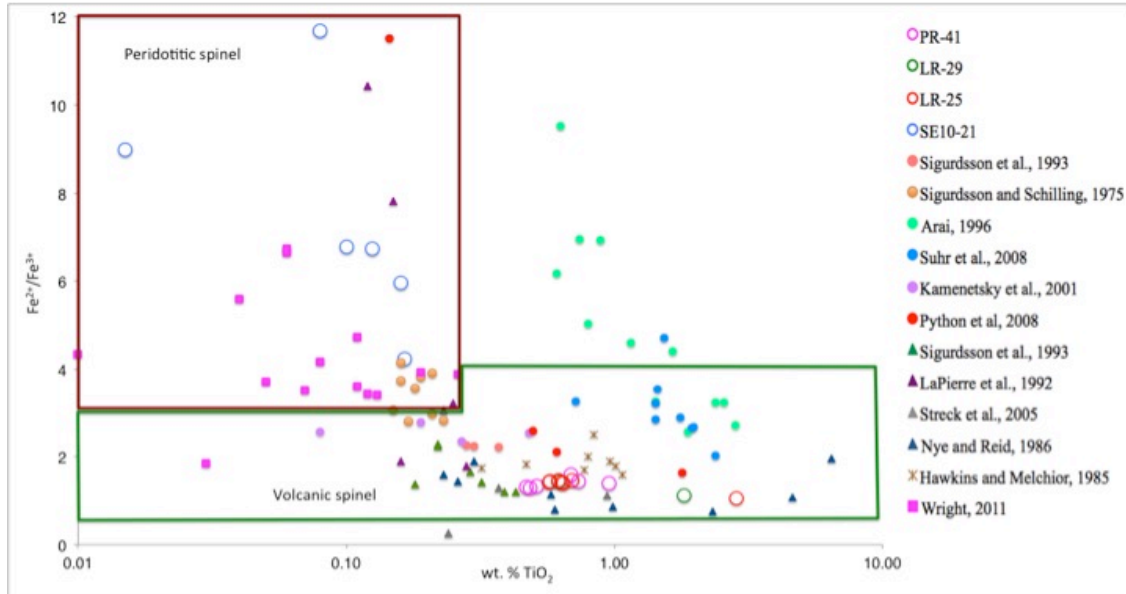


Figure 20. Spinel wt. % TiO<sub>2</sub> plotted against Fe<sup>2+</sup>/Fe<sup>3+</sup>. Diagram shows compositional fields for peridotitic spinel (TiO<sub>2</sub> < 0.2 wt. %, Fe<sup>2+</sup>/Fe<sup>3+</sup> > 3) and volcanic spinel (Fe<sup>2+</sup>/Fe<sup>3+</sup> < 4) (fields after Kamenetsky et al., 2001). Over 95% of spinel analyses from mantle peridotites have <0.2 wt% TiO<sub>2</sub>. The figure compares the turbidite detrital spinel compositions to spinel compositions from different tectonic settings globally (see Appendix).

Kamenetsky et al. (2000) studied detrital spinel from turbiditic sandstones in NE Italy and NW Slovenia and recognized two compositional groups, one from mantle peridotites (ophiolites) and another from basaltic volcanics. The peridotitic spinel are defined by high Fe<sup>2+</sup>/Fe<sup>3+</sup> and <0.2 wt% TiO<sub>2</sub>. The volcanic spinel have higher wt% TiO<sub>2</sub>, higher Al<sub>2</sub>O<sub>3</sub>, and include a broad category of MORB-type rocks, backarc basin basalts, subduction-related magmas, and tholeiites from continental rifting. Figure 20 shows the defined regions of peridotitic and volcanic spinel. Here the SE10-21 samples plot within the peridotitic spinel field (these grains have varying Cr#s from the 20s to 70s, moderately depleted to more depleted Al). The samples from PR-41 and LR-25 and

LR-29 samples plot within the volcanic spinel area. Some of the PR samples which have high Mg#s may be indicative of fast-cooled volcanic rocks and chromitites (Irvine, 1967).

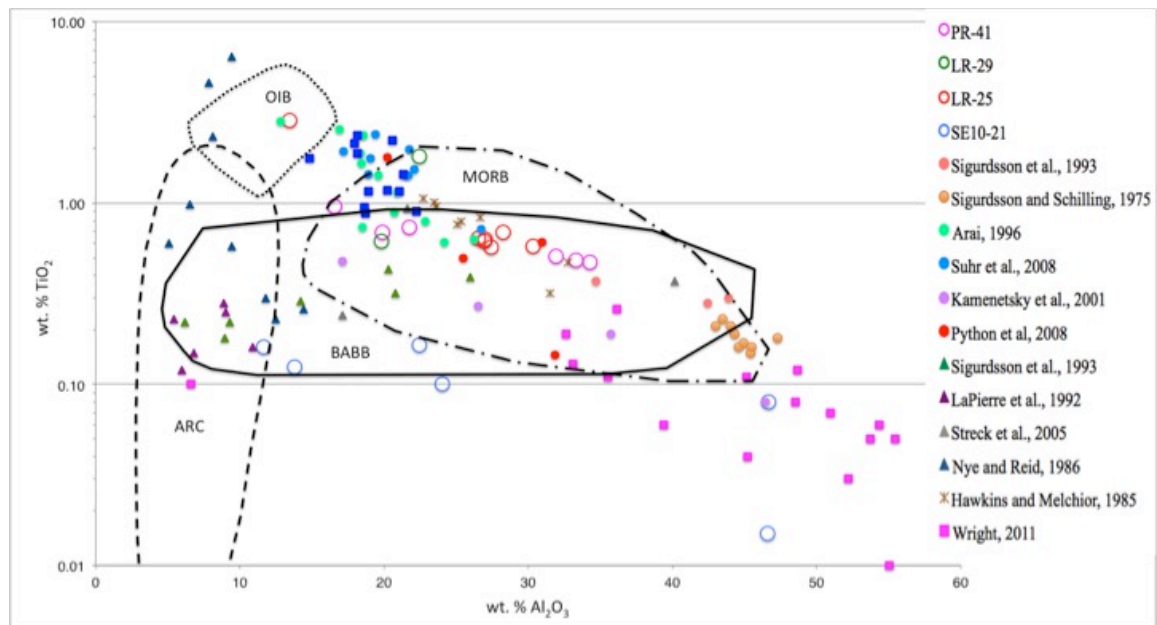


Figure 21.  $\text{Al}_2\text{O}_3$  wt. % vs  $\text{TiO}_2$  wt. % compositional relationships of “volcanic” spinel ( $\text{TiO}_2 > 0.2$  wt. %) (fields after Kamenetsky et al., 2001). Fields discriminate among spinel from mid-ocean ridges (MORB), backarc basins (BABB), ocean islands (OIB), and island arc magmas (ARC). The figure compares the turbidite detrital spinel compositions to spinel compositions from different tectonic settings globally (see Appendix).

To further examine tectonic provenance of detrital spinel from sedimentary rocks, Lenaz et al. (2000) plotted  $\text{Al}_2\text{O}_3$  against  $\text{TiO}_2$  abundances and calibrated against global settings to create four ranges for tectonic settings: volcanic island arcs, mid-ocean ridges, backarc basins, and ocean islands. High  $\text{Al}_2\text{O}_3$  (greater than 25%) is indicative of rocks from MORB or MORB-like backarc rocks, while spinel with  $\text{Al}_2\text{O}_3$  from 15-25% and  $\text{TiO}_2 < 1$  wt% represent subduction-related backarc basalts or continental tholeiites. Low  $\text{Al}_2\text{O}_3$  and high  $\text{TiO}_2$  up to 3 wt % point to possible intra-plate volcanism like ocean island basalts. The spinel from island arcs have low ( $< 0.2$  wt%)  $\text{TiO}_2$ . In Figure 21, the

SE10-21 samples plot within the backarc and arc regions, while the PR-41, LR-25 and LR-29 samples plot primarily within the mid-ocean ridge and backarc regions.

In summary, all the detrital and volcanic clinopyroxene samples are sub-alkaline. Compositions range from diopside to augites. The clinopyroxene are not all from the same volcanic series, but they are not from the mantle residues. There are both tholeiitic and calc-alkaline clinopyroxene compositions corresponding to upper crustal gabbroic clinopyroxene or volcanic clinopyroxene. The detrital spinel grains are not all from mantle residues and are not from the Santa Elena ophiolite. The spinel show influence from volcanic arc and mid-ocean ridge tectonic settings. The minerals are not from a single source, but are from different rock types and tectonic settings.

## **Discussion**

### **Tectonic setting and petrogenesis**

Analysis of the chemical compositions of clinopyroxene and spinel from the Rivas and Descartes Formations indicate provenance and tectonic origins of the turbidite detrital grains. The rock types that are seen in Costa Rica and Panama represent possible source inputs, including ultramafic ophiolite bodies (such as the Santa Elena ophiolite complex), oceanic remnants of the CLIP (tholeiitic basalts from the Nicoya Complex), mafic gabbros, and volcanic arc andesites. Figure 22 is a general cross-sectional view from west to east of what the paleogeography might have looked like during the Paleocene to Eocene during the time the forearc Sandino Basin was developing. The bounding features are the Middle America Trench (MAT) in the west and the andesitic arc in the east. The forearc basin may have been underlain with late Cretaceous tholeiitic arc and oceanic Nicoya complex, which may have shed sediments into the basin while it formed. The accreted ophiolite may have acted as a backstop on the western edge of the basin, trapping the sedimentary fill and also contributing sediments during uplift of the outer arc. The developing andesitic arc to the east was also a possible contributor of detritus. As any or all of these terranes emerged or were shallowly uplifted, ephemeral carbonates formed and contributed hemipelagic carbonate sediments into the system. It is possible to compare the geochemical data from the detrital spinel and clinopyroxene of the Rivas and Descartes Formations to those of different rock types seen in Costa Rica to determine the tectonic origins and provenance of the sedimentary deposits in the Sandino Basin.

## **Ophiolite sources**

Typically, ophiolite complexes do not have components from only one tectonic setting; they may have a range of compositions from fertile, un-metasomatized to highly depleted mantle (Choi et al., 2008, Aldanmaz et al., 2009). Portions of ophiolites falling within the peridotite abyssal field of Dick and Bullen (1984) are interpreted as preserved mid-ocean ridge or back-arc basin mantle (Choi et al., 2008), and this how the Santa Elena peridotites are categorized. Peridotites from the Santa Elena ophiolite evolved due to partial melting of mantle rocks that were anhydrous to slightly hydrous, with fractional partial melting up to 25% (Dick et al, 1984; McKenzie and Bickle, 1988). The melts are thought to initiate with a depleted upper mantle source (DMM) (Workman and Hart, 2005), which would produce low-degree melts high in incompatible element concentrations (e.g., Ti, Ba, La, Ce), so that peridotites formed beneath mid-ocean ridges are expected to have moderate to no depletion in incompatible elements. This melt would then create the lherzolites and clinopyroxene-bearing harzburgites found in the massif. To determine whether there is input from the Santa Elena ophiolite within the turbidite deposits, the geochemical analyses of clinopyroxene and spinel from Wright (2011) are compared to the detrital clinopyroxene and spinel data from the Rivas and Descartes Formation turbidites.

The Santa Elena ophiolite data from Wright (2011) indicate that the clinopyroxene Mg#s range from 91 to 93 and have Cr #s from 8 to 19. The detrital clinopyroxene from Santa Elena ophiolite and Descartes peninsula are compositionally different; the Mg#s range from 63 to 91 with an average of 78, while Cr #s are much lower from 0 to 10 with an average of 1.3. The geochemical data from the clinopyroxene

detrital grains are compared to the SEP ophiolite clinopyroxene in the pyroxene composition end-member diagram (Figure A-4). The Santa Elena ophiolite pyroxene plot in a tight cluster within the diopside field. While some Rivas and Descartes clinopyroxene are diopside, the majority of the SEP detrital clinopyroxene grains plot as augite. The detrital grains that are diopside plot in a distinctly different position than the diopside from the SEP ophiolite being more calcium-rich.

Discrimination diagrams (LeBas, 1962; Leterrier et al., 1982) allow for further elucidation of the sedimentary source of the detrital grains. In the LeBas covariation diagram (Figure A-14), all the detrital and SEP ophiolite clinopyroxene data are within the sub-alkaline field (low silica and high alumina), which is defined as input from a tholeiite, ocean floor basalt, or a volcanic arc basalt. As the sub-alkaline category is quite broad, the Leterrier diagrams continue to break down the tectonic origins of the pyroxene. In the first plot from Leterrier (Figure 9), both the detrital and ophiolite clinopyroxene fall in the other basalts field (i.e., MORB, BABB, tholeiitic, calc-alkaline). The next diagram (Figure 10) breaks the category into non-orogenic (MORB, BABB) and orogenic (tholeiitic, calc-alkaline). Here again there is a separation of the data; the SEP clinopyroxene fall in the non-orogenic field, while the Rivas and Descartes clinopyroxene grains are within the orogenic field.

Clinopyroxene from peridotite may indicate extent of partial melting based on their trace element concentrations (Johnson, 1990; Hellebrand et al., 2001). The concentration of HREEs relative to LREEs can be used to infer how much partial melting has occurred, because LREEs are more incompatible in melts than HREEs. During normal, anhydrous melting of mantle rocks, there will be a greater decrease of LREE

concentrations than HREE concentrations. This will result in REE patterns with a more steeply dipping LREE end of the curve than the MREE and HREE end of the curve. For mantle clinopyroxene, a steeply dipping LREE curve indicates low to moderate degrees of partial melting and that they have been unaffected by metasomatism after initial melting. Figure 14 is a chondrite-normalized trace element diagram comparing the SEP ophiolite clinopyroxene data to the Rivas and Descartes detrital grains. Because the peridotite spinels are from residues of partial melts, they are extremely depleted in LREEs, creating a steeply dipping LREE curve, relative to the detrital grains, which have a more gentle LREE curve. In addition, the extended trace element diagram (A-8) indicates that the ophiolite mantle clinopyroxene are enriched in Nb, whereas the detrital clinopyroxene are depleted. The more gently dipping LREE curve from the detrital turbidite clinopyroxene would indicate much more melt-rock interaction for if it was mantle clinopyroxene, but more likely they have crystallized from a melt, so they are getting more LREE input. As the data suggest, the detrital clinopyroxene from the Rivas and Descartes turbidites is not from an ophiolitic source.

Spinel Cr# (molar Cr/(Cr+Al)) is acknowledged as an indicator of extent of partial melting (Dick and Bullen 1984) and melt-rock reaction (Kelemen, 1990). Chromium is very compatible within the mantle, while aluminum is highly incompatible; thus, as degrees of partial melting increase, there will be a decrease of aluminum concentration. This is reflected as an increase in Cr# with increased partial melting (Dick and Bullen, 1984). The range of Cr#s for mantle peridotites starts at 10 for the most fertile and goes up to 90 for the most highly depleted peridotite. Wright (2011) determined that Santa Elena ophiolite complex spinel has Cr#s ranging from 12 to 39, suggesting only modest

depletion and Mg #s ranging from 58 to 80. These grains plot within the abyssal group of Dick and Bullen (1984) (Figure 18). The spinel from the turbidites have Cr#s ranging from 22 to 59 and Mg#s of 50 to 70 and plot within both the abyssal and forearc fields.

Figure 19 shows the changing chemical signature of peridotitic spinel as a relationship between Cr# and wt% Ti. In normal anhydrous partial melting of the mantle, there is an increase in Cr# with a decrease in wt % TiO<sub>2</sub>. In this figure, the most undepleted end of the mantle trend is represented by depleted MORB mantle (DMM) of Workman and Hart (2005). With normal, anhydrous melting of DMM, the melt trend follows the dashed line and there is no interaction with other melts. The arrows in Figure 19 show how the spinel compositions change with the effects of melt-rock reaction and interaction with either MORB or boninite. The SEP ophiolite spinel plot in the most undepleted end of the diagram and follow the anhydrous melting trend. Some of the Rivas and Descartes detrital spinel from the SE10-25 sample fall along the anhydrous melting trend and are indicative of early crystallization, minimal melt-rock reaction, and are less depleted in Al. Two more of these grains plot near the end of the DMM trend, and may indicate later crystallization of spinel along the curve or some melt-rock interaction that increased the TiO<sub>2</sub> content. The spinel from the PR-41 and LR-25 and -29 samples are either showing the effects of reaction with MORB melts or may be volcanic spinels (from melts themselves) and not peridotitic (from residues of mantle partial melts) at all. In either case, there is more melt-rock reaction of the detrital spinel than the ophiolitic spinel.

To determine whether the spinel is truly peridotitic or if it is volcanic, Figure 20 is a comparison of iron ratio ( $\text{Fe}^{2+}/\text{Fe}^{3+}$ ) to wt. % TiO<sub>2</sub> and fields for peridotitic and

volcanic spinel have been defined by Kamenetsky et al. (2001). All the SE10-25 samples fall within the peridotite spinel field and may be called true mantle spinel with  $<0.2$  TiO<sub>2</sub> wt. %. These are the spinel grains that fell close to the normal anhydrous melting trend of DMM, but these detrital spinel do not cluster together, nor do they plot similarly to the SEP ophiolite spinel. Figure 21 shows compositional relationships of volcanic spinels (based on basalt data) and compares wt. % Al<sub>2</sub>O<sub>3</sub> with wt % TiO<sub>2</sub>. The fields define tectonic provenance from MORB, BABB, ocean island basalts (OIB), or island arc (ARC) spinels. While the diagram was designed for volcanic spinel, it is useful to show how different the peridotitic spinels are to those from volcanic magmas. The mantle clinopyroxene fall outside of the defined fields, along with some of the SE10-25 data, because they are from mantle residues and not basalts; thus, the detrital spinel may be from more than one source, but they are not likely to be derived from the Santa Elena ophiolite.

## Paleocene-Eocene

Cross-sectional W-E view. Formation of andesitic island arc, with ephemeral carbonate platforms

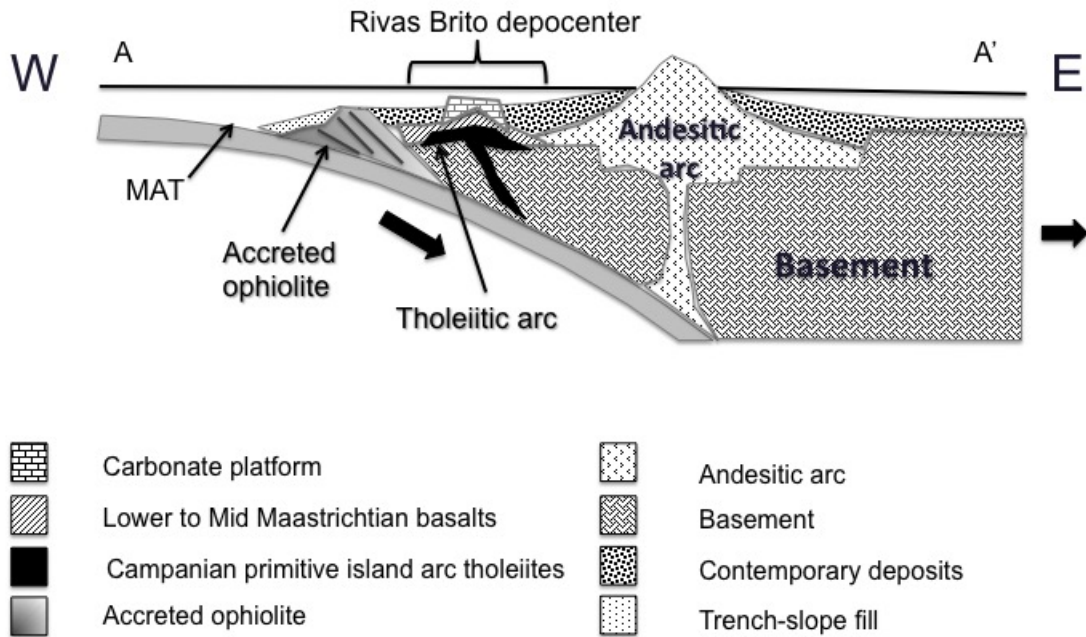


Figure 22. Cross-sectional view of northern Costa Rica from the Paleocene to early Eocene after Seyfried et al. (1987). Subsidence is occurring in the slope-trench area and in the forearc basin as the andesitic island arc develops. Ephemeral carbonate platforms appear on highs and shallow submerged areas.

### Mid-ocean ridge gabbroic sources

Another type of source input that was considered was gabbro, which may be part of an ophiolite sequence or from an oceanic spreading center, a mid-ocean ridge (MOR). Here we will consider a mid-ocean ridge gabbroic source. Using the end-member diagram (Figure A-6), the Rivas and Descartes clinopyroxene are compared to MOR gabbro clinopyroxene data, which plot as both diopside and augite. The detrital diopside grains plot similarly to the gabbroic diopside, and the augitic MOR clinopyroxene also

plot similarly to the detrital grains (and do not overlap the volcanic boulder samples from the turbidite conglomerate). There is good correlation with MOR gabbro compositionally. In the LeBas covariation diagram for silica and alumina (Figure A-14), the MOR gabbro samples also plot as sub-alkaline like the detrital samples. In the Leterrier et al. (1982) diagrams (Figures 9-11), the MOR gabbro samples also fall in the other basalts field. The next diagram then discriminates non-orogenic (MORB, BABB) and orogenic (calc-alkaline and tholeiitic) tectonic origins. While the MOR gabbro clinopyroxene comparison data do fall on either side of the discrimination line for non-orogenic and orogenic fields, this is because the non-orogenic field (dashed line) overlaps the orogenic field (dotted line). This suggests that while all the detrital and volcanic Rivas and Descartes grains fall under the discrimination line and into the orogenic field, that not all of these grains may be volcanic. Some of the samples that plot in the overlapping zones may be from a MOR setting, and the chondrite-normalized trace element diagrams show this to be the case.

In Figures A9-A12, chondrite-normalized trace element diagrams and extended diagrams compare the MOR gabbro patterns to the Rivas and Descartes detrital grain patterns. The detrital grains show a gently sloping LREE pattern, with a slight negative anomaly for Europium (Eu), and flat MREE and HREE slopes. Figures A-9 and A-10 compare the detrital grains to the data of Harigane et al., (in press) and the patterns are very similar in both the standard and extended trace element diagrams. The extended diagram (Figure A-10) also shows the MOR clinopyroxene are depleted in LREEs and Nb. There are also negative Zr and Ti anomalies, similar to the detrital grains. These

samples cover the high end of the range where the detrital grains plot; thus, it is possible that some of the clinopyroxene input is from a mid-ocean ridge source.

The detrital spinel grains plotted in Figure 20 show that only sample SE10-25 is truly peridotitic. The field for volcanic spinel covers a variety of tectonic environments including MORB-type rocks, BABB, subduction related magmas, and tholeiites from continental rifting. Other global comparison data plotted in this diagram are from MOR gabbros, volcanic arcs, and a backarc basin. All the comparison data from volcanic arc and backarc spinel fall within the volcanic field. The MOR gabbro data fall in a small corner of the peridotitic field, partly in the volcanic field, and partly in white space on the diagram. There may be room to add a MOR field here. The detrital spinel from the PR-41 and LR-25 and -29 samples fall within the volcanic field and have  $\text{TiO}_2$  wt % > 0.2 and lower  $\text{Fe}^{2+}/\text{Fe}^{3+}$  than the peridotitic spinel, but this is inconclusive for tectonic provenance because the field covers multiple tectonic environments.

Figure 21 defines tectonic environments of origin based on the compositional relationship of wt. %  $\text{Al}_2\text{O}_3$  vs. wt. %  $\text{TiO}_2$  from volcanic spinel ( $\text{TiO}_2 > 0.2$  wt. %). Global comparison data plotted in this diagram are from MOR gabbros, volcanic arcs, and a backarc basin. The MOR gabbro spinel data for the most part fall within the MORB field, although some of the comparison data is not within the field. The detrital spinel grains plot within the overlapping tectonic fields of MORB and BABB (geochemically almost indistinguishable), with one sample from LR-25 anomalously plotting as OIB. This may be explained because the MORB field may need to be expanded, as seen with the comparison MOR spinel data that also falls outside of the

field. Both spinel and clinopyroxene major and trace element data indicate a possible mid-ocean ridge provenance.

### **Arc volcanic rocks**

Looking at compositional end-member diagram for clinopyroxene (Figure 7), the clinopyroxene from the volcanic andesitic boulders found on the Descartes peninsula (plotted as open squares on the diagram) plot toward the end of the compositional spectrum for the Rivas and Descartes samples on the diagram. This figure also demonstrates the compositional variability of clinopyroxene grains that are from the same parent magma. The SE10-25 detrital clinopyroxene samples are comparable to the volcanics at the end of the range, but this is not conclusive, as the andesitic grains show a range of augitic compositions. Using the compositional end-member diagram to compare the detrital grains to global volcanic arc clinopyroxene (Figure A-7), there is a larger compositional area that the arc volcanics cover from diopside to augite, similar to both the detrital and volcanic Rivas and Descartes samples.

The LeBas covariation diagram (Figure 14) shows that both the andesite samples and global clinopyroxene data are sub-alkaline like the detrital grains. The Leterrier et al., (1982) diagram (Figure 9) shows both the andesitic clinopyroxene grains from Descartes and the global volcanic arc data plot within the other basalts category. Further discrimination in Figure 10 shows that the andesite samples fall within the orogenic basalt field (dotted line) and below the discrimination line. The global arc data fall primarily within the orogenic basalt field, but some of the data fall within the overlapping area of the non-orogenic basalt and within the non-orogenic field. This suggests

geochemical similarities between MOR environments and volcanic arc environments. Finally in Figure 11, the volcanic data are divided into calc-alkaline and tholeiitic fields. The andesitic EP clinopyroxenes fall within the calc-alkaline category as expected, while the global volcanic arc clinopyroxene and detrital clinopyroxene plot as both calc-alkaline and tholeiitic. The Leterrier diagrams suggest two different volcanic magma sources for the detrital clinopyroxene from the Rivas and Descartes turbidites.

The detrital clinopyroxene grains have been plotted with the andesitic Descartes clinopyroxene data and the global volcanic arc clinopyroxene data in chondrite-normalized trace diagrams (see Figures A-11 to A-12). The andesite clinopyroxene patterns cover the high range of the data and have a similar pattern to the detrital samples, including gently dipping LREE patterns, negative Eu anomalies, and flat HREE patterns. The volcanic arc clinopyroxene patterns have a flatter Eu anomaly than the detrital clinopyroxene and cover the low to mid range of the detrital clinopyroxene data. The plot of HFSEs to REEs (Figure 17) shows the andesite sample (EP 46) is more depleted in HFSEs compared to REEs, and the detrital clinopyroxene cluster nearer those data and Fijian arc clinopyroxene, than they do MOR and BAB sources. This diagram indicates more of a subduction-zone, volcanic origin for the detrital clinopyroxene over a MOR origin.

The detrital spinel grains plotted in Figure 20 fall within the field for volcanic spinel, which covers a variety of tectonic environments, including subduction related magmas. Comparison data plotted in this diagram are from global volcanic arc data. All the comparison spinel data plot within the volcanic field. The detrital spinel from the PR-41 and LR-25 and -29 samples fall within the volcanic field and look similar to the

comparison volcanic arc spinel data. Figure 21 defines tectonic provenance fields based on volcanic basalt data. Global comparison data from volcanic arc spinel fall within the volcanic arc field as expected, as well as in the lower portion of the MORB field, and within the BABB field. The detrital spinel samples from PR-41 and LR-25 and LR-29 do not plot in the volcanic arc field, but do plot similarly to arc tholeiite data (closed green triangles) within the BABB field. The detrital spinel data suggest a possible tholeiitic arc source and the clinopyroxene major and trace element data indicate two possible volcanic arc sources: tholeiitic arc and calc-alkaline arc. Three different trends for sediment source rocks emerge based on geochemical data from the detrital clinopyroxene and spinel from the Rivas and Descartes turbidites. These are the rocks that would have eroded and sourced the sediment input to the forearc basin, including a mantle-derived, abyssal peridotite source, a source rock more closely related to a MOR-type source, and volcanic sources that are tholeiitic and calc-alkaline.

### **Paleogeography of Paleocene-Eocene Central America**

The larger tectonic and depositional setting of the Late Cretaceous to late Eocene provides a foundation for understanding the provenance of the Rivas and Descartes detrital spinel and clinopyroxene grains. Before (and during) deposition of either the Rivas or Descartes turbidites occurred, the pre-existing rock types were ophiolitic bodies (peridotites, gabbros, diorites, dunites, basalts), CLIP (Nicoya complex), primitive island arc tholeiitic basalts, carbonates, and calc-alkaline andesitic island arc basalts. Dominant deposition from the Campanian to Eocene was, deep marine basin plain turbidites, along with intermittent channelized and lobe turbidite deposits and pelagic to hemipelagic

carbonate sedimentation. The long-sustained outer arc high confined these turbidite deposits to the west in the Sandino Basin while the forearc basin opened during initiation of the subduction-induced volcanic arc. Paleocurrent data from Astorga (1988) point to two major distribution patterns along the Pacific margin; one longitudinal pattern that controls primary sedimentation in the basin. It parallels the basin axis and is more characteristic of deep basin plain turbidite deposits and lobes. The second pattern is transverse and is more characteristic of channels, slump deposits, and local lobes; it is coincident with basin sediment entry points (see Figure 23,24).

Figures 23 and 24 are schematic map views of inferred paleogeography of Costa Rica from the Paleocene through the Eocene, during the time of the Rivas and Descartes Formation deposition. The map shows the location of the modern coast, the location of the Sandino Basin, where the arc would have been located, hypothetical and inferred sediment source inputs, paleocurrent directions (longitudinal and transverse), and different emerged terranes (of unnamed lithology), many surrounded by carbonate platforms. As the geochemical data suggest, these emerged bodies may be ophiolite bodies, remnants of the oceanic CLIP, primitive tholeiitic arc or new volcanic islands forming from the andesitic arc.

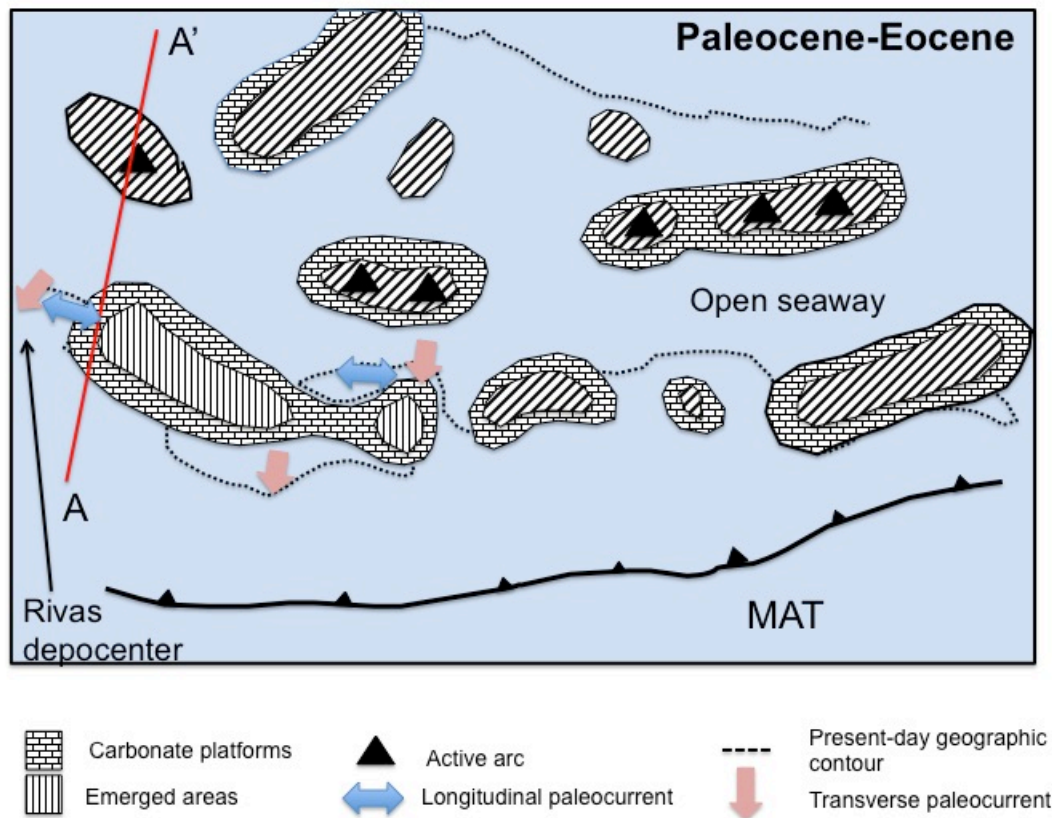


Figure 23. Map of the open seaway during the Paleocene to Eocene, showing the Middle America Trench (MAT) and emerged terranes that may be ophiolitic, MOR-related, tholeiitic volcanic, or andesitic at the active arc (after Astorga et al., 1991).

Longitudinal paleocurrents are associated with basin plain turbidites (low-density deposits). These currents can transport the medium- to fine-grained deposits along the trench over distances up to 1,000 km. While the geochemical data from the clinopyroxene and spinel do not indicate that the Santa Elena ophiolite is a sediment source, one of the longitudinal currents may have carried sediments from a different eroded ophiolitic body from elsewhere along the Pacific coast. It is possible that another ophiolite massif contains gabbros that are the source of the clinopyroxene with MOR gabbro character. Another possibility of a mantle source in the seaway is an unknown ophiolite body that may not be known or discovered in Costa Rica because the Miocene

and younger volcanics would have covered it. It is recognized that Central America is partly composed of accreted forearc ophiolite bodies and this may be one such body that remains hidden.

Transverse paleocurrents deposited local lobes and conglomeratic, channelized deposits such as those seen in the Descartes Formation. Forearc basins are known to be fed by sediments from the active arc, and geochemical data suggest this happened. The tectonic history indicates tholeiitic arc volcanism through the Maastrichtian that eventually transitioned into andesitic arc volcanism. The hypothetical and inferred entry points in Figure 24 are well positioned to source the active arc and act as an efficient delivery system for sediment from the arc. As the tholeiitic arc was active until the end Cretaceous, it is expected that the older Rivas deposits would have the more tholeiitic clinopyroxene. The BH-13 and SE10-25 samples from the Rivas Formation do plot in the tholeiitic field within the overlapping area on the diagram in Figure 11. These sediments were possibly sourcing the primitive tholeiitic arc that began to transition into a more andesitic character by the early Paleocene. These sediments may be remnants of the older arc volcanics that are either missing or may also be covered by the Miocene and younger volcanics. The tholeiitic signature of the Rivas detrital clinopyroxene may also point to the Nicoya Complex tholeiitic basalts as another source input.

Pebbly to conglomeratic channel fills characteristic of transverse paleocurrents indicate shorter transport distances from the source, as evidenced by andesitic boulders from conglomerate in the late Paleocene to Eocene Descartes Formation. The clinopyroxene from the conglomeratic andesite cobbles have a calc-alkaline geochemical character that point to a source from the andesitic island arc volcanics that initiated in the

late Maastrichtian-early Paleocene. The detrital clinopyroxene grains from PR-42 are also calc-alkaline and also suggest the active andesitic arc as a source.

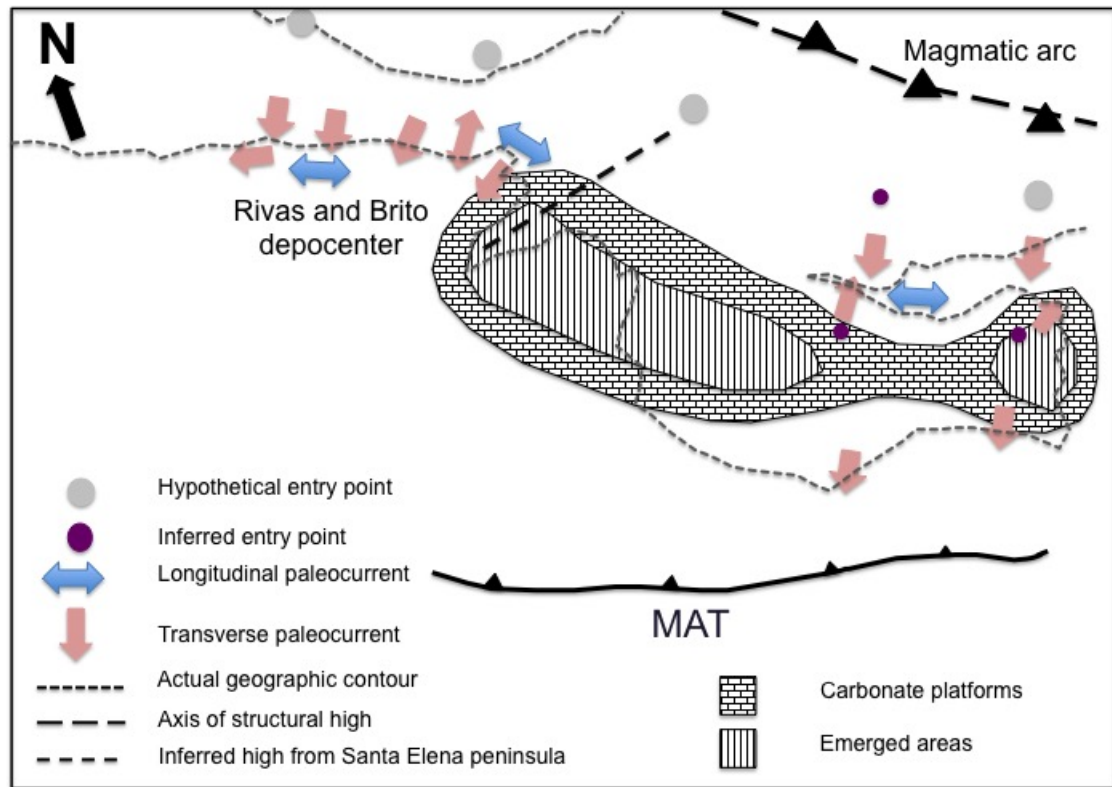


Figure 24. Paleocene to Eocene paleogeography showing the Middle America Trench (MAT), the emerged outer arc with carbonate build ups, the inner forearc, paleocurrent patterns, structural highs and hypothetical and inferred entry points during the depositional time period for the Rivas and Descartes Formations (after Astorga, 1987; and Astorga et al., 1991). The Late Paleocene to early Eocene was a relatively stable time for tectonics, explosive andesitic volcanics developed during this time, and carbonate platforms built up during periods of volcanic quiet.

## Conclusions

The Rivas and Descartes Formation turbidites contain detrital spinel and clinopyroxene. The possible sources for these minerals are the ultramafic or mafic section of an ophiolite, mid-ocean ridge gabbros or basalts, tholeiitic basalts, or calc-alkaline volcanic arc andesites. Geochemical analyses of these minerals narrows can help identify specific tectonic environments.

1. Heavy minerals from this study of the sandstones consist of plagioclase, clinopyroxene, and spinel.
2. Clinopyroxene are mostly augitic (with some diopside), and are chemically similar to sub-alkaline, and both calc-alkaline and tholeiitic clinopyroxenes.
3. Trace elements of clinopyroxene do not reflect the same residual mantle origin as the Santa Elena ophiolites.
4. Spinel are moderately to highly aluminum-depleted.
5. Some spinel are similar to Santa Elena mantle spinel and some are not.
6. Provenance of clinopyroxene based on mineral chemistry suggests upper crustal gabbroic to volcanic sources, not mantle sources.
7. Spinel mineral chemistry suggests the provenance of source areas as ophiolitic (but not Santa Elena ophiolite mantle), with arc and MOR influences.
8. The paleogeography suggests the possibility of multiple source inputs including ophiolites and magmatic arc (accreted terranes).
9. These accreted terranes ultimately became the foundation that blocked the seaway in the Miocene and triggered onset of glaciation.

Because the exact geomorphology of the Pacific coast of Costa Rica from the Paleocene to Eocene is unknown, the sediment source rocks must be inferred from both modern geomorphology of the coast and the geochemical signature of detrital grains from the syn-tectonic deposits in the forearc Sandino Basin. The mantle spinel suggest a peridotite input, but probably not from the Santa Elena ophiolite; mantle input may be from either a different ophiolite body somewhere along the coast or from mantle rocks that are now covered by Tertiary volcanics or have been completely eroded. The character of the crustal minerals suggests sources from MOR gabbros (possibly from the Nicoya Complex or from other CLIP remnants along the Pacific coast), and island arc tholeiites and andesites. Understanding the geochemistry of the detrital grains within the Rivas and Descartes Formation deposits also reveals information about the Late Cretaceous to Eocene volcanic arcs in Costa Rica. While there are no known outcrops for these volcanic rocks, the detrital grains reveal information about what the arc may have looked like at that time. The detrital spinel and clinopyroxene suggest that during the early history of the Panama seaway, sediment sources filling the forearc Sandino Basin were dominated first by older ophiolites then by volcanic input from the evolving island arc. Ultimately these sediments were deposited at a time the seaway was open and forearc basins were being filled with massive amounts of sediment; this sedimentary fill contributed to the eventual closing of the isthmus in the Miocene, leading to significant changes in global climate.

## References

Aldanmaz, E., Schmidt, M.W., Gourgaud, A. & Meisel, T., 2009. Mid-ocean ridge and supra- subduction geochemical signatures in spinel-peridotites from the Neotethyan ophiolites in SW Turkey: Implications for upper mantle melting processes. *Lithos* 113, 691-708

Alvarado, G.E., Kussmaul, S., Chiesa, S., Gillot, P.Y., Appel, H., Worner, G., Rundle, C., 1992. Resumen cronoestratigráfico de las rocas ígneas de Costa Rica basado en dataciones radiométricas. *Journal of South American Earth Sciences* 6, 151-168.

Alvarado, G.E., Dengo, C., Martens, U., Bundschuh, J., Aguilar, T., Bonis, S.B., 2007. Stratigraphy and geologic history. In: Bundschuh, J., Alvarado, G.E., (Eds.), *Central America: Geology, Resources, and Hazards*. Taylor & Francis, London, UK, pp. 239-266.

Astorga, A., 1988. Geodinámica de las cuencas del Cretácio Superior-Paleógeno de la region “forearc” del sure de Nicaragua y Norte de Costa Rica. *Revista Geologica de America Central* 9, 1-40.

Astorga, A., Fernandez, J.A., Barboza, G., Campos, L., Obando, J., Aguilar, A., and Obando, L.G., 1991. Cuencas sedimentarias de Costa Rica: Evolución géodinamica y potential de hidrocarburos. *Revista Geologica de America Central*, 13, 15-59.

Azema, J. & Tournon J., 1980. La peninsule de Santa Elena, Costa Rica: un massif ultrabasiqne charrie en marge pacifique de L'Amérique Centrale. *Costa Rica: Comptes Rendus de L'Academie des Sciences des Paris* 290, 9 - 12.

Azéma, J., Origlia, I., Tournon, J., DeWever, P., 1982. Nouvelles données sur la présence de Crétacé Moyen au sein des formations volcano-sédimentaires de l'autochtone relatif de la péninsule de Santa Elena (Costa Rica, Amérique Centrale). 9a Réunion annuelle des Sciences de la Terre. Paris, Société Géologique de France, 22.

Baumgartner, P.O., Mora, C.R., Butterlin, J., Sigal, J., Glacon, G., Azéma, J., and Bourgois, J., 1984. Sedimentación y paleogeografía del Cretácico y Cenozoico del litoral pacífico de Costa Rica. *Revista Geológica de América Central* 1, 57-136.

Baumgartner, P.O. & Denyer, P. 2006. Evidence for middle Cretaceous accretion at Santa Elena Peninsula (Santa Rosa Accretionary Complex), Costa Rica. *Geologica Acta* 4, 179 - 191.

Beccaluva, L., Chinchilla - Chavez, A.L., Coltori, M., Giunta, G., Siena, F. & Vaccaro, C. 1999. Petrologic and structural significance of the Santa Elena - Nicoya Ophiolitic Complex in Costa Rica and geodynamic implications. *European Journal of Mineralogy* 11, 1091 - 1107.

Bellon, H. & Tournon, J., 1978. Contribution de la géochronométrie K-Ar à l'étude du magmatisme de Costa Rica, Amérique Centrale. *Bulletin Société Géologique de France* 6, 955 - 959.

Bice, K. L., Marotzke, J. 2002. Could changing ocean circulation have destabilized methane hydrate at the Paleocene/Eocene boundary?. *Paleoceanography*, 17, 8-1 – 8-12.

Bergoeing, J.P., 2007. *Geomorfología de Costa Rica*. Librería Francesa, San José, Costa Rica, pp. 1-328.

- Brass, G.W., Southam, J.R., Peterson, W.H., 1982. Warm saline bottom water in the ancient ocean. *Nature*, 328, 123-126.
- Calvo, C. 2003. Provenance of plutonic detritus in cover sandstones of Nicoya Complex, Costa Rica: Cretaceous unroofing history of a Mesozoic ophiolite sequence. *Geological Society of America Bulletin* 115, 832-844.
- Cawood, P.A., 1983. Modal composition and detrital clinopyroxene geochemistry of lithic sandstones from the New England Fold Belt (east Australia): A Paleozoic forearc terrane. *Geological Society of America Bulletin* 94, 1199-1214.
- Choi, S.H., Shervais, J.W. & Mukasa, S.B. 2008. Supra-subduction and abyssal mantle peridotites of the Coast Range ophiolite, California. *Contrib. Mineral. Petrol.* 156, 551 - 576.
- DeMets, C. 1995. Plate motion and crustal deformation. *Reviews of Geophysics* 33, 365 - 369.
- Dengo, G. 1962. Tectonic-igneous sequence in Costa Rica. In: Engel, A.E.J., James, H.J., Leonard, B.F. (Editors). A volume to honor A.F. Budington. *Geological Society of America Special Volume*, 133 - 161.
- Denyer, P. & Gazel, E. 2009. The Costa Rican Jurassic to Miocene oceanic complexes: Origin, tectonics and relations. *Journal of South American Sciences* 28, 429-442.

Denyer, P., Baumgartner, P.O. & Gazel, E. (2006). Characterization and tectonic implications of the Mesozoic - Cenozoic oceanic assemblages of Costa Rica and Western Panama. *Geologica Acta* 4, 219 - 235.

Denyer, P., Montero, W., Flores, K., 2005. Apuntes sobre al geología de las hojas Golfo y Berrugate, Costa Rica. *Revista Geológica de América Central* 32, 99-108.

DeWever, P., Azema, J., Tournon, J., & Desmet, A. 1985. Decouverte de materiel oceanique du Lias-Dogger inferieur dans la peninsule de Santa Elena (Costa Rica, Amerique Centrale). *Comptes Rendus de L'Academie des Sciences des Paris* 300, 759 - 764.

Dick, H.J.B., Bullen, T., 1984. Chromian spinel as a petrogenetic indicator in abyssal and alpine-type peridotites and spatially associated lavas. *Contributions to Mineralogy and Petrology* 86, 54-76.

Dick, H.J.B., Fisher, R.L. & Bryan, W.B. (1984). Mineralogic variability of the uppermost mantle along mid-ocean ridges. *Earth and Planetary Science Letters* 69, 88-106.

DiMarco, G., Baumgartner, P.O. & Channel, J.E.T. (1995). Late Cretaceous - early Tertiary paleomagnetic data and a revised tectonostratigraphic subdivision of Costa Rica and western Panama. In: Mann, P. (Editor). *Geological and tectonic development of the Caribbean Plate Boundary in Southern Central America*. Geological Society of America Bulletin Special Papers 295, 1 - 27.

- Einsle, G., 2000. Sedimentary Basins: Evolution, Facies, and Sediment Budget. Springer-Verlag, Berlin.
- Estes, R., & Hutchison, J. H. 1980. Eocene lower vertebrates from Ellesmere Island, Canadian Arctic Archipelago. *Palaeogeography, Palaeoclimatology, Palaeoecology*, 30, 325-347.
- Flueh, E.R., von Huene, R., 2007. Crustal structure. In: Bundschuh, J., Alvarado, G.E., (Eds.), *Central America: Geology, Resources, and Hazards*. Taylor & Francis, London, UK, pp. 267-276.
- Flores, K., Denyer, P., & Aguilar, T., 2003. Geología y estratigrafía de la hoja Abangares: Guanacaste, Costa Rica. *Revista Geológica de América Central* 29, 127-136.
- Galli-Olivier, C., 1979. Ophiolite and island-arc volcanism in Costa Rica. *Geological Society of America Bulletin*, 90, 444-452.
- Gazel, E., Denyer, P., Baumgartner, P.O. 2006. Magmatic and geotectonic significance of Santa Elena Peninsula, Costa Rica. *Geologica Acta* 4, 193 - 202.
- Gazel, E., Carr, M.J., Hoernle, K., Feigenson, M.D., Szymanski, D., Hauff, F., van den Bogaard, P., 2009. Galapagos-OIB signature in southern Central America: Mantle refertilization by arc-hot spot interaction. *Geochemistry Geophysics Geosystems* 10.
- Gose, W.A., 1983. Late Cretaceous-Early Tertiary tectonic history of southern Central America. *Journal of Geophysical Research* 88, 10585-10592.

Hauff, F., Hoernle, K., Schmincke, H.-U., Werner, R., 1997. A mid Cretaceous origin for the Galapagos hotspot: volcanological, petrological and geochemical evidence from Costa Rica oceanic crustal fragments. *Geologische Rundschau* 86, 141-155.

Hauff, F., Hoernle, K., Bogaard, P., 2000. Age and geochemistry of basaltic complexes in western Costa Rica: Contributions to the geotectonic evolution of Central America. *Geochemistry, Geophysics, Geosystems* 1, 1 - 41.

Hawkesworth, C. J., Gallagher, K., Hergt, J. M., McDermott, F., 1994. Destructive plate margin magmatism: geochemistry and melt generation. *Lithos*, 33, 169-188.

Hellebrand, E., Snow, J.E., Dick, H.J.B., Hofmann, A.W., 2001. Coupled major and trace elements as indicators of the extent of partial melting in mid-ocean-ridge peridotites. *Nature* 410, 677 - 681.

Hoernle, K., Hauff, F., 2007. Oceanic Igneous Complexes. In: Bundschuh, J., Alvarado, G.E., (Eds.), *Central America: Geology, Resources, and Hazards*. Taylor & Francis, London, UK, pp. 523-548.

Hoernle, K., Hauff, F., van den Bogaard, P. 2004. 70 m.y. history (139 - 69 Ma) for the Caribbean large igneous province. *Geology* 32, 697 - 700.

James, K.H., 2007. Structural geology: From local elements to regional synthesis. In: Bundschuh, J., Alvarado, G.E., (Eds.), *Central America: Geology, Resources, and Hazards*. Taylor & Francis, London, UK, pp. 277-322.

Johnson, K. T., Dick, H. J., & Shimizu, N. (1990). Melting in the oceanic upper mantle: an ion microprobe study of diopsides in abyssal peridotites. *Journal of Geophysical Research*, 95, 2661-2678.

Kamenetsky, V.S., Crawford, A.J., Meffre, S., 2000. Factors controlling chemistry of magmatic spinel: an empirical study of associated olivine, Cr-spinel and melt inclusions from primitive rocks. *Journal of Petrology* 42, 655-671.

Kelemen, P.B. 1990. Reaction between Ultramafic Rocks and Fractionating Basaltic Magma I. Phase Relations, the Origin of Calc-alkaline Magma Series, and the Formation of Discordant Dunite. *Journal of Petrology* 31, 51 - 98.

Kumpulainen, R.A., 1995. Stratigraphy and sedimentology in western Nicaragua. *Revista Geológica de América Central* 18, 91-94.

Le Bas, J.M., 1962. The role of aluminum in igneous clinopyroxenes with relation to their parentage. *American Journal of Science* 260, 267-288.

Lenaz, D., Kamenetsky, V.S., Crawford, A.J., Princivalle, F., 2000. Melt inclusions in detrital spinel from the SE Alps (Italy-Slovenia): a new approach to provenance studies of sedimentary basins. *Contributions to Mineralogy and Petrology* 139, 748-758.

Leterrier, J., Maury, R.C., Thonon, P., Girard, D., Marchal, M., 1982. Clinopyroxene composition as a method of identification of the magmatic affinities of paleo-volcanic series. *Earth and Planetary Science Letters* 59, 139-154.

Lowe, D. R., 2004. Deep water sandstones: Submarine canyon to basin plain, western California. AAPG Pacific Section Special Publication, GB 79, 1-79.

Lowe, D. R., 1982. Sediment gravity flows: II Depositional models with special reference to the deposits of high-density turbidity currents. *Journal of Sedimentary Research*, 52, 279-297.

Mann, P., Rogers, R.D., Gahagan, L., 2007. Overview of plate tectonic history and its unresolved tectonic problems. In: Bundschuh, J., Alvarado, G.E., (Eds.), *Central America: Geology, Resources, and Hazards*. Taylor & Francis, London, UK, pp. 201-238.

Marshall, J.S., 2007. The Geomorphology and Physiographic Provinces of Central America. In: Bundschuh, J., Alvarado, G.E., (Eds.), *Central America: Geology, Resources, and Hazards*. Taylor & Francis, London, UK, pp. 75-122.

McDonough, W.F., Sun, S. –s., 1995. The composition of the Earth. *Chemical Geology* 120, 223-253.

McKenzie D. & Bickle, M.J., 1988. The Volume and Composition of Melt Generated by Extension of the Lithosphere. *Journal of Petrology* 29, 625-679.

Minster, J. B., Jordan, T. H., 1978. Present-day plate motions. *Journal of Geophysical Research* 83, 5331–5354.

- Montes, C., Cardona, A., Jaramillo, C., Pardo, A., Silva-Tamayo, J.C, Valencia, V., Ayala, C, Pérez--Angel, L.C., Rodríguez-Parra, L.C., Ramirez, V., Niño, H., 2015. Middle Miocene closure of the Central American Seaway. *Science* 348, 226 - 229
- Morimoto, N., 1988. Nomenclature of Pyroxenes. *Mineralogy and Petrology* 39, 55-76.
- Morton, A.C., 1991. Geochemical studies of detrital heavy minerals and their application to provenance research. Geological Society, London, Special Publications 57, 31-45.
- Nisbet, E.G., Pearce, J.A., 1977. Clinopyroxene composition in mafic lavas from different tectonic settings. *Contributions to Mineralogy and Petrology* 63, 149-160.
- Parkinson, I.J. & Pearce, J.A. 1998. Peridotite from the Izu-Bonin-Mariana Forearc (ODP Leg 125): Evidence for Mantle Melting and Melt-Mantle Interaction in a Supra-Subduction Zone Setting. *Journal of Petrology* 39, 1577 - 1618.
- Pindell, J.L., Kennan, L., 2009. Tectonic evolution of the Gulf of Mexico, Caribbean and northern South America in the mantle reference frame: an update. Geological Society, London, Special Publications 328, 1-55.
- Pindell, J.L., Kennan, L., Stanek, K.P., Maresch, W.V. & Draper, G. 2006. Foundations of Gulf of Mexico and Caribbean evolution: eight controversies resolved. *Geologica Acta* 4, 303-341.
- Piper, D.K.W., Normark, W.R., 1983. Turbidite depositional patterns and flow characteristics, Navy Submarine Fan, California Borderland. *Sedimentology*, 30, 681-694.

Poulsen, C. J., Barron, E. J., Arthur, M. A., Peterson, W. H. 2001. Response of the mid-Cretaceous global oceanic circulation to tectonic and CO<sub>2</sub> forcings. *Paleoceanography*, 16, 576-592.

Ranero, C., von Huene, F., Flueh, E., Duarte, M., Baca, D., and McIntosh, K., 2000. A cross section of the convergent Pacific margin of Nicaragua. *Tectonics*, 19, 335-357.

Ranero, C. R., Von Huene, R., Weinrebe, W., Barckhausen, U., 2007. Convergent margin tectonics: A marine perspective. In: Bundschuh, J., Alvarado, G.E., (Eds.), *Central America: Geology, Resources, and Hazards*. Taylor & Francis, London, UK, pp. 239-266.

Schmidt - Effing, R. 1980. Radiolarien der Mittel-Kreide aus dem Santa Elena - Massiv von Costa Rica. *Neues Jahrbuch Geologie und Paläontologie* 160, 241 - 257.

Seyfried, H., Astorga, A., Calvo, C., 1987. Sequence stratigraphy of deep and shallow water deposits from an evolving island arc: the upper Cretaceous and Tertiary of southern Central America. *Facies* 17, 203-214.

Sinton, C.W., Duncan, R.A. & Denyer, P. 1997. Nicoya peninsula: a single suite of Caribbean oceanic plateau magmas. *Journal of Geophysical Research* 102, 15507 - 15520.

Stalder, R., Foley, S. F., Brey, G. P., Horn, I. 1998. Mineral-aqueous fluid partitioning of trace elements at 900–1200 C and 3.0–5.7 GPa: new experimental data for garnet, clinopyroxene, and rutile, and implications for mantle metasomatism. *Geochimica et Cosmochimica Acta*, 62, 1781-1801.

- Stow, D.A.V., 1986. Deep clastic seas. In: Reading, H.G., (Ed.), *Sedimentary Environments and Facies*. Blackwell, Oxford, UK, pp. 399-444.
- Struss, I., Artiles, V., Cramer, B., and Winsemann, J., 2008. The petroleum system in the Sandino forearc basin, offshore western Nicaragua. *Journal of Petroleum Geology* 31, 221-244.
- Tournon, J. 1984. *Magmatismes du Mesozoique a l'actuel en Amerique Centrale: L'exemple de Costa Rica, des ophiolites aux andesites*. PhD Thesis, University Pierre and Marie Curie.
- Twiss, R. J., Moores, E. M., 1992. *Structural Geology*. W.H. Freeman and Company, New York.
- Walther, C.H.E., Flueh, E.R., Ranero, C.R., Von Huene, R., Strauch, W., 2000. Crustal structure across the Pacific margin of Nicaragua: evidence for ophiolitic basement and a shallow mantle sliver. *Geophysical Journal International* 141, 759-777.
- Wegner, W., Wörner, G., Harmon, R.S., Jicha, B.R., 2011. Magmatic history and evolution of the Central American Land Bridge in Panama since Cretaceous times. *Geological Society of America Bulletin* 123, 703-724.
- Weyl, R., 1980. *Geology of Central America*. Gebruder Borntraeger, Berlin, pp. 1-371.
- Workman, R.K. & Hart, S.R., 2005. Major and Trace Element Composition of the Depleted MORB Mantle (DMM). *Earth and Planetary Science Letters* 231, 53 - 72.

Wright, S. C., 2011. Major and trace element geochemistry of peridotites and their tectonic implications: Santa Elena ophiolite complex, northwest Costa Rica. M. Sc. Thesis, University of Houston, Texas

## **Appendix I: Sample locations and maps**



Figure A-1. Map of Santa Elena and Descartes peninsulas with sample locations indicated by pins.



Figure A-2. Map of Santa Elena peninsula with both sample locations marked by pins and measured strikes and dips indicated on map.

Table A-1. Sample locations with strike and dip measurements.

Reference point	Latitude decimal	Longitude decimal	Strike	Dip
1	10.94148333	-85.86816667	N75E	45 NW
2	10.9425	-85.8703	N80E	45 NW
3	10.91761667	-85.7863	N85E	35 NW
4	10.93585	-85.73341667	N85W	30 NE
5	10.93831667	-85.734	N85W	20 NE
6	10.93928333	-85.73311667	N88E	28 NW
7	10.93026667	-85.73983333	N60W	30 NE
8	10.95155	-85.70813333	N70W	35 NE
9	10.95141667	-85.7074	N65W	25 NE
10	10.95053333	-85.7067	N55W	40 NE
11	10.94911667	-85.70486667	N50W	43 NE
12	10.94971667	-85.70371667	EW	34 N
13	10.92493333	-85.81755	N64W	56 NE

14	10.92513333	-85.81833333	N64W	55 NE
15	10.9245	-85.6938	N75E	41 NW
16	10.93478333	-85.70481667	N88E	24 NW
17	10.9348	-85.69276667	N85E	42 NW
18	10.9635	-85.69276667	N35W	78 NE
19	10.95251667	-85.69623333	N50W	15 NE
20	11.0298666667	-85.70693333	N70W	15 NE
21	11.0286	-85.70883333	EW	18 N
22	11.03265	-85.7457	N83W	56 NE
23	11.0441333333	-85.72278333	N75W	25 NE
24	11.0077833333	-85.6845	N60W	28 NE
25	10.9916333333	-85.68875	N70W	35 SW
26	10.98125	-85.68636667	N70E	68 SE
27	10.9912833333	-85.68831667	N70W	36 SW
28	11.0080333333	-85.73386667	N55W	30 SW
29	11.02015	-85.70821667	EW	45 N

30	10.9250166667	-85.81836667	N85W	74 NE
31	10.9464	-85.65521667	N85E	30 NW
32	10.9487833333	-85.6548	N70W	45 NE
33	11.01125	-85.7406	N60E	13 NW
34	11.0139833333	-85.74005	N80W	30 NE
35	11.0164666667	-85.73903333	N65W	65 NE
36	11.0206666667	-85.73681667	N68W	82 NE
37	11.0268166667	-85.74773333	N75E	21 NW
38	11.0274	-85.75008333	N60W	29 SW
39	11.0267166667	-85.69568333	N78E	28 NW

## **Appendix II: Additional diagrams**

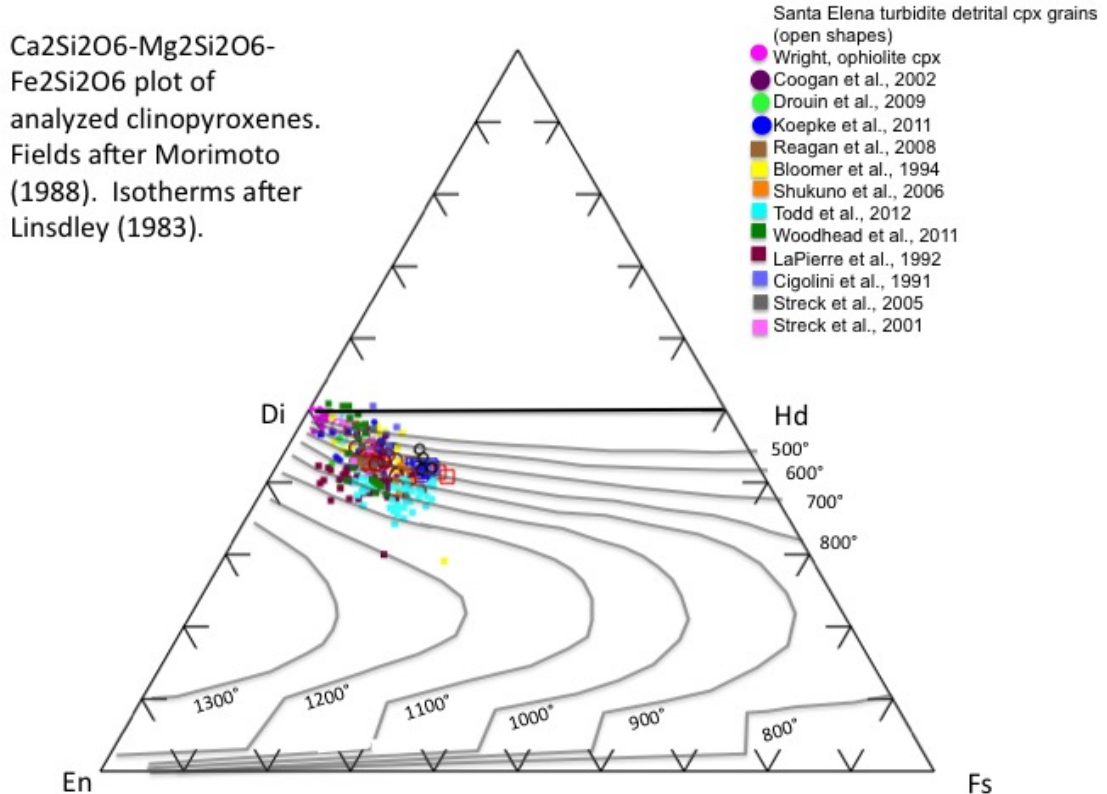


Figure A-3. Clinopyroxene end-member compositional diagram with isotherms superimposed on top of it. This diagram shows the Santa Elena detrital clinopyroxene grains (open circles) and the conglomeratic andesite boulder clinopyroxene grains (open squares) from the Descartes Formation. Also included in this plot are samples from global sources: peridotite clinopyroxene (magenta closed circles), mid-ocean ridge gabbros (closed purple, green, blue circles), and volcanic arc samples (closed squares). Isotherms indicate different crystallization temperatures for the different tectonic environments, or for the peridotite clinopyroxene, the temperature at which the peridotite residues were melted. This figure shows that the turbidite clinopyroxene were crystallized in the range of 600-800°, while the peridotite clinopyroxene were melted at 500°. The MOR clinopyroxene were also crystallized between 600-800°, while the volcanic arc pyroxene were crystallized over a broader range and at higher temperatures (500-1100°). The Santa Elena detrital grains are dissimilar to the ophiolite clinopyroxene data, but similar to the MOR gabbro and volcanic arc clinopyroxene data.

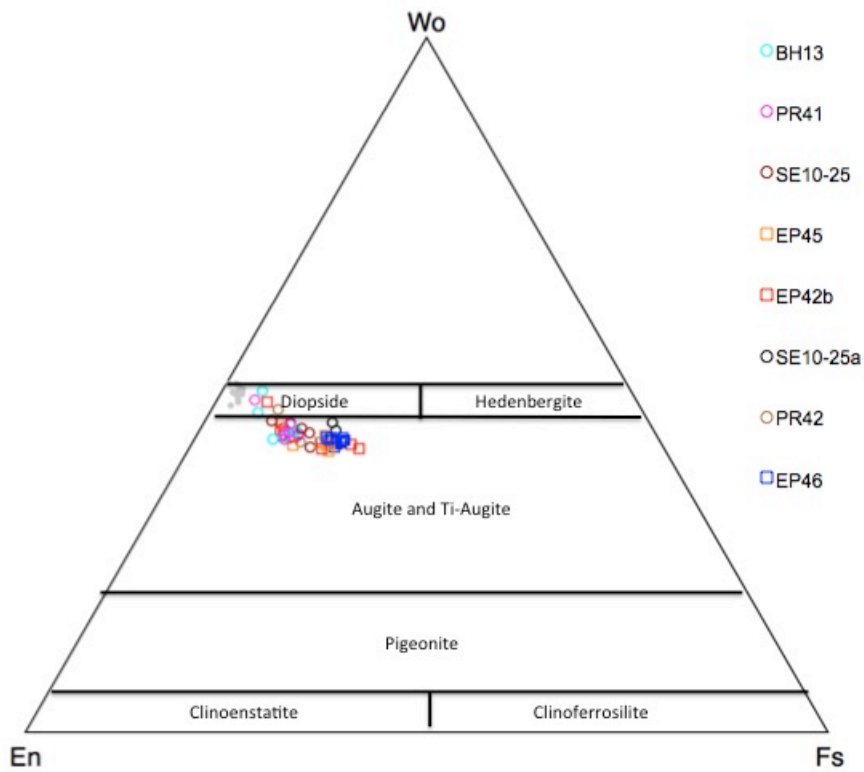


Figure A-4. Compositional end-member diagram for pyroxenes (fields after Morimoto, 1988). Rivas and Descartes Formation detrital clinopyroxene data (open shapes) compared to mantle peridotite clinopyroxene in grey from Wright (2011).

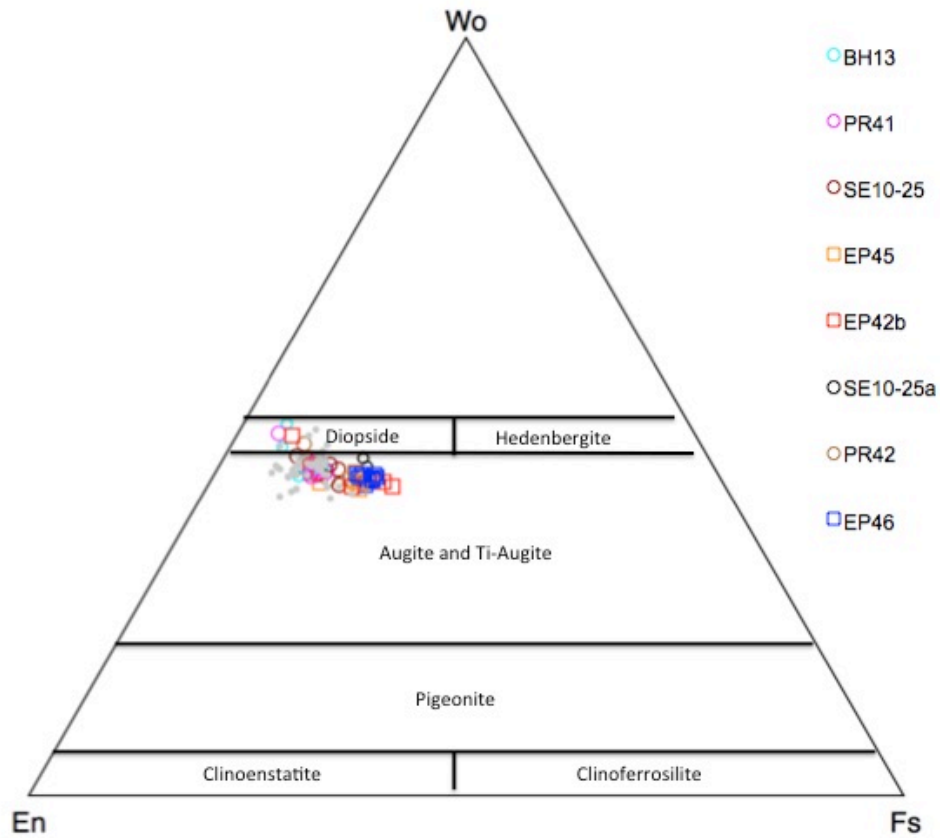


Figure A-6. Compositional end-member diagram for pyroxenes (fields after Morimoto, 1988). Rivas and Descartes Formation detrital clinopyroxene data (open shapes) compared to clinopyroxene from mid-ocean ridge gabbros in grey (Coogan et al., 2002; Drouin et al., 2009; Koepke et al., 2011).

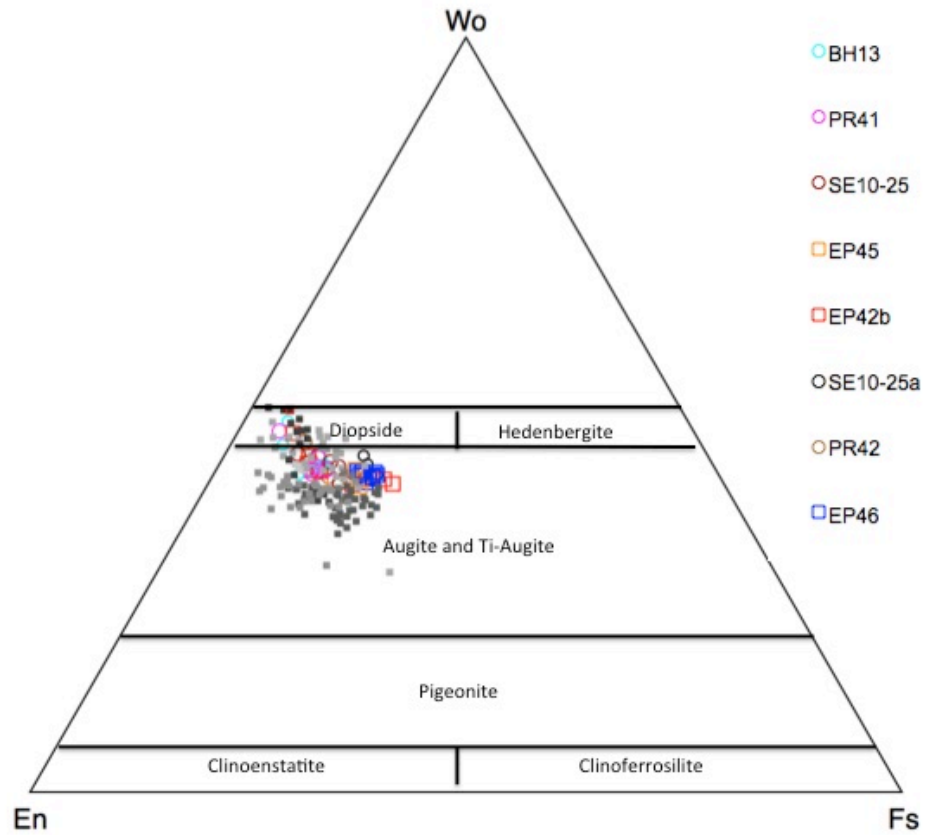


Figure A-7. Compositional end-member diagram for pyroxenes (fields after Morimoto, 1988). Rivas and Descartes Formation detrital clinopyroxene data (open shapes) compared to clinopyroxene from volcanic arcs in grey (Reagan et al., 2008; Bloomer et al., 2008; Shukuno et al., 2006; Todd et al., 2012; Woodhead et al., 2011; LaPierre et al., 1992; Cigolini et al., 1991; Streck et al., 2005; Streck et al., 2001).

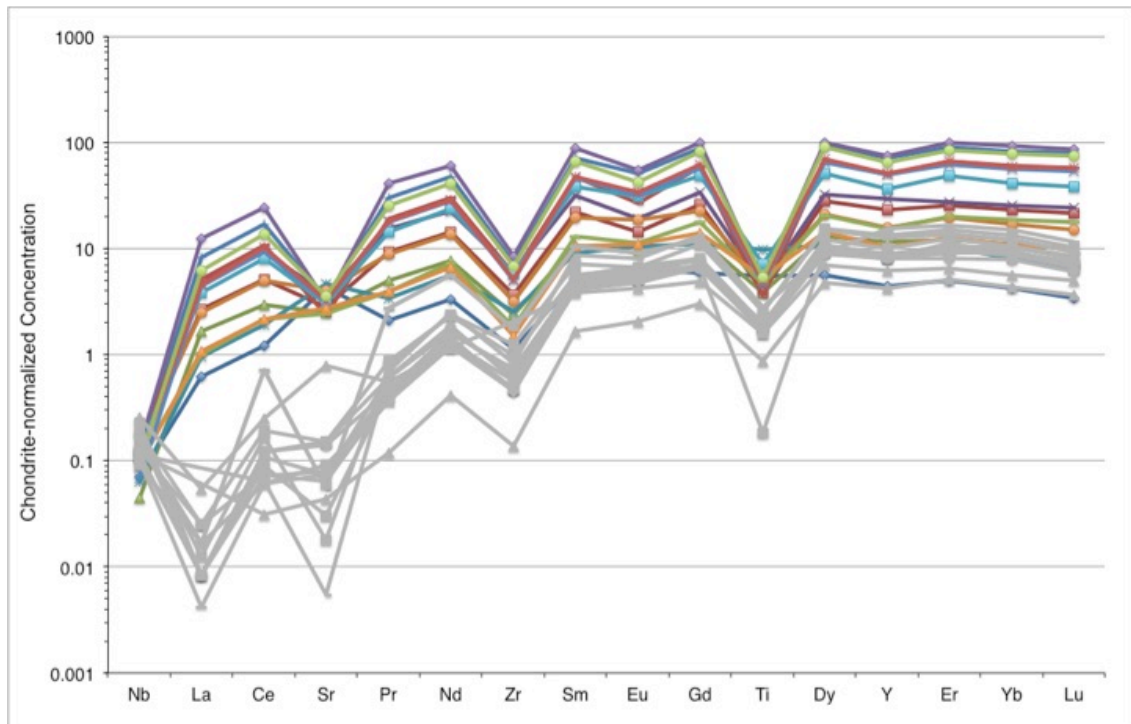


Figure A-8. Chondrite-normalized extended REE diagram comparing trace element concentrations of mantle clinopyroxene (in grey) from the Santa Elena ophiolite (Wright, 2011) to detrital clinopyroxene of Rivas and Descartes Formations (in color).

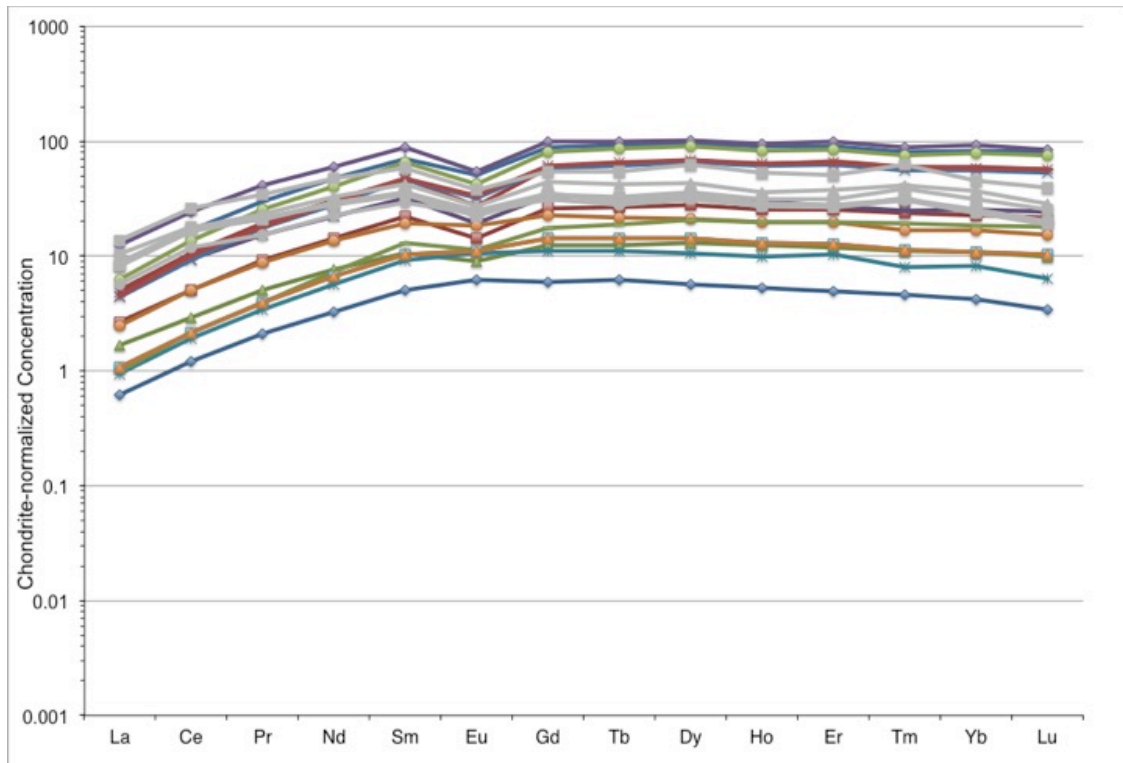


Figure A-9. Chondrite-normalized REE diagram comparing trace element concentrations of mantle clinopyroxene (in grey) from backarc gabbroic clinopyroxene (Harigane et al., in press) to detrital clinopyroxene of Rivas and Descartes Formations (in grey).

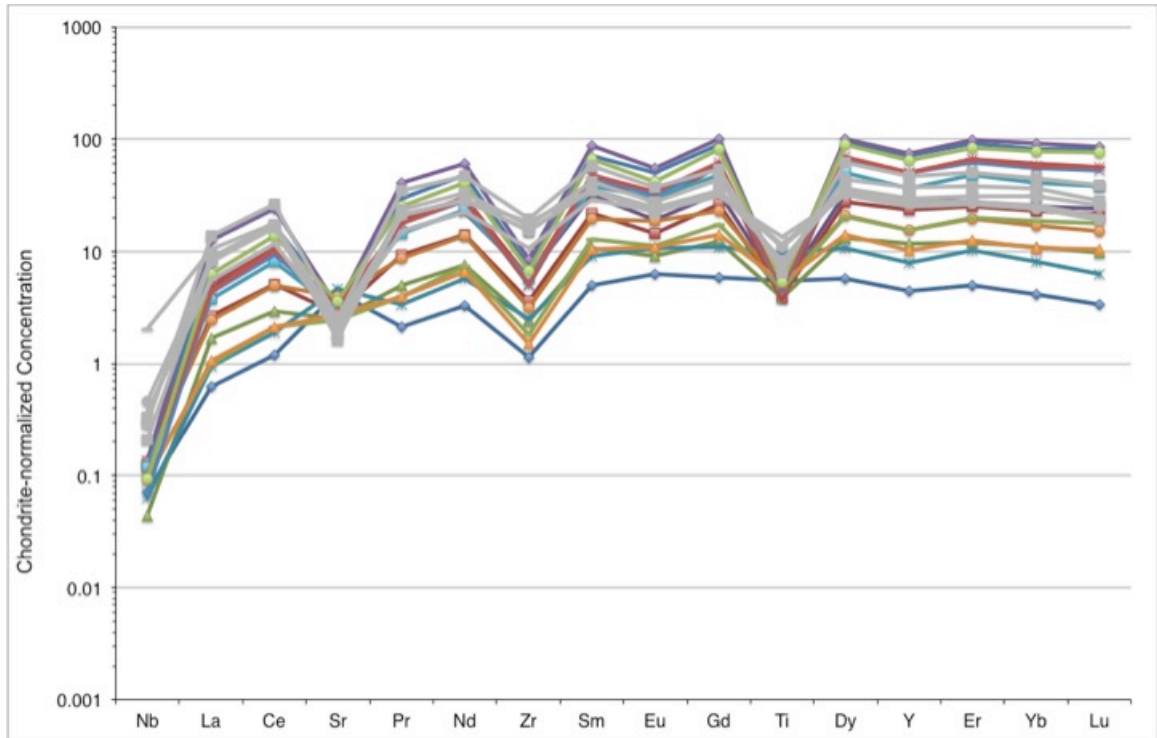


Figure A-10. Extended Chondrite-normalized REE diagram comparing trace element concentrations of clinopyroxene from mid-ocean ridge gabbros (in grey) (Harigane, in press) to the detrital Rivas and Descartes clinopyroxene (in color).

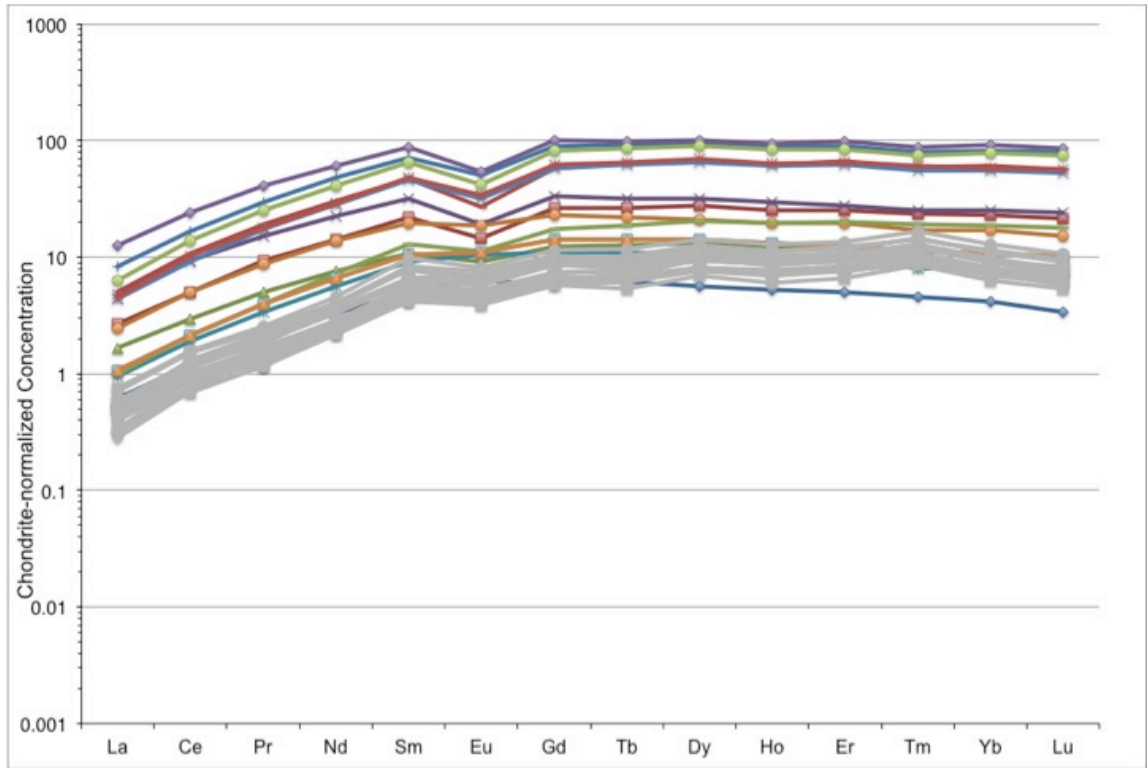


Figure A-11. Chondrite-normalized REE diagram comparing trace element concentrations of clinopyroxene from mid-ocean ridge gabbros (in grey) (Koepke et al., 2011) to detrital clinopyroxene of Rivas and Descartes Formations (in color).

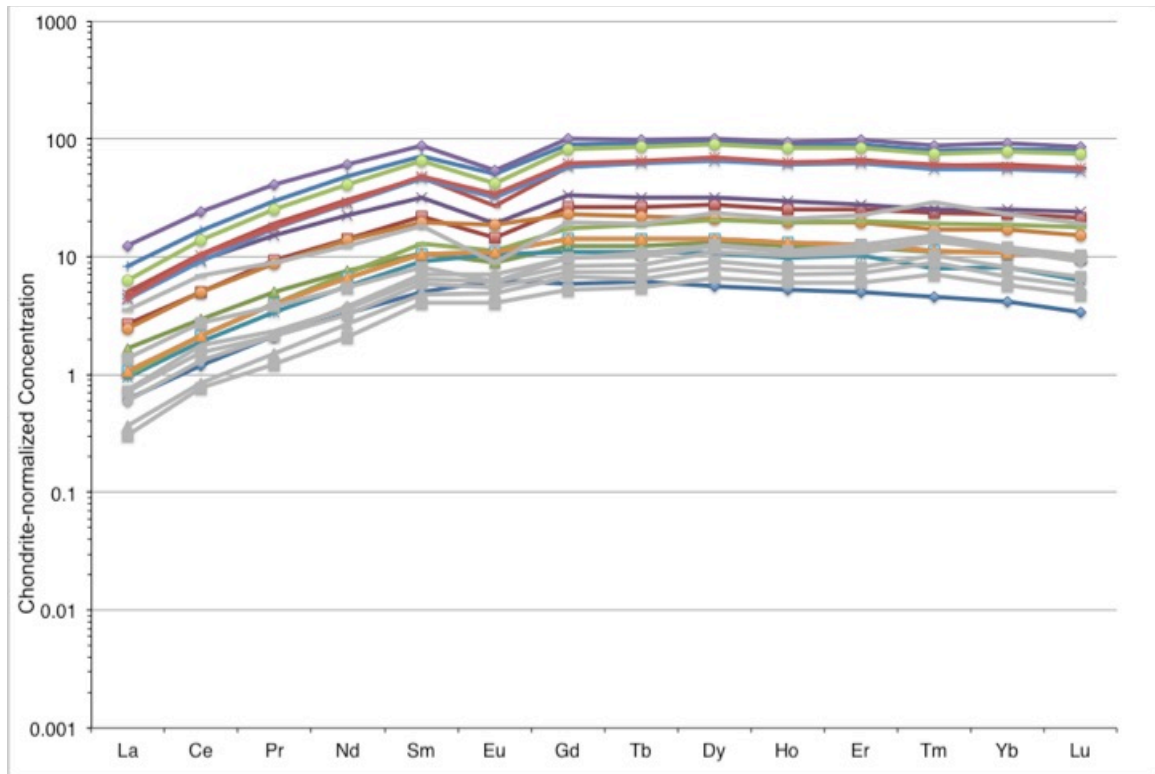


Figure A-12. Chondrite-normalized REE diagram comparing trace element concentrations of clinopyroxene from mid-ocean ridge gabbros (in grey) (Drouin et al., 2009) to detrital clinopyroxene of Rivas and Descartes Formations (in color).

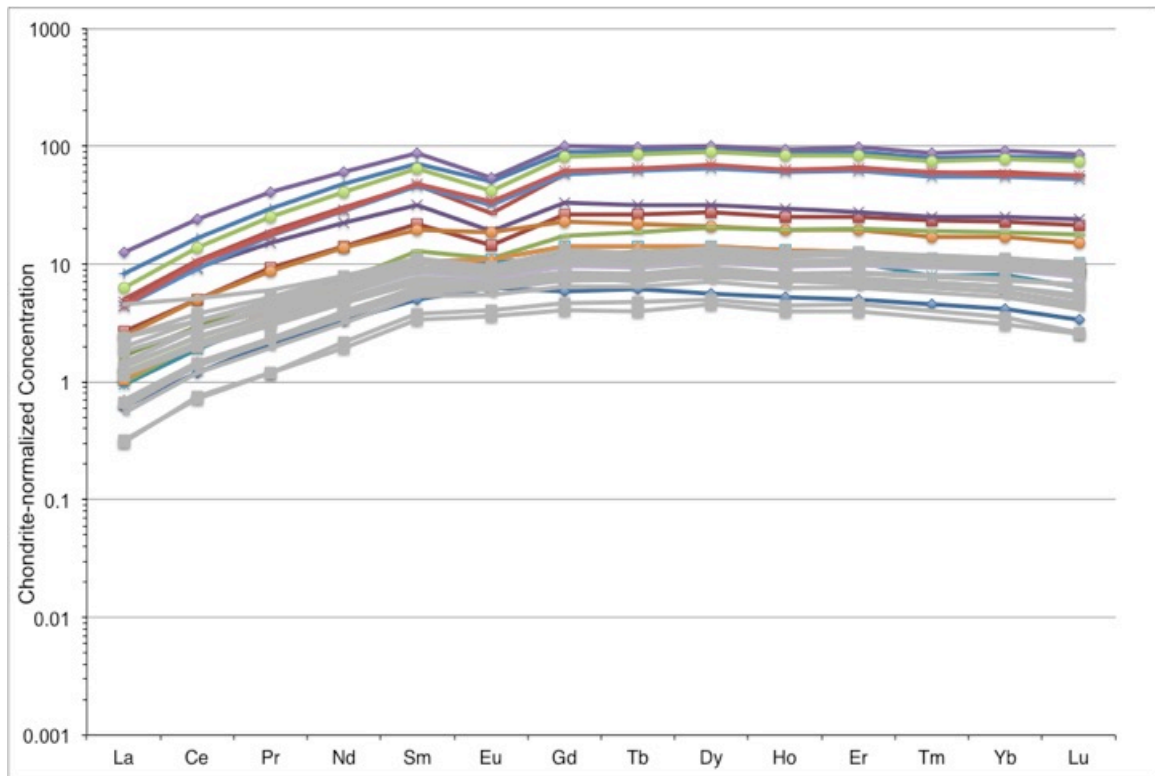


Figure A-13. Chondrite-normalized REE diagram comparing trace element concentrations of clinopyroxene from volcanic arc gabbros (in grey) (Woodhead et al., 2011) to detrital clinopyroxene of Rivas and Descartes Formations (in color).

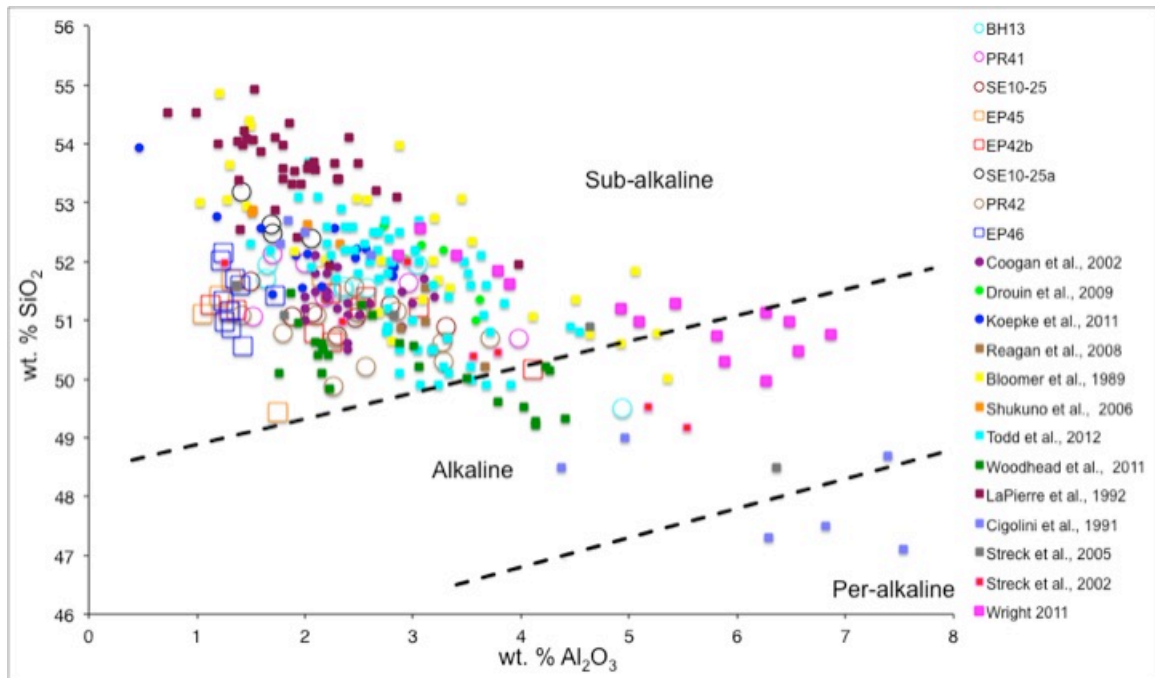


Figure A-14. Al<sub>2</sub>O<sub>3</sub> vs SiO<sub>2</sub> co-variation diagram for Rivas and Descartes Formation detrital clinopyroxene grains. Divisions for compositional types are after Le Bas (1962). The detrital grains are open circles and the volcanic clinopyroxene grains from andesite boulders are open squares. Additional comparison data from global sources are included: Santa Elena ophiolite clinopyroxene (closed magenta square), MOR gabbroic clinopyroxene (closed circles), volcanic arc clinopyroxene (closed squares).

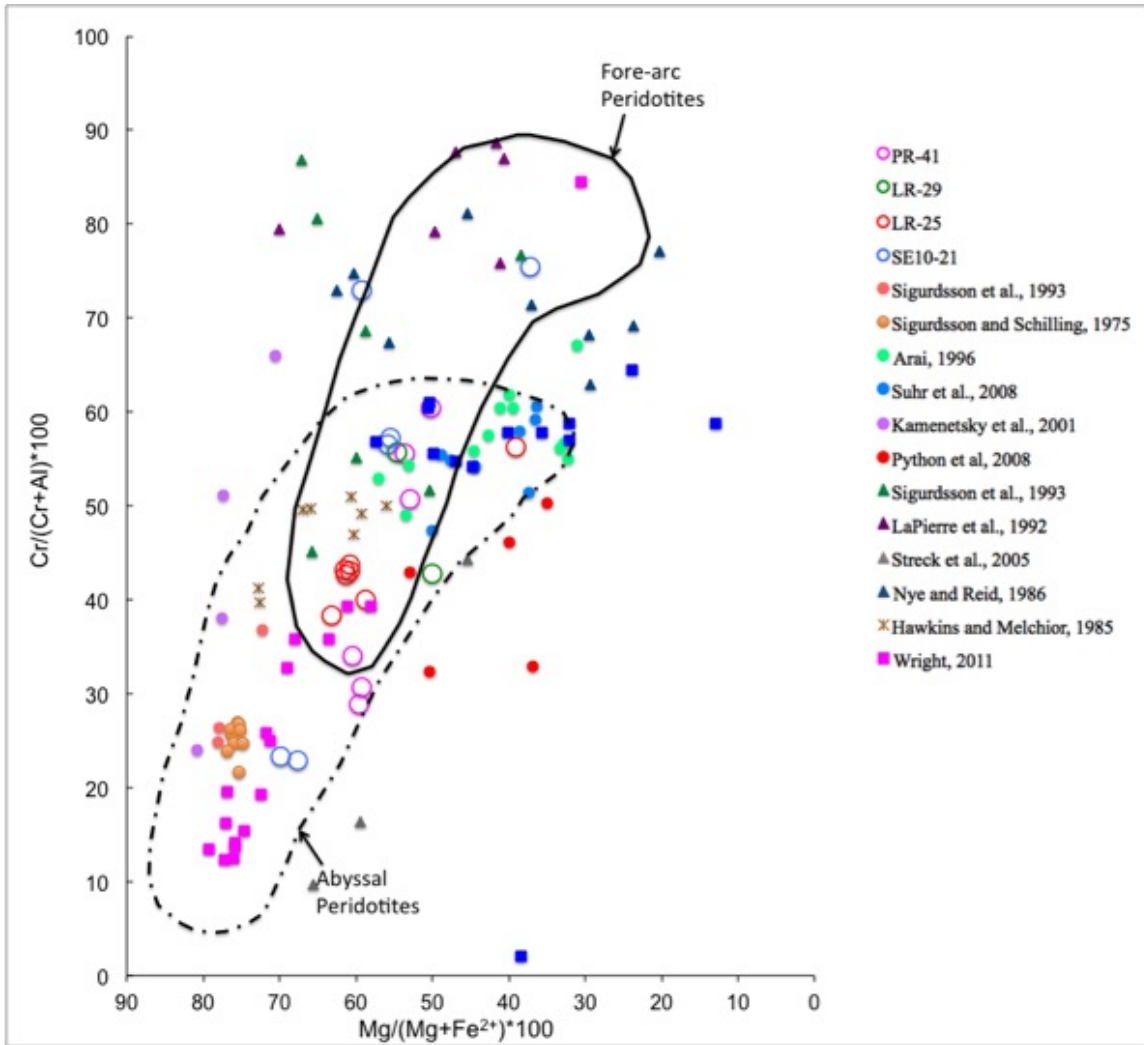


Figure A-15. Plot of spinel Mg# ( $Mg/(Mg+Fe^{2+})$ ) against spinel Cr# ( $Cr/(Cr+Al)$ ). The detrital spinel grains fall in both the abyssal and forearc fields. Fertile to moderately depleted abyssal peridotites fall on the lower end of this trend with low Cr#'s and high Mg#'s, while more depleted fore-arc peridotites fall on the upper end of the trend (fields after Dick and Bullen, 1984). Figure includes global comparison data from: Santa Elena ophiolite spinel, mid-ocean ridge gabbros, volcanic arcs, and backarcs.

## **Appendix III: Petrographic descriptions**

BH-13 thin section shows two depositional periods: a fine-grained, lower energy deposit and a coarser-grained, higher density deposit. The fine-grained deposit has fine (0.177-0.125 mm) to very-fine (0.125-0.088mm) grain sizes, is well sorted, and has fine, planar laminations. Grains are angular to sub-angular plagioclase in a muddy matrix. The coarse-grained deposit is massive with no layering. Grain sizes vary from coarse (2 mm) to fine (0.125 mm) grains in a muddy matrix and are not well sorted. Grains consist of abundant angular to subrounded plagioclase, subangular to subrounded clinopyroxene, opaques, carbonate fossil tests, and angular to subangular sparry calcite clasts. Plagioclase grains show zoning and polysynthetic twinning; clasts are beginning to seritize.

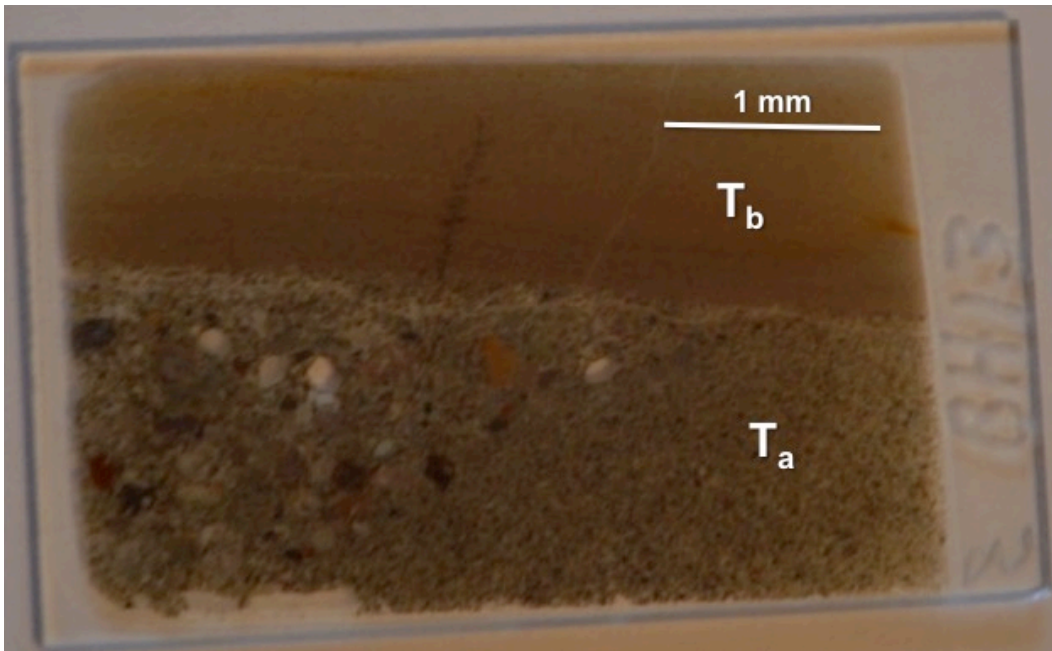


Figure A-16. BH-13 thin section showing two depositional periods: lower, massive deposit (T<sub>a</sub>) with coarse to fine grains and an upper, fine- to very-fine grained parallel laminated (T<sub>b</sub>) deposit.

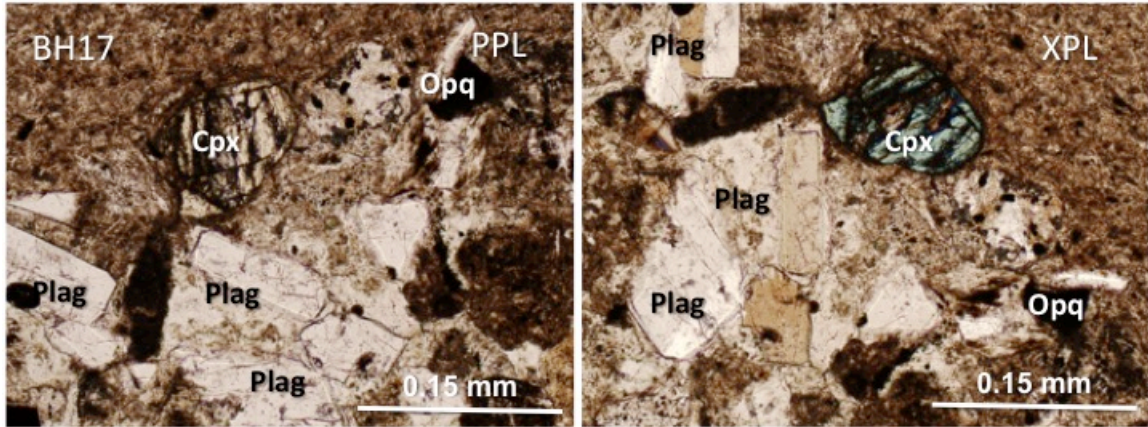


Figure A-17. Photomicrographs in plane polarized light (PPL) and cross-polarized light (XPL) of the coarse grained  $T_b$  deposit. Detrital grains include abundant plagioclase with opaques and very minor clinopyroxene in a muddy matrix.

BH-17 thin section shows three distinct depositional periods within this sample (Figure A-18): two very fine-grained sand (0.125-0.088 mm) to silt sized (<0.088 mm) grain deposits, between a fine-grained deposit. The silt-sized grains in the well sorted pink layer (a) that show ripple cross-bedding of  $T_c$  Bouma distinction. There are scarce grains of opaque heavy minerals throughout the section. At the base of the massively bedded section (b), there is an inversely graded bed with euhedral tabular plagioclase grains showing both twinning and zoning; scarce high relief green clinopyroxene grains with 2<sup>nd</sup> order colors (see in picture); and heavy mineral grains that are seen as reddish-brown in plane polarized light. The massive section (Figure A-17) sees a grain size increase to fine-medium sand-sized (0.5 -0.177 mm) grains. Within a muddy matrix, there are abundant plagioclase grains that are angular to rounded (0.177-0.088 mm), show polysynthetic twinning, some grains are altering to clays (seritized). There are scarce fine-sized (0.25-0.177 mm) grains of clinopyroxene, and heavy minerals that are black and reddish-brown in color. At the top of the massive

section, before the parallel-layered  $T_b$  brown section and the middle massive deposit ( $T_a$  Bouma classification), there is what appears to be fossil hash in a brown muddy matrix. Fossils are composed of both carbonate and siliceous material and are  $<0.125$  mm. The very fine-grained brown deposit has parallel laminations, which are categorized as a  $T_b$  Bouma classification, and deposited by a low-density turbidity current. There are fine fractures at the top of the deposit that are filled with calcite.

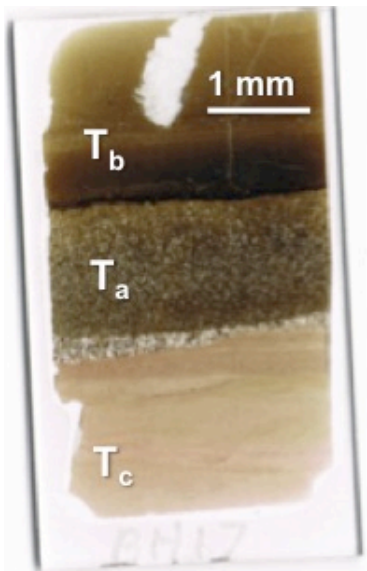


Figure A-18. Thin section of BH-17 showing three depositional periods with Bouma divisions: pink layer ( $T_c$ ) shows cross-beds, middle, massive layer ( $T_a$ ), and upper, plane laminated layer ( $T_b$ ).

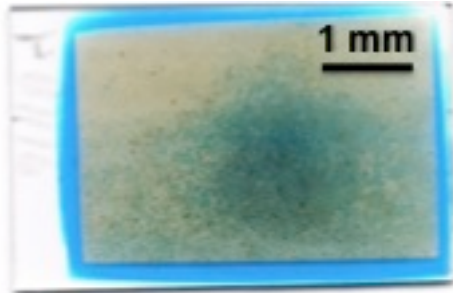


Figure A-19. Thin section of BH-16 showing fine- to very fine- sand sized grains in the deposit.

Fine- to very-fine grained sand-sized deposit in a muddy matrix with thin euhedral laths and angular to subangular grains of plagioclase (0.25-0.125 mm). Most plagioclase grains are unaltered, while some are altering to clay. Grains are well sorted and there are abundant, very fine grained (0.125-0.062 mm) heavy minerals that are black to reddish-brown in color. Fossil tests and clinopyroxene grains are sparse.

PJ37

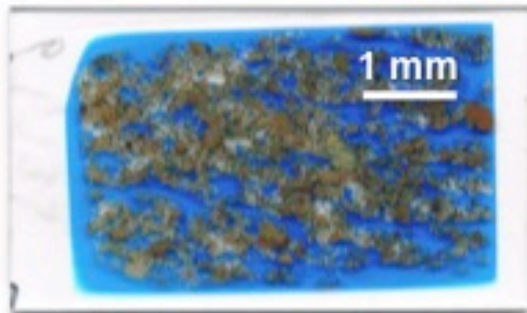


Figure A-20. Thin section from PJ-37 shows grains that are not well consolidated and coarser grain sizes.

Thin section consists of coarse (2 mm) to fine (0.177 mm) grains that are not well consolidated. Clasts are not well sorted and consist of abundant angular to subrounded plagioclase laths with zoning and polysynthetic twinning, rounded mud clasts, opaque minerals, and sparse clinopyroxene. Cement is muddy and sample is immature.

SE10-26 sample has a muddy matrix with calcite fossil tests, tabular grains of plagioclase, sparry calcite grains, clinopyroxene, and abundant opaque minerals. Grain sizes range from medium (1 mm) to very fine (0.088 mm). The sample is poorly sorted and texturally immature. Plagioclase grains are tabular laths that are angular to subangular, show twinning and zoning, and show various stages of alteration to sericite. Clinopyroxene grains are angular to subangular. Opaque minerals are abundant and black to reddish-brown in plane polarized light. Many grains are pyritized. Spinel is sparse in the sample and is only identified in reflected light. Calcite fossils include gastropods, ostracodes, clams, bryozoans, and both large and small foraminifera (forams). The larger benthic forams are indicative of shallow water environments, but the smaller forams are indicative of deep water. The benthic forams were likely reworked by the turbidity currents and redeposited in the deep water deposit.

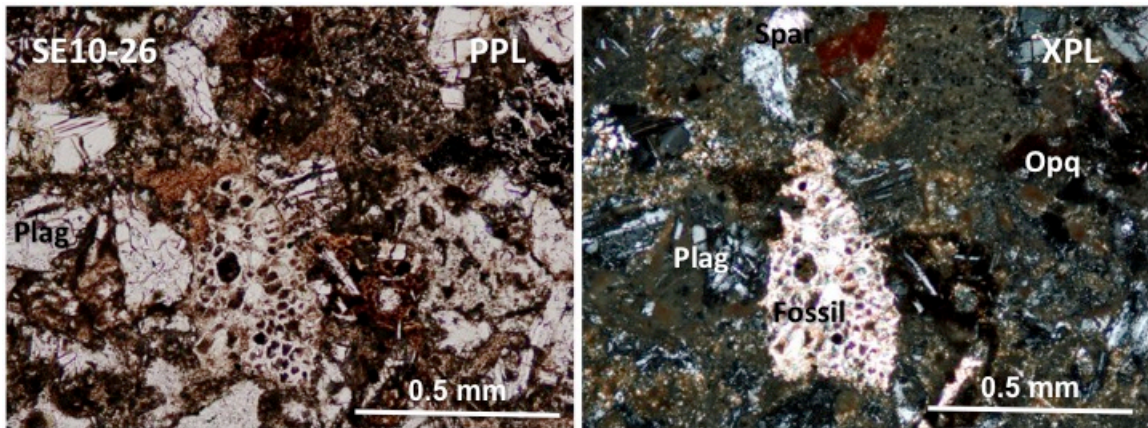


Figure A-21. Photomicrographs of SE10-26 that show plagioclase laths, sparry calcite, opaque grains, and a large bryozoan fossil test in both plane and cross-polarized light.

Thin section from SEB-31 is a limestone with a micritic matrix, carbonate foraminifera tests (0.35-0.7 mm), gastropod tests and other shell hash. Smaller fossil grains are 0.177-0.088 mm. Post-depositional fractures in the rock are filled by sparry calcite.

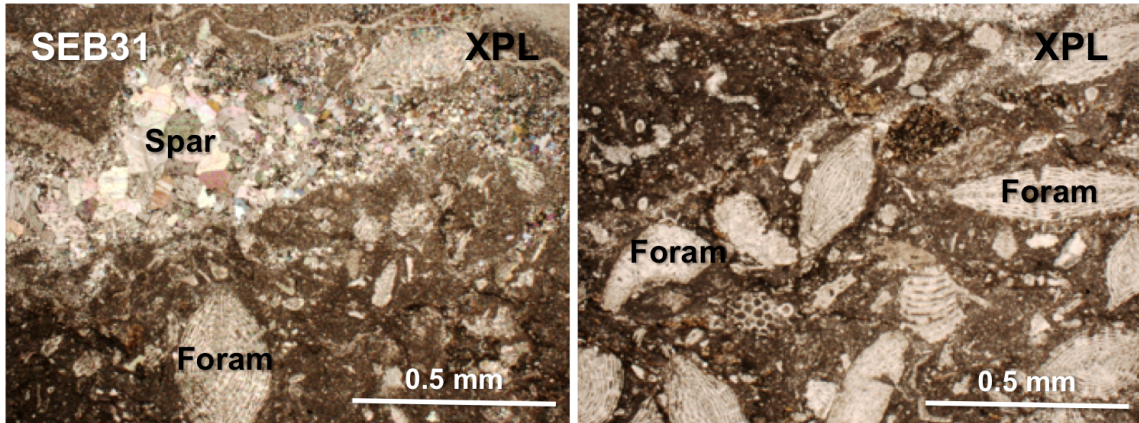


Figure A-22. Photomicrographs of micritic limestone with foraminifera (Foram), other fossil grains, and sparry calcite (Spar) .

## **Appendix IV: Error tables**

Table A-2. Error Table for Arenal Hornblende standard (NMNH 111356)

	Literature Values:			%
	Arenal Hbl.	Avg. Value	Abs. Std. Dev.	
Na <sub>2</sub> O	1.91	2.05	0.11	5.41
MgO	14.24	15.25	0.25	1.63
SiO <sub>2</sub>	41.46	41.99	1.85	4.40
Al <sub>2</sub> O <sub>3</sub>	15.47	14.10	0.32	2.27
K <sub>2</sub> O	0.21	0.21	0.02	9.76
CaO	11.55	12.12	0.26	2.13
TiO <sub>2</sub>	1.41	1.42	0.02	1.62
MnO	0.15	0.17	0.02	9.88
Fe <sub>2</sub> O <sub>3</sub>	12.74	13.23	0.52	3.93
Total	99.14	100.54	2.11	2.10

Table A-2. Error analyses of thirty six repeat analyses of Arenal hornblende standard measured on the University of Houston electron microprobe.

Table A-3. Error Table for Chromite standard

	Avg. Value	Abs. Std. Dev.	Published Value
			Chromite23
TiO <sub>2</sub>	0.06	0.04	-
Al <sub>2</sub> O <sub>3</sub>	9.87	0.11	9.80
Cr <sub>2</sub> O <sub>3</sub>	60.29	0.28	59.82
Fe <sub>2</sub> O <sub>3</sub>	3.84	0.51	-
MgO	15.18	0.18	15.02
CaO	0.01	0.01	0.10
MnO	0.12	0.01	0.10
FeO	9.98	0.24	12.89
ZnO	0.05	0.04	-
Total	99.40	0.47	-

Table A-3. Error analyses of thirty five analyses of Chromite23 standard measured on the University of Houston electron microprobe.

Table A-4. Error Table for KL2G standard

Sample	KL2-G	Average	Abs. Std. Dev.	Rel. Std. Dev.
Mg24	44265	44265	429	0.97
Si29	235135	235135	7483	3.18
Ti49	15343	15343	1030	6.72
V51	309	309	12	4.03
Sr88	356	356	19	5.44
Y89	25.4	25.4	1.3	4.97
Zr90	152	152	7	4.64
Nb93	15	15.0	0.8	5.14
La139	13.1	13.1	1.0	7.47
Ce140	32.9	32.9	2.4	7.19
Pr141	4.6	4.60	0.33	7.11
Nd146	21.7	21.7	1.5	7.04
Sm147	5.55	5.55	0.39	7.03
Eu153	1.92	1.92	0.16	8.20
Gd157	5.92	5.92	0.65	10.98
Tb159	0.89	0.89	0.06	6.89
Dy163	5.22	5.22	0.34	6.60
Ho165	0.961	0.96	0.07	7.45
Er166	2.54	2.54	0.11	4.50
Tm169	0.331	0.33	0.02	6.66
Yb172	2.1	2.10	0.16	7.55
Lu175	0.285	0.28	0.02	7.93
Hf178	3.93	3.93	0.27	6.92

Table A-4. Error analyses of fifteen repeat analyses of the KL2G standard measured on the University of Houston LA-ICP-MS.

Table A-5. Error analyses of the ATHO standard

	Literature			
	ATHO-G	Average	Abs. Std. Dev.	Rel. Std Dev
Mg24	621	620.90	11.77	1.90
Si29	353403	334947.15	12881.12	3.85
Ti49	1528	1538.18	47.86	3.11
V51	3.91	5.41	1.43	26.51
Sr88	94.1	102.89	3.43	3.33
Y89	94.5	107.53	3.76	3.50
Zr90	512	565.86	19.87	3.51
Nb93	62.4	61.65	2.33	3.78
La139	55.6	61.61	3.62	5.87
Ce140	121	134.75	7.27	5.40
Pr141	14.6	16.35	0.95	5.79
Nd146	60.9	68.16	4.18	6.13
Sm147	14.2	15.49	0.96	6.21
Eu153	2.76	2.89	0.21	7.42
Gd157	15.3	16.60	1.29	7.77
Tb159	2.51	2.87	0.21	7.47
Dy163	16.2	18.60	1.30	6.99
Ho165	3.43	3.82	0.26	6.89
Er166	10.3	11.65	0.77	6.63
Tm169	1.52	1.67	0.13	7.80
Yb172	10.5	11.84	0.97	8.15
Lu175	1.54	1.70	0.16	9.23
Hf178	13.7	15.42	1.34	8.72

Table A-5. Error analyses of twelve repeat analyses of the ATHO standard measured on the University of Houston LA-ICP-MS.